ABSTRACT BOOK

5th BIOMEMS and MICROFLUIDIC TECHNOLOGIES WORKSHOP

June 11-12, 2026

Sabancı Üniversitesi

SUNUM SABANCI UNIVERSITY NANOTECHNOLOGY RESEARCH AND APPLICATION CENTER

EFSUN

EGE UNIVERSITESI 1955

ODTÜ METU

METU MEMS CENTER

KOÇ UNIVERSITY

İZMİR YÜKSEK TEKNOLOJİ ENSTİTÜSÜ 1992

Abstract Book of

5th BioMEMS and Microfluidic Technologies Workshop

Hybrid

Sabancı University

Nanotechnology Research and Application Center
Istanbul ,Turkiye

Dates: June 11-12, 2026

Dear Colleagues,

It is our great pleasure to welcome you to the 5th BioMEMS and Microfluidic Technologies Workshop. This workshop is designed to promote interdisciplinary discussion across engineering, nanotechnology, biomedical sciences, and point-of-care innovation. Bringing together researchers, clinicians, engineers, industry representatives, and students, the workshop provides a collaborative platform for exchanging ideas, presenting recent advances, and establishing new scientific collaborations in the rapidly evolving fields of BioMEMS and microfluidic technologies. The scientific program features invited lectures, thematic sessions, and networking opportunities covering a broad spectrum of emerging technologies and translational applications, including:

- Biosensors
- MEMS / NEMS
- Microfluidics
- Lab-on-a-Chip Systems
- Point-of-Care Diagnostics
- Organ-on-a-Chip Systems
- Wearable and Implantable Devices
- Energy Harvesting and Self-Powered Sensors
- Environmental Monitoring
- Translational Microtechnologies
- Manufacturing and Scalable Fabrication
- Standardization, Interoperability, and System Integration

We sincerely thank all participants for joining us and contributing to this workshop. Through the diverse expertise of our invited speakers, engaging scientific discussions, and opportunities for academic networking, we hope this meeting will foster interdisciplinary collaboration, encourage innovative research, and inspire the next generation of scientists and engineers working at the interface of biology, medicine, and microscale technologies.

Organizing Committee

The 5th BioMEMS and Microfluidic Technologies Workshop is organized through the collaborative efforts of researchers from Sabancı University, İzmir Institute of Technology (IZTECH), METU MEMS Center, Ege University, and Koç University.

Chairs

Prof. Ali Koşar, Sabancı University

Prof. H. Cumhur Tekin, İzmir Institute of Technology (IZTECH) / METU MEMS Center

Vice Chairs

Prof. Özlem Yeşil Çeliktaş, Ege University

Prof. Metin Muradoğlu, Koç University

Prof. Haluk Külah, METU MEMS Center

Prof. Ender Yıldırım METU MEMS Center

Local Organizing Committee

Dr. Gül Kozalak, Sabancı University

Melis Hazal Porsuk, Sabancı University

İlayda Çelik, Sabancı University

Dr. İsmail Bütün, Sabancı University

Hasan Uluşan, METU MEMS Center

Workshop Program

	TR-time	CEST	11 June 2026, Thursday
Registrations	09:30 – 10:00	08:30 – 09:00	
Session 1	10:00 – 10:20	09:00 – 09:20	**Opening Remarks**
	10:20 – 10:50	09:20 – 09:50	**Olivier T. Guenat,** *Bioengineering the Lung Parenchyma and Its Diseases on Chip* ***(Online)***
	10:50 – 11:20	09:50 – 10:20	**Qasem Ramadan,** *Micro-engineered Organotypic In Vitro Models for Pharmacokinetics & Immune–Metabolic Disease Modelling*
	11:20 – 11:40	10:20 – 10:40	**Coffee Break**
Session 2	11:40 – 12:10	10:40 – 11:10	**Massimo Mastrangeli,** *Microelectromechanical Physiological Systems*
	12:10 – 12:40	11:10 – 11:40	**Suna Timur,** *Biofunctional Surfaces and Nanomaterial-Integrated Platforms for Point-of-Care Diagnostics* ***(Online)***
	12:40 – 14:00	11:40 – 13:00	**Lunch Break & Networking**
Session 3	14:00 – 14:30	13:00 – 13:30	**Huabing Yin,** *Integrating Microfluidics and Label-Free Detection for Diagnostics and Discovery* ***(Online)***
	14:30 – 15:00	13:30 – 14:00	**Onur Parlak,** *In vivo and In vitro Epidermal Sensors for Medical Diagnostics and Therapy*
	15:00 – 15:20	14:00 – 14:20	**Coffee Break**
Session 4	15:20 – 16:00	14:20 – 15:00	**Poster Session & Networking**
	16:00 – 16:30	15:00 – 15:30	**Hasan Kurt,** *Tailoring Plasmonic Metasurfaces for Optofluidic Biosensing*
	16:30 – 17:00	15:30 – 16:00	**Ali Beskok,** *Active Microfluidic Impedance Biosensors for Real-Time Biomolecule Detection* ***(Online)***
	19:00 – 22:00		**Gala Dinner**
	TR-time	**CET**	**12 June 2026, Friday**
Registrations	09:30 – 10:00	08:30 – 09:00	
Session 1	10:00 – 10:30	09:00 – 09:30	**Savaş Taşoğlu,** *Machine Learning-Automated Microfluidic Circuit Design: From µFluidicGenius to Programmable 3D-Printed LAMP-on-a-Chip for Rapid Point-of-Care Mpox*
	10:30 – 11:00	09:30 – 10:00	**Oya Tagit,** *Microfluidics as an Enabling Technology for the Clinical Translation of Nanomedicines: From Design to Scalable Manufacturing*
	11:00 – 11:20	10:00 – 10:20	**Coffee Break**
Session 2	11:20 – 11:50	10:20 – 10:50	**Morteza Ghorbani,** *Cavitation Technology in Biomedical Applications: Fundamentals and Emerging Opportunities*
	11:50 – 12:20	10:50 – 11:20	**Jérôme Charmet**, *Microfluidics and Robotics, what can go wrong?* ***(Online)***
	12:20 – 13:40	11:20 – 12:40	**Lunch Break & Networking**
Session 3	13:40 – 14:10	12:40 – 13:10	**Elsa Batista,** *Metrology and Standardization Challenges in Microfluidics* ***(Online)***
	14:10 – 14:40	13:10 – 13:40	**Darwin Reyes,** *Microphysiological Systems with Integrated Sensors for Continuous, Real-Time Dynamic Measurements* ***(Online)***
	14:40 – 15:10	13:40 – 14:10	**Vania Silverio**, Microfabrication as an Enabler of Performance and Integration in Microfluidics
	15:10 – 15:30	14:10 – 14:30	**Coffee Break**
	15:30 – 16:30	14:30 – 15:30	**Poster Session & Networking**
	16:30 – 17:00	15:30 – 16:00	**Best Poster Award & Closing Remarks**

Acknowledgements

The Organizing Committee gratefully acknowledges the valuable support of all individuals and organizations who contributed to the successful organization of the 5th BioMEMS and Microfluidic Technologies Workshop.

The Committee members sincerely thank SUNUM (Sabancı University Nanotechnology Research and Application Center) for hosting the workshop and for providing the venue, organizational infrastructure, and administrative support throughout the event.
They also express our sincere appreciation to the Faculty of Engineering and Natural Sciences of Sabanci University for its invaluable support and contributions to the organization of the workshop.

They gratefully acknowledge the EFSUN Center of Excellence for its support in promoting interdisciplinary research and collaboration across functional surfaces and interfaces, nanotechnology, micro/nanofluidics, biomedical engineering, and related fields.

They also acknowledge the funding from the MicroFloTec project of the European Commission. They appreciate the Beespenser Company, sponsor of the 5th BioMEMS and Microfluidic Technologies Workshop, for its generous support in organizing this successful event.

Finally, they thank all invited speakers, presenters, session chairs, committee members, and participants whose enthusiasm and scientific contributions made this workshop a successful and inspiring scientific meeting.

POSTER ABSTRACTS

Dynamic Tracking of Single Particles in a Pneumatic Valve-Integrated Microfluidic Magnetic Levitation System

Sadik Koc[1], Busra Erimez[1], Hilal Doger[1], and *H. Cumhur Tekin[1,2]
[1]The Department of Bioengineering, Izmir Institute of Technology, Türkiye
[2]METU MEMS Center, Türkiye

Introduction

Magnetic levitation (MagLev) systems have emerged as powerful label-free platforms for density-based characterization and separation of particles and biological samples in paramagnetic media [1–3]. Conventional microfluidic MagLev systems generally rely on single-channel architectures, requiring interruption of the experiment during environmental modifications such as medium exchange or drug exposure. This limitation restricts continuous monitoring of the same levitating object and introduces variability in longitudinal measurements. For applications involving dynamic cellular responses, including drug treatment and cell-state transitions, maintaining uninterrupted observation of the same particle or cell is essential for accurate temporal analysis [4,5]. To address this challenge, we developed a pneumatic valve-integrated multi-chamber microfluidic MagLev platform capable of performing environmental modulation while continuously tracking single particles without disturbing their levitation equilibrium.

Materials and Methods

The microfluidic device was fabricated in polydimethylsiloxane (PDMS) using standard soft lithography techniques. The chip consisted of a main levitation channel divided into three independent chambers through pneumatically actuated valves integrated into a separate control layer. Reliable valve closure was achieved at approximately 2 bar pressure, enabling leakage-free compartmentalization and controlled medium exchange between chambers. Medium replacement experiments were performed using clear and colored solutions at flow rates ranging from 0.1 to 0.5 µL/min to evaluate exchange efficiency. Flow-dependent levitation behavior was characterized using 1.035 g/mL density microparticles suspended in paramagnetic media.

Results and Discussion

The developed platform enabled efficient medium exchange, achieving over 90% replacement within 30 minutes at flow rates of 0.1 µL/min and above. Building upon our previously established stable confinement of particles under varying flow conditions [6], the present work focuses on dynamic single-particle tracking. Levitation analysis revealed that increasing flow rates resulted in reduced levitation height due to enhanced drag forces acting on the particles. Despite this reduction, particles remained stably confined up to a critical threshold, after which displacement and eventual chamber exit were observed. Importantly, when flow was terminated, particles rapidly returned to their original equilibrium positions. Dynamic medium exchange experiments conducted on a single bead demonstrated stable levitation behavior following replacement between different paramagnetic media. Post-exchange levitation heights showed strong agreement with static control measurements, confirming that environmental modulation could be achieved without disrupting particle stability or equilibrium conditions.

These findings demonstrate the capability of the system to continuously monitor single particles across multiple environmental states while preserving measurement reliability.

Conclusion

This study presents a pneumatic valve-integrated microfluidic MagLev platform enabling dynamic environmental control and real-time tracking of single particles. By allowing repeated measurements on the same levitating object without experimental interruption, the system overcomes the major limitation associated with conventional MagLev platforms. The proposed approach provides a promising framework for future applications involving density-based cellular analysis, longitudinal single-cell monitoring, drug screening, and precision sorting.

Acknowledgement

The authors gratefully acknowledge TÜBİTAK (Project No. 124E059) for financial support. S.K. acknowledges support from the TÜBİTAK 2211-A National Scholarship Program for PhD Students.

References

[1] B. Karakuzu *et al.*, "Magnetic levitation-based miniaturized technologies for advanced diagnostics," *Emergent Materials 2024 7:6*, vol. 7, no. 6, pp. 2323–2348, Jul. 2024, doi: 10.1007/S42247-024-00762-6.

[2] E. Yilmaz, E. Ozcivici, and H. C. Tekin, "Microfluidic Platform for Sorting Materials Based on Their Densities Using Magnetic Levitation," *Proceedings - 2019 Innovations in Intelligent Systems and Applications Conference, ASYU 2019*, Oct. 2019, doi: 10.1109/ASYU48272.2019.8946406.

[3] N. G. Durmus *et al.*, "Magnetic levitation of single cells," *Proc Natl Acad Sci U S A*, vol. 112, no. 28, pp. E3661–E3668, Jul. 2015, doi: 10.1073/PNAS.1509250112.

[4] S. Kecili *et al.*, "µDACS platform: A hybrid microfluidic platform using magnetic levitation technique and integrating magnetic, gravitational, and drag forces for density-based rare cancer cell sorting," *Biosens Bioelectron X*, vol. 15, p. 100392, Dec. 2023, doi: 10.1016/J.BIOSX.2023.100392.

[5] F. Eduati *et al.*, "A microfluidics platform for combinatorial drug screening on cancer biopsies," *Nature Communications 2018 9:1*, vol. 9, no. 1, pp. 1–13, Jun. 2018, doi: 10.1038/s41467-018-04919-w.

[6] S. Koc *et al.,* "Pneumatic Valve-Integrated Magnetic Levitation-Based Microfluidic System for in-Situ Medium Exchange," in 2026 IEEE 39th International Conference on Micro Electro Mechanical Systems (MEMS), Jan. 2026, doi: 10.1109/MEMS64181.2026.11419246.

Characterization of Garlic-Derived Exosome-Like Nanoparticles and Evaluation of Their Effects on Cell Viability in 2D and 3D A549 Lung Cancer Models

Rasim Efe Can[1], Büşra Yüksel[1], Emre Cebeci[1], Oğuz Kaan Kırbaş[1], Sibel Şimsek Yazıcı[2], Fikrettin Şahin[1]

[1]Faculty of Engineering and Natural Sciences, Genetics and Bioengineering Department, Yeditepe University, İstanbul, Turkey

[2]R & D and Analysis Center Laboratories (YÜ-AGAM) Yeditepe University, 34718 İstanbul

Lung cancer remains one of the leading causes of cancer-related mortality worldwide. Recently, plant-derived exosome-like nanoparticles have attracted considerable attention due to their potential biological activities and biocompatibility [1]. Conventional two-dimensional (2D) cell culture systems fail to fully mimic the complexity of the tumor microenvironment, whereas three-dimensional (3D) spheroid models provide a more physiologically relevant platform for evaluating cellular responses [2,3]. Therefore, this study aimed to characterize garlic-derived exosome-like nanoparticles and evaluate their effects on cell viability in both 2D and 3D A549 lung cancer models.

Exosome-like nanoparticles were isolated from garlic, and nanoparticle tracking analysis (NTA) revealed a high-yield stock concentration 2.14e+11 ± 2.36e+09 particles/ml. The cytotoxic effects of these nanoparticles on A549 cells were evaluated using the MTS cell viability assay after 72 hours of incubation. In 2D cultures, the garlic-derived nanoparticles significantly reduced cell survival in a dose-dependent manner, exhibiting strong cytotoxic activity with an IC50 value achieved at a 10% concentration, where cell viability decreased to approximately 44%. In contrast, the comparative analysis revealed that 3D spheroid models exhibited a higher resistance profile; at the same 10% concentration, cell viability remained at approximately 70%, indicating that the 3D microenvironment significantly influences cellular sensitivity to plant-derived vesicles.

In conclusion, garlic-derived exosome-like nanoparticles exhibited a potent anti-cancer effect on A549 lung cancer cells. The observed differential resistance between the two platforms underscores that 3D spheroid models provide a more physiologically representative platform for evaluating the biological effects of extracellular vesicles, highlighting the critical importance of advanced *in vitro* models for extracellular vesicle research and cancer studies.

Acknowledgement: The authors acknowledge financial support from The Scientific and Technological Research Council of Türkiye (22AG028)

References:

[1] Mu, J., Zhuang, X., Wang, Q., Jiang, H., Deng, Z.B., Wang, B., et al. (2014). Interspecies communication between plant and mouse gut host cells through edible plant derived exosome-like nanoparticles. Molecular Nutrition & Food Research, 58(7), 1561-1573.

[2] Edmondson, R., Broglie, J.J., Adcock, A.F., & Yang, L. (2014). Three-dimensional cell culture systems and their applications in drug discovery and cell-based biosensors. Assay and Drug Development Technologies, 12(4), 207-218.

[3] Kapałczyńska, M., Kolenda, T., Przybyła, W., Zajączkowska, M., Teresiak, A., Filas, V., et al. (2018). 2D and 3D cell cultures – a comparison of different types of cancer cell cultures. Archives of Medical Science, 14(4), 910-919.

Dissipative Particle Dynamics (DPD): A Coarse-Graining Bridge Between Molecular Dynamics and Continuum Modeling for Microfluidics, Lab-on-a-Chip Systems, and Translational Biomedical Technologies

Salar Heyat Davoudian[1,2], Ali Koşar[1,2,3]

[1]Faculty of Engineering and Natural Science, Sabanci University, 34956 Tuzla, Istanbul, Türkie

[2]Center of Excellence for Functional Surfaces and Interfaces for Nano-Diagnostics (EFSUN), Sabancı University, Orhanli, 34956 Tuzla, Istanbul, Turkey

[3]Sabanci University Nanotechnology Research and Application Center, 34956 Tuzla, Istanbul, Turkey

Introduction

Microfluidics, lab-on-a-chip platforms, and translational biomedical technologies rely on the precise manipulation of fluids, droplets, particles, and biological entities at micro- and mesoscales. At these scales, system behavior is governed not only by continuum hydrodynamics but also by interfacial forces, thermal fluctuations, wettability, contact-line dynamics, and fluid–structure interactions. Consequently, the design and optimization of biomedical microdevices, diagnostic platforms, and targeted drug-delivery systems require modeling approaches capable of capturing phenomena across multiple length and time scales [1,2].

Dissipative Particle Dynamics (DPD) is a coarse-grained, particle-based mesoscale simulation method that bridges the gap between molecular dynamics and continuum fluid mechanics. By representing clusters of molecules as soft interacting particles, DPD significantly reduces computational cost while preserving essential hydrodynamic behavior, thermal fluctuations, and interfacial physics. Since its original formulation by Hoogerbrugge and Koelman [3] and its subsequent thermodynamic framework established by Groot and Warren [4], DPD has evolved into a versatile tool for investigating soft matter systems, polymeric fluids, multiphase flows, emulsions, suspensions, and biomedical transport phenomena [5–7]. The unique ability of DPD to simultaneously resolve fluid–fluid, fluid–structure, and fluid–surface interactions make it particularly attractive for microfluidic and biomedical applications. Recent studies have demonstrated its effectiveness in modeling deformable polymers, bio-inspired microswimmers,

droplet transport, wettability-controlled flows, and smart functional surfaces, where conventional continuum-based methods may face significant limitations [8–11].

This workshop introduces DPD as a coarse-graining framework that connects molecular-scale interactions to macroscale transport behavior in microfluidics, lab-on-a-chip systems, and translational biomedical technologies. The workshop will cover the governing equations, boundary-condition treatments, and numerical implementation of DPD, followed by representative case studies including bio-inspired polymeric tail drag reduction, rolling/sliding microdroplet dynamics, and wettability-gradient-driven droplet transport. These examples demonstrate how DPD can support the rational design of energy-efficient microrobots, smart biomedical interfaces, anti-icing surfaces, passive microfluidic transport platforms, and targeted drug-delivery systems. Despite significant advances in continuum CFD and molecular dynamics simulations, an important modeling gap still exists at mesoscopic scales where thermal fluctuations, interfacial dynamics, and fluid–structure interactions simultaneously influence transport phenomena. DPD has emerged as one of the most successful approaches for addressing this challenge.

Methods

Dissipative particle dynamics, DPD, consists of the system of particles that the behavior of any particle i is modeled by Newton's laws of motion, $\frac{dr_i}{dt} = V_i \quad , \quad \frac{dV_i}{dt} = f_i$, where r_i, V_i, and f_i indicate the position, velocity, and forces vector per unit mass, respectively. The interaction forces between DPD particles are obtained from the summation of conservative, dissipative, and random forces. Conservative forces model the thermodynamic behavior of DPD particles [12]. In single-phase flows, the conservative forces between particles i and j are obtained from $F_{ij}^{C} = a_{ij} w^{c}(r_{ij}) e_{ij}$, where $a_{ij} = 75 k_B T/\rho$ is the maximum repulsion parameter between particles i and j. Parameters k_B, T, and ρ are Boltzmann constant, temperature, and number density, respectively. According to conservative force equation, $w^c(r_{ij})$ is the weight function of the conservative force. This function is related to the free energy of particles and is given as, $w^{c} = \begin{cases} 1 - \frac{r_{ij}}{r_c} & r_{ij} < r_c \\ 0 & r_{ij} \geq r_c \end{cases}$, where $r_{ij} = r_i - r_j$ and r_c is the cut-off radius. In this equation, e_{ij} is the unit vector and equals to $r_{ij}/|r_{ij}|$. In multiphase flows, determining the repulsion parameter, i.e. a_{ij}, is of particular importance. Suppose i is the first phase particle and j is the second one. The repulsion parameter between the identical phase particles is determined according to the following equation [13], $a_{ii} = \frac{\kappa_i^{-1} - 1}{2\alpha\rho_i}$ and $a_{jj} = \frac{\kappa_j^{-1} - 1}{2\alpha\rho_j}$ where κ and ρ are the compressibility parameter and the density, respectively. α is the constant parameter equal to $\alpha = 0.101 \pm 0.001$. The repulsion parameter between i and j is defined from $(\delta_i - \delta_j)^2 = -r_c^4 \alpha(\rho_i^2 a_{ii} + \rho_j^2 a_{jj} - 2\rho_i \rho_j a_{ij})$. Here, δ_i and δ_j are the Hildebrand solubility parameters. The dissipative forces show the viscous behavior of particles and cause the reduction in relative velocity between DPD

particles [12]. Like the Stokes equation of drag force, the dissipative force is related to the first order of velocity and is given by $F_{ij}^{D} = -\gamma w^{D}(e_{ij} \cdot V_{ij})e_{ij}$. Here, γ is the dissipative force coefficient and $w^{D}(r_{ij})$ is the weight function of the dissipative force and V_{ij} equals $V_i - V_j$. As DPD is the coarse grain representation of the molecular dynamics method, the DPD particle's degree of freedom is less than the MD. So to satisfy the physics, the random forces are taken to account in DPD equations. The random force is $F_{ij}^{R} = \sigma w^{R}(r_{ij})\theta_{ij}e_{ij}$ where σ and $w^{R}(r_{ij})$ are the random force coefficient and weight function where θ_{ij} is the Gaussian random variable. To make the system isothermal, the dissipative and random force coefficients are related together using the fluctuation-dissipation theorem [4] as $w^{D}(r) = [w^{R}(r)]^2 = \begin{cases} \left(1 - \frac{r_{ij}}{r_c}\right)^2 & r_{ij} < r_c \\ 0 & r_{ij} \geq r_c \end{cases}$, $\sigma^2 = 2\gamma k_B T$. If there are any elastic particles in the domain, the forces between these particles would be written as $F_{ij}^{S} = -kr_{ij}e_{ij}$, where k is the elasticity constant between the particles, and it depends on the material. The conservative force repulsion parameter between the elastic (polymeric) particles and the fluid particles is calculated using $a_{ij} = a_{ii} + 3.27\chi_{ij}$, where χ_{ij} denotes the Flory–Huggins interaction parameter characterizing the interaction between the polymer and fluid particles.

For boundary conditions, the inlet and outlet are considered periodic, and the upper and lower walls of the channel have no-slip boundary conditions. The imaged particle method is used to apply the no-slip wall boundary condition [8]. The governing equations of Dissipative Particle Dynamics (DPD) are integrated using the modified velocity-Verlet algorithm. At each time step, the positions and velocities of all particles are updated based on the conservative, dissipative, random, and elastic forces acting on them. The particle position at the next time step is calculated as $r_i(t + \delta t) = r_i(t) + \delta t V_i(t) + \frac{1}{2}(\delta t)^2 f_i(t)$. The intermediate velocity is then predicted as $\tilde{V}_i(t + \delta t) = V_i(t) + \lambda \delta t f_i(t)$. where $\lambda = 0.65$ is an empirical parameter. After applying the appropriate boundary conditions and recalculating the forces at the updated particle positions, the velocity is corrected as $V_i(t + \delta t) = V_i(t) + \frac{1}{2}\delta t\big(f_i(t) + f_i(t + \delta t)\big)$.

Results and Discussion

1. Bio-Inspired Polymeric Tail Drag Reduction

Nature provides numerous examples of microorganisms that utilize flexible appendages, such as flagella and cilia, to interact with their surrounding fluid environment. Inspired by these biological systems, the present study investigates the role of flexible polymeric tails in drag reduction rather than thrust generation. Figure 1 illustrates several bio-inspired tail configurations, including single, double, triple, and hierarchical polymeric structures attached to a microswimmer-like body. These designs are motivated by natural swimmers such as sperm cells and flagellated bacteria, whose flexible tails significantly influence the surrounding flow field.

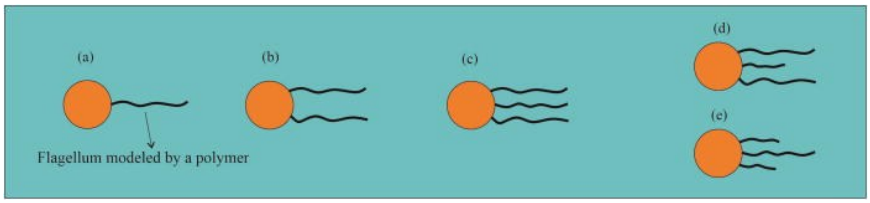

Figure 1. Different flexible structures: (a) single tail, (d) double tails, (c) triple tails, (d) hierarchical structure 1, and (e) hierarchical structure 2 [8].

To evaluate the effect of tail length on drag reduction, single polymeric tails with lengths ranging from 1.75D to 7D were investigated, where D is the characteristic diameter of the body (see Figure 2). The DPD simulations reveal that increasing the tail length substantially modifies the wake structure downstream of the body (Figure 3). Longer flexible tails interact more strongly with the surrounding fluid and generate a larger region of flow disturbance, resulting in significant changes in the pressure distribution around the body.

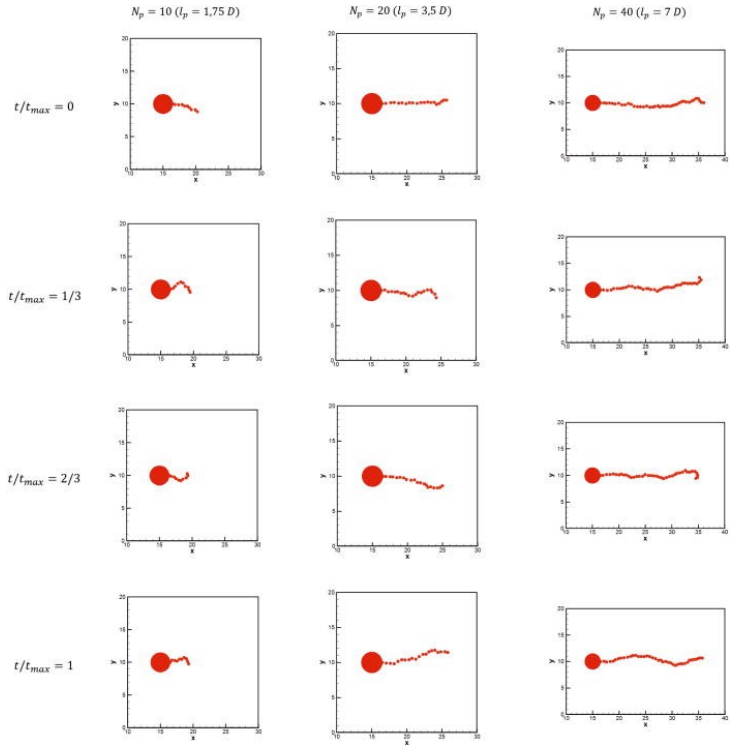

Figure 2. The flexible structures' motions at different times (k=50, Re=15)[8]

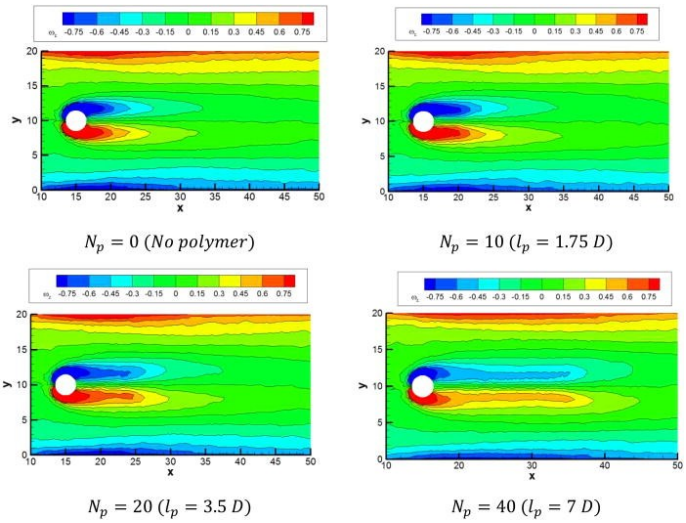

Figure 3. Vorticity contour in different polymer bead numbers (k=50, Re=15) [8]

Short tails ($l_p = 1.75D$) slightly increase the total drag due to an increase in pressure drag, whereas longer tails progressively reduce the drag coefficient. The longest investigated tail ($l_p = 7D$) decreases the total drag coefficient by approximately 22.9%, while the pressure drag is reduced by more than 35%. These results suggest that the primary drag-reduction mechanism originates from wake modification and pressure redistribution rather than changes in viscous drag. The nonlinear interaction between the flexible tail and the surrounding fluid alters the downstream vortex structures, thereby reducing the pressure difference between the front and rear portions of the body. In addition to single-tail configurations, nature frequently employs multiple and hierarchical appendages rather than isolated structures. Therefore, double-tail, triple-tail, and hierarchical polymer arrangements were also examined (Figure. 4).

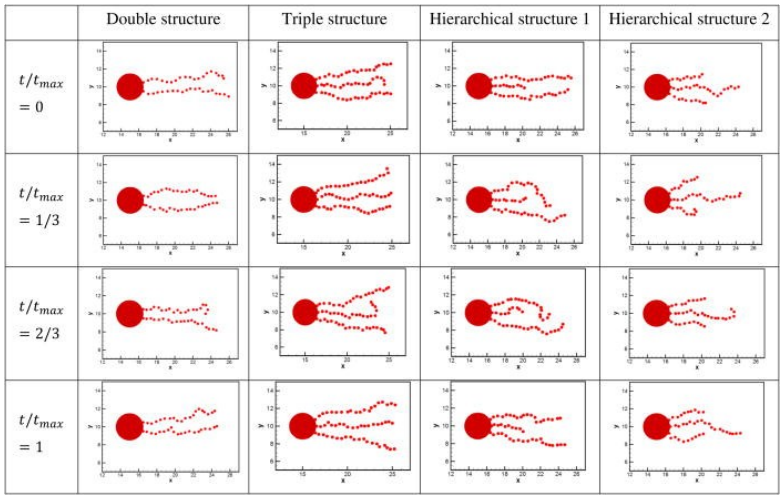

Figure 4. Multi-polymeric and hierarchical tail structures including double-tail, triple-tail, and hierarchical configurations [8].

The simulations demonstrate that multi-polymeric structures provide additional control over the wake dynamics and further influence the drag components. Among the investigated configurations, the triple-tail structure exhibits the highest overall performance, reducing the total drag coefficient by approximately 14.4%. In this case, both pressure and viscous drag components decrease simultaneously. Hierarchical structures show a more complex behavior, where viscous drag reduction may be accompanied by pressure drag enhancement, resulting in smaller net improvements. The obtained results demonstrate that flexible polymeric structures can serve as passive drag-control devices in low-Reynolds-number flows. The observed drag-reduction mechanisms are particularly relevant for the design of energy-efficient bio-inspired microrobots, microswimmers, and biomedical microdevices operating in confined microfluidic environments. Furthermore, this study highlights the ability of DPD simulations to capture the coupled fluid–polymer interactions responsible for these complex transport phenomena, providing valuable insight for the development of next-generation lab-on-a-chip and translational biomedical systems.

2. Rolling/Sliding Microdroplet Dynamics

The second case study presented in this workshop focuses on droplet transport and wettability dynamics in microfluidic environments. Understanding droplet motion on engineered surfaces is of fundamental importance for digital microfluidics, self-cleaning materials, anti-icing technologies, condensation heat transfer, and targeted drug delivery systems. Within the DPD framework, surface wettability is controlled by adjusting the conservative repulsion coefficients between fluid particles and wall image particles. By modifying the wall–fluid interaction strength, a wide range of equilibrium contact angles can be reproduced, from strongly hydrophilic surfaces ($\theta<90°$) to highly hydrophobic and superhydrophobic surfaces ($\theta>150°$). As illustrated in Figure 5, increasing the repulsion coefficient between water particles and wall particles increases the static contact angle and promotes hydrophobic behavior. Conversely, reducing this interaction strength results in enhanced wetting and lower contact angles. This capability enables DPD simulations to directly link microscopic interaction parameters to macroscopic wettability characteristics observed experimentally.

Hydrophilic surface

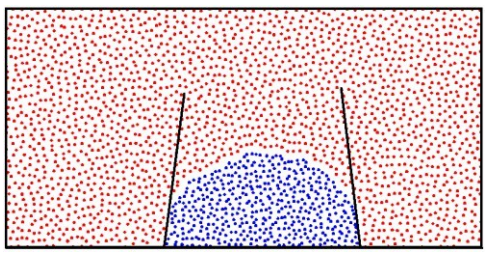

$a_{ew} = 23.09$ $a_{eB} = 36.13$ $\theta_s = 82°$

Hydrophobic surface

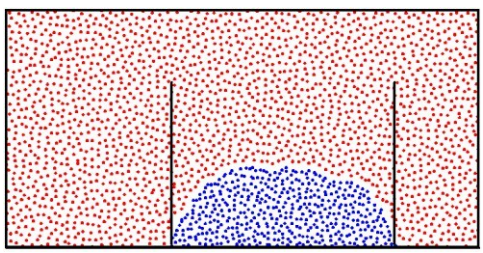

$a_{ew} = 25.81$ $a_{eB} = 51.62$ $\theta_s \approx 90°$

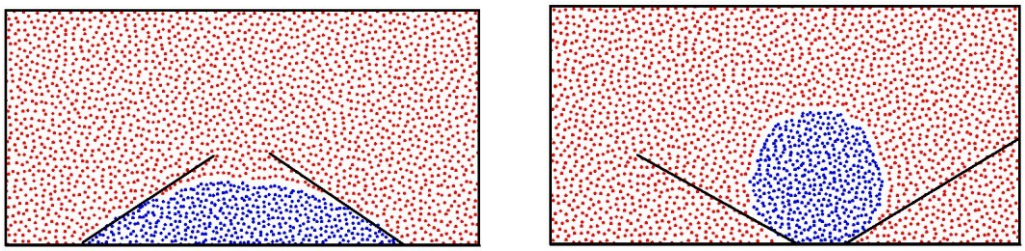

Figure 5. Hydrophobic/hydrophilic surfaces in the DPD method

To investigate the transport mechanisms of microscale droplets, a water droplet was placed inside an immiscible surrounding liquid (benzene) within a channel inclined by 5°. The simulations show that the droplet continuously migrates along the inclined surface and reaches the end of the computational domain after approximately 400 DPD time units (Figure 6(a)). The predicted droplet shapes and trajectories agree qualitatively with available experimental observations of droplets moving on low-energy surfaces. To distinguish between rolling and sliding motions, particle pathlines inside the droplet were analyzed (Figure 6(b)). The trajectories reveal that droplet motion is not purely translational nor purely rotational. Instead, individual particles exhibit simultaneous rotational and translational movements, producing a mixed transport mechanism that can be described as a rolling–sliding hybrid motion or a "dance-like" behavior.

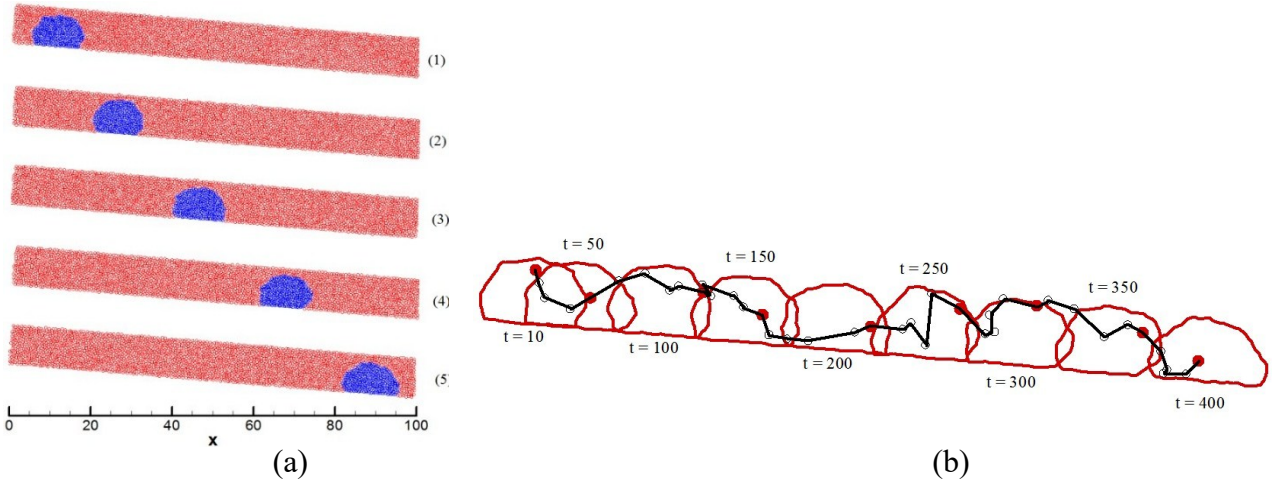

*Figure 6. (a) DPD simulation results of water (blue particles) inside benzene (red particles) on a hydrophobic inclined surface with an angle of **5°** at times (1) 10, (2) 100, (3) 200, (4) 300, and (5) 400 per DPD unit. (b) The pathline of a random particle of the water droplet in benzene*

The simulations were repeated for hydrophilic surfaces using identical geometrical and flow conditions. Representative results are shown in Figure 7. Unlike the hydrophobic case, the droplet spreads over the surface and exhibits significantly smaller contact angles. Stronger adhesion between the droplet and the wall leads to increased wetting and the formation of

residual liquid traces behind the moving droplet. The particle pathlines demonstrate that translational motion dominates over internal circulation. Consequently, droplet transport on hydrophilic surfaces is characterized primarily by slipping behavior, whereas rotational motion becomes substantially weaker. This observation highlights the critical role of wettability in determining the balance between rolling and sliding mechanisms.

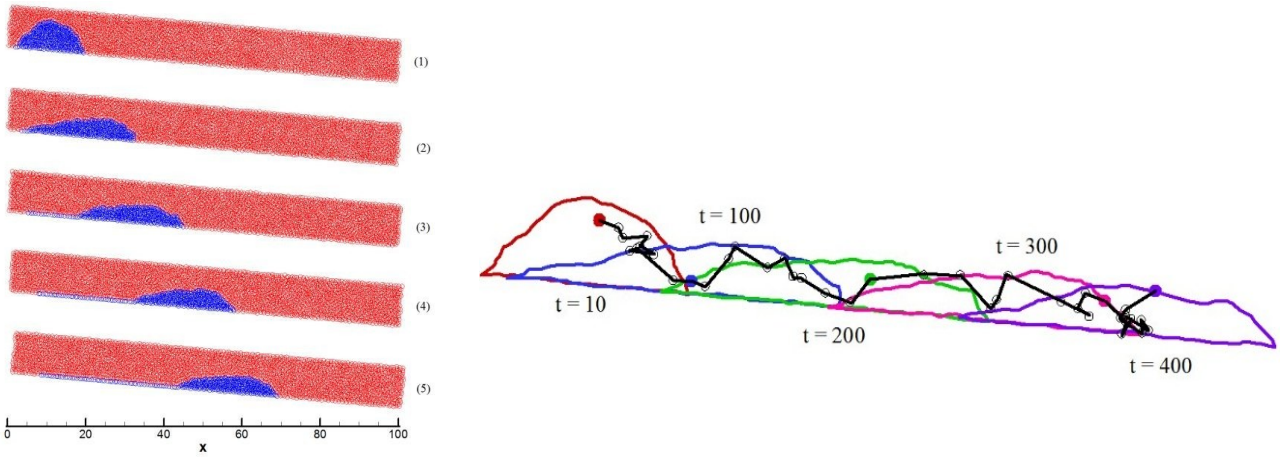

(a) (b)

*Figure 7. (a) DPD simulation results of water (blue particles) inside benzene (red particles) on a hydrophobic inclined surface with an angle of **5**° at times (1) 10, (2) 100, (3) 200, (4) 300, and (5) 400 per DPD unit. (b) The pathline of a random particle of the water droplet in benzene*

Beyond uniform wettability surfaces, the workshop also presents recent DPD simulations of smart surfaces with spatially varying wettability. On homogeneous surfaces, droplets remain nearly stationary unless external forces such as gravity or pressure gradients are applied. However, introducing a wettability gradient generates an imbalance in surface energy and contact angle along the droplet interface. The simulations demonstrate that droplets spontaneously migrate toward regions of higher wettability without requiring any external actuation. This passive transport mechanism provides a promising strategy for controlled liquid manipulation in microfluidic devices. Such wettability-gradient-driven motion has significant potential for:

- Passive microfluidic pumping,
- Lab-on-a-chip fluid transport,
- Anti-icing and de-icing technologies,
- Self-cleaning surfaces,
- Biomedical sample handling,
- Targeted drug-delivery platforms.

The presented results collectively demonstrate that mesoscale fluid transport is governed by a complex interplay between surface forces, interfacial tension, and fluid–fluid interactions. DPD simulations successfully capture these coupled phenomena while maintaining computational efficiency significantly higher than atomistic molecular dynamics simulations. Furthermore, the particle-level information available in DPD provides direct access to internal droplet dynamics that are difficult to observe experimentally. This capability enables the identification of rolling, sliding, and mixed transport modes and offers valuable insight for the rational design of advanced microfluidic and biomedical systems.

Conclusion

This workshop demonstrates how Dissipative Particle Dynamics (DPD) serves as an effective coarse-grained simulation framework that bridges molecular-scale interactions and continuum-scale transport phenomena in microfluidics, lab-on-a-chip systems, and translational biomedical technologies. By representing clusters of molecules as interacting particles, DPD captures hydrodynamic behavior, thermal fluctuations, interfacial dynamics, and fluid–structure interactions while maintaining computational efficiency significantly higher than atomistic molecular dynamics simulations. Through a series of representative case studies, the workshop highlights the versatility of DPD in addressing complex mesoscale transport problems. Bio-inspired microswimmer simulations reveal that flexible polymeric tails strongly modify wake dynamics and pressure distributions, leading to significant drag reduction. The results show that longer polymeric tails and multi-tail configurations can substantially decrease total drag, providing valuable design principles for energy-efficient microrobots and biomedical microswimmers.

The workshop also demonstrates the capability of DPD to model multiphase droplet dynamics and surface wettability effects. Simulations of droplets on inclined hydrophobic and hydrophilic surfaces show that droplet motion is neither purely rolling nor purely sliding. Instead, droplets exhibit a coupled rolling–sliding behavior whose relative contribution depends on wettability, fluid properties, and interfacial interactions. Furthermore, simulations on smart surfaces with spatial wettability gradients illustrate how passive droplet transport can be achieved through surface-energy variations without external actuation, offering promising opportunities for anti-icing technologies, self-cleaning surfaces, passive microfluidic pumping, and targeted drug-delivery applications. Overall, the presented examples demonstrate that DPD provides unique insight into the nonlinear coupling between fluids, interfaces, polymers, droplets, and biological structures. As microfluidic and biomedical technologies continue to evolve toward increasingly complex and multifunctional systems, DPD emerges as a powerful predictive and design tool capable of connecting molecular physics to engineering-scale performance. The methodologies and applications discussed in this workshop provide a foundation for future developments in smart microfluidic devices, lab-on-a-chip platforms, biomimetic microrobots, and next-generation translational biomedical technologies.

References:

[1] Gurkan UA, Wood DK, Carranza D, Herbertson LH, Diamond SL, Du E, et al. Next generation microfluidics: fulfilling the promise of lab-on-a-chip technologies. Lab Chip 2024;24:1867–74.

[2] Xu T, Hu J, Liu C, Bai H, Zhang L, Zhuang W, et al. Lab-on-a-chip technologies: The future of precision medicine and high-throughput biomolecular analysis. Biomedical Analysis 2025;2:159–78.

[3] Hoogerbrugge PJ, Koelman JMVA. Simulating microscopic hydrodynamic phenomena with dissipative particle dynamics. EPL (Europhysics Letters) 1992;19:155–60.

[4] Groot RD, Warren PB. Dissipative particle dynamics: Bridging the gap between atomistic and mesoscopic simulation. J Chem Phys 1997;107:4423–35.

[5] Curk T. Dissipative particle dynamics for coarse-grained models. J Chem Phys 2024;160.

[6] Dingyi PAN, Guohui HU, Shuo C, Nhan P-T. Mesoscopic modeling of complex multiphase fluids: Dissipative particle dynamics (DPD) method and its applications. 力学进展 2024;54:173–201.

[7] Javan Nikkhah S, Vandichel M. Dissipative particle dynamics modeling in polymer science and engineering. Wiley Interdiscip Rev Comput Mol Sci 2025;15:e70018.

[8] Heyat Davoudian S, Javadi K. Flexible polymeric tail for micro robot drag reduction bioinspired by the nature microorganisms. Physics of Fluids 2022;34.

[9] Chen G, Yan J, Liang J, Zheng J, Wang J, Pang H, et al. Advances in Wettability-Engineered Open Planar-Surface Droplet Manipulation. Micromachines (Basel) 2025;16:893.

[10] Kiyani E, Kooshkbaghi M, Shukla K, Koneru RB, Li Z, Bravo L, et al. Characterization of partial wetting by CMAS droplets using multiphase many-body dissipative particle dynamics and data-driven discovery based on PINNs. J Fluid Mech 2024;985:A7.

[11] Chowdhury EH, Sohan MSH, Gonzalez-Valle CU, van Duin ACT, Ramos-Alvarado B. Understanding surface wettability: insights from experiments, molecular simulations, and first-principles theory. Nanoscale 2026;18:9469–516.

[12] Tiwari A, Abraham J. Dissipative-particle-dynamics model for two-phase flows. Physical Review E—Statistical, Nonlinear, and Soft Matter Physics 2006;74:056701.

[13] Goel H, Chandran PR, Mitra K, Majumdar S, Ray P. Estimation of interfacial tension for immiscible and partially miscible liquid systems by Dissipative Particle Dynamics. Chem Phys Lett 2014;600:62–7.

A Microfluidic Biosensor Platform for Monitoring Breast Cancer

Kaan Sönmez[1], Eren Zaman[2,3], Zeynep Nur Şahin[4], Hasancan Yağdoğan[3], Zeynep Sevdagül Türkoğlu[5], Emir Guzelsağaltıcı[6], İsmail Bütün[1,7,*], Ali Koşar[1,7,8,9,*]

[1] Faculty of Engineering and Natural Sciences, Sabancı University, İstanbul, Türkiye
[2] Eurasian Institute of Earth Sciences, İstanbul Technical University, İstanbul, Türkiye
[3] Faculty of Science and Letters, İstanbul Technical University, Istanbul, Türkiye
[4] Faculty of Science and Engineering, Sorbonne University, Paris, France
[5] Institute of Pure and Applied Sciences, Marmara University, Istanbul, Türkiye
[6] Faculty of Chemical and Metallurgical Engineering, Yıldız Technical University, Istanbul, Türkiye
[7] Sabancı University Nanotechnology Research and Application Centre (SUNUM), İstanbul, Türkiye
[8] Center of Excellence for Functional Surfaces and Interfaces for Nano-Diagnostics (EFSUN), Sabancı University, İstanbul, Türkiye
[9] Turkish Academy of Sciences (TÜBA), Çankaya, 06700, Ankara, Türkiye
[*] Corresponding Authors: İsmail Bütün; ismailbutun@sabanciuniv.edu, Ali Koşar; Email: kosara@sabanciuniv.edu

Abstract—In this study, it is aimed to create a cost-effective microfluidic chip integrated immuno-electrochemical biosensing platform. The system is ideally suited for convenient, real-time diagnostics in point-of-care settings. The primary function of the sensor kit is to establish a closed system using a microfluidic chip that enables the development of a sensing device that requires only a few microliters sample volume. The concentration of biomarkers, captured by antibodies inside the microfluidic chip, was monitored using the electrochemical impedance spectroscopy technique. The surface was functionalized explicitly for the targeted biomarker, namely CA 27-29 Biomarker, and noticeable changes in the biomarker concentration occur as it becomes captured onto the surface which leads to distinct variations in both the real and imaginary parts of the impedance and changes in the overall impedance magnitude. Consequently, it can be concluded that the chosen surface modifications and biomarkers effectively validate the biosensor's performance that we reached the 0.1kIU/mL detection limit. Here, we can indicate that the label-free detection and cost-effective

fabrication is the advantage over the conventional methods. This innovative system aims to significantly advance personalized prognosis and diagnosis, offering ease of use in clinical environments and at-home applications.

Keywords—microfluidic biosensor; breast cancer; Lab-on-a-Chip; electrochemical impedance spectroscopy; biomarkers.

I. Introduction

Breast cancer poses significant diagnostic and follow-up challenges in the global healthcare system due to heterogeneous subtypes and metastatic potential [1]. Current diagnostic methods such as mammography, magnetic resonance imaging (MRI) and biopsy face limitations such as invasiveness, high cost, radiation exposure, and low sensitivity [2]. Accurate diagnosis of the cancer stage and accessible tracking tools are critical for success in treatment. Conventional blood tests are neither time-effective nor effort-efficient due to heterogeneous biomarker composition depending on the stage, type, and complex laboratory requirements [3]. In this context, it has become clear that there is a growing need for a non-intrusive and quantitative biosensor platform designed specifically for point-of-care applications. Thus, we developed a microfluidic chip-based immuno-electrochemical biosensor displayed in Fig.1. Label-free and rapid detection and comprehensive biomarker panel address the diagnostic gap in the literature related to minimally invasive, point-of-care breast cancer analysis.

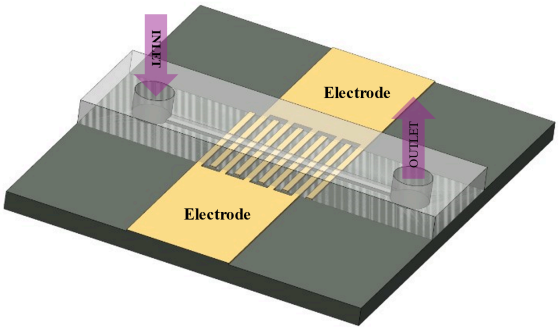

Fig.1. Interdigitated electrochemical biosensor integrated into microfluidic chips.

II. Current Diagnostic Challenges and Emerging Solutions

Breast cancer accounts for a major share of cancer cases for women worldwide, making early detection essential for effective treatment [4]. Conventional diagnostic tools such as

mammography, MRI, ultrasound, and biopsy often present challenges, including significant costs, exposure to radiation, and the possibility of incorrect results [5]. Therefore, there is a significant need for non-invasive, low-cost, and point-of-care diagnostic approaches. To exemplify, blood tests may satisfy such requirements since changes in the concentration of certain biomarkers in blood provide key information about the status of breast cancer. Higher concentration of the biomarker CA 27-29 yields clinically relevant information as much as the biomarker CA 15-3 in terms of sensitivity and specificity about the progression and metastatic spread of the cancer [6, 7]. In this study, the FDA-recognized breast cancer biomarker CA 27-29 was experimentally evaluated and found to be linked with disease recurrence and prognosis [8].

The combination of electrochemical sensors with the microfluidic technology opens a new perspective for sensing techniques. Microfluidic systems offer high-resolution analysis by minimizing sample and reagent consumption [9]. In this study, a microfluidic chip integrated with gold electrodes patterned on silicon surface was utilized for measuring the concentration changes of the target biomarker. Gold electrodes were selected for their high electrical conductivity, inherent biocompatibility, and surface chemistry, which is appropriate to effectively immobilize antibodies [10]. The electrochemical impedance spectroscopy (EIS) was used to measure biomarker levels. Unlike many conventional methods, this technique allows for quantitative detection without relying on fluorescent tags or enzyme-based labeling [11]. Therefore, to overcome the limitations of traditional diagnostic methods, we provided a new electrochemical biosensor aimed at improving cancer detection. This sensor offers a new approach, offering the early diagnosis and personalized tracking of breast cancer.

III. MATERIAL AND METHOD

A. Materials

The polydimethylsiloxane (PDMS) base and curing agent (Sylgard 184, Dow Corning) were used to fabricate microfluidic chips. The surface of the gold electrodes was modified and targeted to detect cancer biomarkers using the following materials:11-mercaptoundecanoic acid (MUA), N-(3-Dimethylaminopropyl)-N′-ethylcarbodiimide hydrochloride (EDC), N-Hydroxysuccinimide (NHS), phosphate buffered saline (PBS, pH 7. 4) Cancer Antigen

27-29 (CA 27-29, Creative Diagnostics, LOT:NC2403511) and mouse anti-CA 27-29 monoclonal antibody (Creative Diagnostics, LOT: JW07B231) were used.

B. Methods

a) Preparation of Microfluidic Chips

The proposed microfluidic platform has 2 main parts: microfluidic channels and electrodes that are fabricated by using process flow [12] displayed in Fig.2. The process begins with thoroughly cleaning the wafer substrate (University Wafer) to ensure a pristine surface. First, the substrate was cleaned with acetone, then rinsed with isopropyl alcohol (IPA, 2-Propanol CAS 67-63-0, Merck) and deionized water (DI). After cleaning, the wafer was dried using a stream of nitrogen and then dehydrated by baking on a hot plate at 120°C for 3 minutes. Next, a layer of AZ5214 photoresist (MicroChemicals GmbH) was coated using a spin coater (Laurell Technologies) at 4000 rpm for 45 seconds. The coated wafer was then soft baked at 110°C for 60 seconds to prepare it for exposure. Photolithography process was performed using a Midas mask aligner, where the sample was exposed to UV light through a photomask at an intensity of 25 mW/cm² for 8 seconds. This was followed by a post-exposure bake at 110°C for 45 seconds, then a flood exposure for 60 seconds under the same light intensity to complete the image reversal process. Development was carried out using MIF 726 developer (MicroChemicals GmbH), revealing the desired pattern. Finally, the electrodes were formed using a lift-off process after depositing a thin metal stack (50 nm of gold) on top of a 10 nm chromium adhesion layer. Then, the microchannel fabrication [13] (Fig. 2. f–i) began by coating SU-8 3050 negative photoresist (Microchem Corp.) using a spin coater at 1000 rpm for 60 seconds to create a 100 µm thick layer on a cleaned silicon wafer (University Wafer). The wafer was then soft baked at 95°C for 20 minutes, exposed to UV light (325 nm) for 12 seconds using a Midas Mask Aligner, and post-baked at 95°C for 5 minutes. The development process was carried out in a developer solution (SU8 developer) with gentle stirring for 5–8 minutes until the microstructures were visible. The wafer was then rinsed with IPA, dried with nitrogen. The SU-8 molds were used for PDMS casting, where a 10:1 mixture of PDMS base and curing agent was poured over the mold, degassed in a vacuum chamber, and cured in an oven at 75°C for three hours.

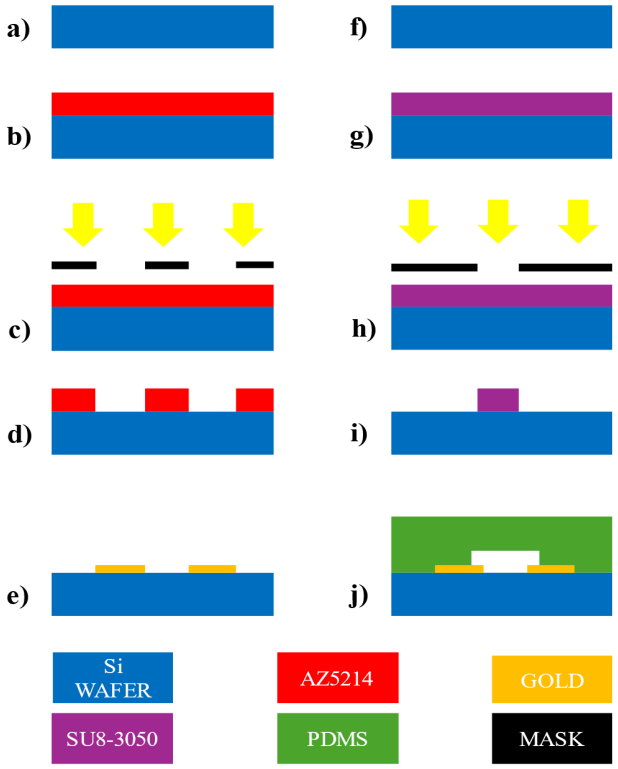

Fig.2. Process flow to fabricate electrochemical biosensor platform. a) silicon wafer, b) AZ5214 photoresist coating on the silicon wafer, c) UV lithography, d) developing, e) metal (Au) deposition, f) silicon wafer, g) SU8-3050 photoresist coating, h) UV lithography, i) developing process, j) oxygen plasma activated bonding process. The colors with text (legends) at the bottom represent the materials that are used during fabrication process.

b) Chip Assembly

In the final step (Fig.2. j), the PDMS channel and the electrochemical chip were bonded by first treating both surfaces with oxygen plasma for one minute using a Harrick plasma cleaner [14]. Then, activated surfaces were carefully aligned and contacted to form a strong, irreversible covalent bond, resulting in microfluidic integrated electrochemical biosensor.

c) Antibody Coating and Antigen Binding on a Microfluidic Channel Surface

1) MUA (11-Mercaptoundecanoic Acid) Coating:

100mM MUA solution (prepared in 95% ethanol) was applied to the surface and incubated for 20 h at room temperature in the dark. After treatment, the surface was washed 3 times with 10mM PBS (pH 7.4).

2) EDC/NHS Activation:

The chip surface was coated with a solution containing 0.1M EDC and 0.4M NHS in PBS and incubated for 30 min at room temperature. The surface was washed 3 times with PBS to remove excess reagents.

3) Antibody Binding:

CA 27-29 Monoclonal antibodies were diluted to 100µg/mL in PBS and 50 mL was applied to the chip channels. Overnight incubation at 4ºC was planned. Due to time constraints, an alternative incubation of 1-2 hours was also considered. To remove the unbound antibodies, the chip channels were cleaned by PBS solution.

4) Preparation of Protein Solutions:

CA 27-29 biomarker stock solution (10kIU/mL) was diluted into 1/10 (named as Antigen100 P2), 1/50 (named as Antigen50 P2), 1/100 (named as AntigenP2) of initial concentration with 10mM PBS (pH-7.4). The diluted solutions were applied to the chip surface and incubated for 15 minutes at room temperature

d) Sensor Measurement Procedure.

The EIS measurements were performed, two-electrode method with the electrode pads shown in schematic in Fig.1., using PARSTAT MC1000 Potentiostat/Galvanostat and obtained data were first analyzed by Kramers-Kronig relations using Linear Kramers-Kronig Valdity Test developed by Institut für Angewandte Materialien Wekstoffe der Elektrotechnik in MATLAB environment. The surface functionalization and antigen detection were successfully achieved through the microfluidic chip, by following the parameters outlined in Table 1.

TABLE I. EXPERIMENTAL PARAMETERS

Coating material	Flow rate	Time delay
	uL/min	h
MUA	20	24
Antibody	20	1
Antigen P2	20	1
Antigen50 P2	20	1
Antigen100 P2	20	1

IV. RESULTS AND DISCUSSION

In this study, the performance of the microfluidic biosensor platform developed for detecting breast cancer protein biomarkers was evaluated using the electrochemical impedance spectroscopy (EIS). The biosensor surface was modified with MUA, followed by covalent antibody immobilization using EDC/NHS activation. These steps enhanced the biocompatibility of the surface and ensured stable antibody immobilization.

After finalizing the required modification steps, the EIS measurements started from 1MHz to 0.1Hz with 20mV amplitude for each biomolecule coating. The Kramers-Kronig test was applied to the acquired data, and results with an error margin below 5% were selected for further analysis. Based on these validated results, a reliable frequency range of 150 kHz to 100 Hz was identified, Fig.3-a.

EIS measurements in Fig.3 confirm the antigen-antibody interactions, where Re(Z) is reduced to more than 2kΩ, occurring on the biosensor surface, while the protein antigens are being captured by antibodies. The highest impedance in the real axis, indicating the highest charge transfer resistance (Rct), is related to MUA coating, which serves as the baseline surface modification. When the antibodies are immobilized, and antigens interact with the surface, a clear shift in the impedance, 1kHz to 10kHz, appears, confirming that biochemical recognition occurs. As the concentration of antigen increases, there are progressive changes in the impedance, mostly in -Im(Z), proving both concentration-dependent binding and the sensitivity of the system. The immobilization of antibodies significantly reduces the charge transfer resistance, which is attributed to the enhanced surface conductivity. Further addition of proteins with differing concentrations named as antigens at increasing concentrations may lead to a progressive reduction in the Rct. The observed impedance trend with increasing concentration indicates that the formation of a thicker biomolecular layer could enhance the charge transfer, thereby reducing the overall impedance [15]. According to the results, 0.1 kUI/mL could be limit of detection (LoD) in for the sensor that is regarded as a highly efficient sensing performance in this case.

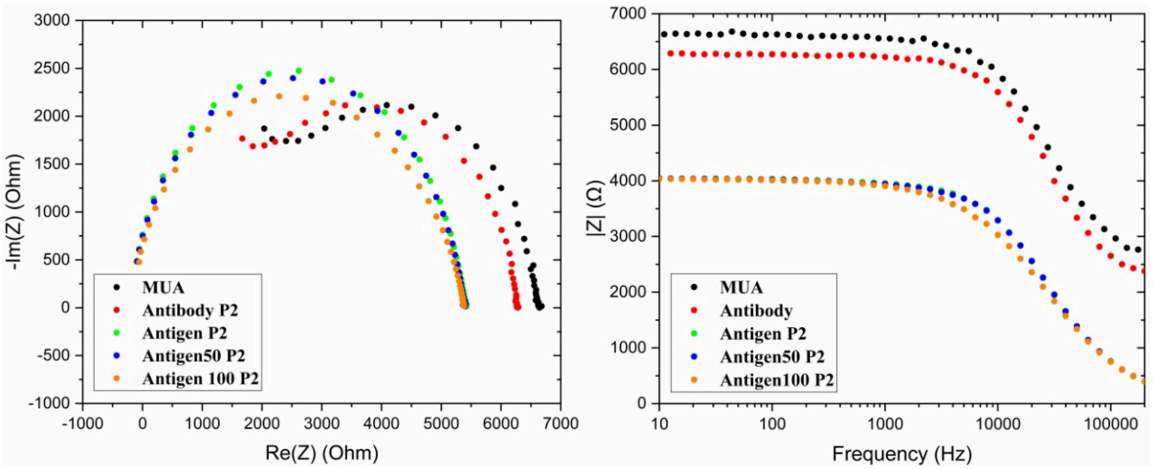

a) **b)**

Fig.3. Electrochemical biosensor responses; a) impedance response of biomarker concentrations in real and imaginary axis and b) concentration effect on the magnitude of the impedance changing with frequency.

According to our results, microfluidic biosensor platform shows great promise for point-of-care breast cancer diagnostics by enabling minimally invasive, portable, and rapid biomarker detection. The distinct impedance profiles obtained can potentially correlate with biomarker levels and cancer stages. However, validation with a larger panel of biomarkers and clinical samples is essential before clinical translation. Future work will focus on optimizing the surface chemistry, expanding the biomarker detection capabilities, integrating multiplexing, and employing advanced data analysis methods such as equivalent circuit modeling and AI to enhance the biosensor's performance and facilitate its widespread clinical adoption.

V. Conclusion

Breast cancer remains as a critical global health challenge, necessitating improved diagnostic tools being both sensitive and accessible. This study addresses the limitations of existing methods by developing a microfluidic biosensor platform designed for the rapid and accurate detection of breast cancer biomarkers. Our results, EIS, demonstrated the platform's high sensitivity and specificity, confirming its reliability for potential clinical applications. Specifically, the EIS analysis effectively demonstrates the change in the impedance corresponding to various concentrations of the CA 27-29 biomarker, indicating the capability

of biosensors to quantitatively analyze biomarker levels. This technology can lead to a suitable tool for early diagnosis and personalized treatment strategies, potentially revolutionizing point-of-care diagnostics. In the future, we anticipate this platform to be further refined and validated in use in diverse clinical settings, including screenings and personalized monitoring, thereby significantly contribute to improving the patient's health.

REFERENCES

[1] L. Kalinowski, J. M. Saunus, A. E. McCart Reed, and S. R. Lakhani, "Breast Cancer Heterogeneity in Primary and Metastatic Disease," in Breast Cancer Metastasis and Drug Resistance: Challenges and Progress, A. Ahmad Ed. Cham: Springer International Publishing, 2019, pp. 75-104.

[2] M. Popiel, D. Mróz-Klimas, R. Kasprzak, and M. Furmanek, "Mammary carcinoma - current diagnostic methods and symptomatology in imaging studies," (in eng), Pol J Radiol, vol. 77, no. 4, pp. 35-44, Oct 2012, doi: 10.12659/pjr.883627.

[3] U. Testa, G. Castelli, and E. Pelosi, "Breast Cancer: A Molecularly Heterogenous Disease Needing Subtype-Specific Treatments," Medical Sciences, vol. 8, no. 1, p. 18, 2020. [Online]. Available: https://www.mdpi.com/2076-3271/8/1/18.

[4] A. Sinha, M. N. B. J. Naskar, M. Pandey, and S. S. Rautaray, "Challenges to the Early Diagnosis of Breast Cancer: Current Scenario and the Challenges Ahead," SN Computer Science, vol. 5, no. 1, p. 170, 2024/01/08 2024, doi: 10.1007/s42979-023-02534-1.

[5] V. Freitas, "Optimizing breast MRI diagnosis: the Kaiser Score's impact on reducing unnecessary biopsies," European Radiology, vol. 35, no. 3, pp. 1502-1503, 2025/03/01 2025, doi: 10.1007/s00330-024-11325-y.

[6] R. Ranjit, V. K. Bozhenko, and E. Aleksandrovna Kudinova, "Molecular Diagnosis of Breast Cancer," in Molecular Diagnostics of Cancer, P. P. Piccaluga Ed. Rijeka: IntechOpen, 2024.

[7] P. S. Frenette, M. P. Thirlwell, M. Trudeau, D. M. P. Thomson, L. Joseph, and J. S. Shuster, "The Diagnostic Value of CA 27-29, CA 15-3, Mucin-Like Carcinoma Antigen,

Carcinoembryonic Antigen and CA 19-9 in Breast and Gastrointestinal Malignancies," Tumor Biology, vol. 15, no. 5, pp. 247-254, 2009, doi: 10.1159/000217898.

[8] E. R. Sauter, "Reliable biomarkers to identify new and recurrent cancer," European journal of breast health, vol. 13, no. 4, p. 162, 2017.

[9] K. B. Mogensen, H. Klank, and J. P. Kutter, "Recent developments in detection for microfluidic systems," ELECTROPHORESIS, vol. 25, no. 21-22, pp. 3498-3512, 2004, doi: https://doi.org/10.1002/elps.200406108.

[10] Y. Li, H. J. Schluesener, and S. Xu, "Gold nanoparticle-based biosensors," Gold Bulletin, vol. 43, no. 1, pp. 29-41, 2010/03/01 2010, doi: 10.1007/BF03214964.

[11] J. S. Daniels and N. Pourmand, "Label-Free Impedance Biosensors: Opportunities and Challenges," Electroanalysis, vol. 19, no. 12, pp. 1239-1257, 2007, doi: https://doi.org/10.1002/elan.200603855.

[12] M. Zamani, C. M. Klapperich, and A. L. Furst, "Recent advances in gold electrode fabrication for low-resource setting biosensing," Lab on a Chip, 10.1039/D2LC00552B vol. 23, no. 5, pp. 1410-1419, 2023, doi: 10.1039/D2LC00552B.

[13] B. H. Jo, L. M. V. Lerberghe, K. M. Motsegood, and D. J. Beebe, "Three-dimensional micro-channel fabrication in polydimethylsiloxane (PDMS) elastomer," Journal of Microelectromechanical Systems, vol. 9, no. 1, pp. 76-81, 2000, doi: 10.1109/84.825780.

[14] A. Tony et al., "A Preliminary Experimental Study of Polydimethylsiloxane (PDMS)-To-PDMS Bonding Using Oxygen Plasma Treatment Incorporating Isopropyl Alcohol," Polymers, vol. 15, no. 4, p. 1006, 2023. [Online]. Available: https://www.mdpi.com/2073-4360/15/4/1006.

[15] M. Pali and I. I. Suni, "Impedance Detection of 3-Phenoxybenzoic Acid Comparing Wholes Antibodies and Antibody Fragments for Biomolecular Recognition," Electroanalysis, vol. 30, no. 12, pp. 2899-2907, 2018, doi: https://doi.org/10.1002/elan.201800495.

Laser-Induced Synthesis of Co-MOF-Based Electrochemical Sensor for High-Performance Dopamine Detection

Dilek Soyler[1]*, Saliha Mutlu[2,3], Bülend Ortaç[3], Ali Karatutlu [3], Taylan Görkan[3], Engin Durgun[3], Jelena Lillepäg[4], Volkan Filiz[4], Nergis Arsu[5], Sevil Savaskan Yılmaz[2,3], Saniye Soylemez [1]

[1]Necmettin Erbakan University, Department of Biomedical Engineering, Konya, 42090, Türkiye

[2]Karadeniz Technical University, Faculty of Science, Department of Chemistry, Trabzon 61080, Türkiye

[3]Bilkent University, Institute of Materials Science Nanotechnology and National Nanotechnology Research Center (UNAM), Ankara 06800, Türkiye

[4]Helmholtz-Zentrum Institute of Membrane Research, Hereon, Max-Planck-Str.1, 21502 Geesthacht, Germany

[5]Yildiz Technical University, Department of Chemistry, Davutpasa Campus, Istanbul 34220, Türkiye

The development of sensitive and selective electrochemical sensors for neurotransmitter monitoring is crucial for biomedical diagnostics and neurodegenerative disease management [1]. In this study, a cobalt-based metal–organic framework (Co-MOF) was synthesized via a rapid laser-induced synthesis (LIRS) method and applied as an electrocatalytic platform for dopamine detection. The laser-assisted approach enabled the rapid formation of highly crystalline Co-MOF structures, offering a scalable route for the fabrication of functional electrode materials [2].

The Co-MOF was deposited onto a graphite rod electrode (GE) to construct a GE/Co-MOF sensor. Electrochemical studies (CV and EIS) confirmed enhanced electron transfer kinetics and an increased electroactive surface area compared to the bare electrode. Differential pulse voltammetry (DPV) revealed strong electrocatalytic activity toward dopamine oxidation under physiological pH conditions. [3]

The sensor exhibited a linear detection range of 0.02–0.5 mM, a sensitivity of 121.61 µA mM^{-1} cm^{-2}, and a detection limit of 5.5 µM. High selectivity was observed against common

interfering species, along with excellent repeatability (%RSD = 1.85) and reproducibility (%RSD = 2.21). Practical applicability was demonstrated through dopamine detection in artificial human serum with satisfactory recovery values.

These results highlight laser-synthesized Co-MOFs as promising electrocatalytic materials for sensitive and reliable electrochemical biosensing applications.

Keywords: Electrochemical sensor, Dopamine sensing, Cobalt metal–organic framework (Co-MOF), Laser-induced synthesis, Differential pulse voltammetry.

References:

[1] Karim, A., Yasser, M., Ahmad, A., Natsir, H., Wahab, A. W., Fauziah, S., ... & Syahrir, M. (2024). A review: Progress and trend advantage of dopamine electrochemical sensor. *Journal of Electroanalytical Chemistry*, *959*, 118157.

[2] De Chiara, B., Del Duca, F., Hussain, M. Z., Kratky, T., Banerjee, P., Dummert, S. V., ... & Wolfrum, B. (2025). Laser-Induced Metal–Organic Framework-Derived Flexible Electrodes for Electrochemical Sensing. *ACS Applied Materials & Interfaces*, *17*(2), 3772-3784.

[3] Mutlu, S., Ortaç, B., Karatutlu, A., Gorkan, T., Durgun, E., Soyler, D., Soylemez, S., ... & Savaskan Yilmaz, S. (2026). High-Power Rapid Laser-Induced Synthesis of Multi-functional Cobalt Metal-Organic Framework With an Unprecedented Synthesis Efficiency. *Advanced Materials Technologies*, e02487.

Microfluidic Wet Spinning of Tubular Vessel for Organ-on-Chip Applications

Naz Celiktas[1], Omur Sert[2], Esra Erdal[1,4], Ozlem Yesil-Celiktas[2,5]

[1]Izmir Biomedicine and Genome Center (IBG), Dokuz Eylul University Health Campus, 35340, Izmir, Turkey

[2]Department of Bioengineering, Faculty of Engineering, Ege University, 35100, Izmir, Turkey

[4]Department of Medical Biology and Genetics, Faculty of Medicine, Dokuz Eylul University, 35340, Izmir, Turkey

[5]ODTÜ MEMS Center, 06530, Ankara, Turkey

Introduction

Perfusable microvascular networks have the potential to recapitulate convective transport while providing physiologically relevant three-dimensional vascular architecture. Current strategies for replicating these transport phenomena include 3D printing using sacrificial templates [1], the use of decellularized plant vasculature [2] and microfluidic approaches [3]. Among these, microfluidic technologies have advanced considerably through the integration of diverse microfabrication techniques and functional biomaterials, enabling the development of tissue constructs that more closely mimic the structural and functional characteristics of native tissues. Notably, the hydrogel-based fibers have been widely incorporated in organ-on-chip systems as muscle fibers or blood vessels, owing to their biocompatible nature. The 3D lumen-like structure of hydrogel-fibers allows perfusion within dense tissue constructs. Coating the fibers with human endothelial cells improves the functionality due to the development of capillary branches. In cancer research, the use of vessel-like-fibers allows the observation of metastatic cascades including intravasation, survival in blood stream and extravasation [4] or circulation of monocytes if immune cells are present [5]. Additionally, it is possible to study circulation of various exposomes in the blood stream in terms of inhalation [6] or digestion. Another important transport mechanism is endocrine signaling, which is essential for the maintenance of homeostasis within the body. This signaling pathway ensures the secreted hormones are transferred to the target cells or organs via blood circulation and feedback loops are triggered [7]. The physiological characteristics of vessels make them selective barriers for the exchange of nutrients, waste products and pharmaceutical ingredients. Vessel-on-a-chip models have been developed as in vitro models for the evaluation of transport properties for drug screening [8]. However, certain design parameters have to be considered. With respect to cellular architecture, biophysical cues can be used towards guiding cells. For instance, seeding endothelial cells in stiffer gels result in vessels with larger lumens, while soft environments provide branched capillary-like structures [9]. Another key factor for transportation through the walls of hollow fiber is porosity. The pore size should be sufficient enough for nutrient and waste exchange, while the pores should be interconnected [10] so that the cells can communicate. Porosity can be controlled by adjusting the polymer concentration, which also affects topography of hydrogels [9]. The next step is the integration of the fabricated and cellularized tubular vessel to the organ-on-chip platform.

There is a gap in the literature regarding the integration of perfusable vessel-like fibers to organ-on-chips for convective transportation in order to observe systematic effects of exposomes, particulate matters or therapeutic agents. The aim of this study is to fabricate a perfusable alginate fiber using microfluidics-assisted co-axial wet-spinning, where the inner wall of the fiber is seeded with human umbilical vein endothelial cells (HUVECs) to form the endothelial barrier.

Materials and Methods

Microfluidics-assisted co-axial wet-spinning was conducted in a laminar flow biosafety cabinet to ensure sterility throughout the experiment. The ratio of flow rates (shell/core) was optimized as Qs/Qc=2. The shell solution was prepared sterile by dissolving alginate (A) and GelMA (G) in HEPES at 37°C. Two different viscosities of alginate were used, a medium viscosity (≥2,000 cP, 2 % (25 °C)) and a low viscosity (4-12 cP, 1 % in H_2O (25 °C)). In addition, various ratios of alginate and GelMA (A/G) were mixed for further characterization analysis on spinnability and degradability. A two-step crosslinking strategy is required for the shell bioink (**Fig. 1**), initial ionic crosslinking, which is followed by UV to further crosslink GelMA. To trigger photocrosslinking, photoinitiator was mixed with the bioink prior to the wet-spinning process. Additionally, the bioink used in the shell compartment was mixed with HUVECs before loading bioinks to syringes. Gelatin was mixed with HEPES for the sacrificial core at 37 °C and filtered sterile after complete dissolution. After incubation at 37 °C, the hollow tubular fiber is obtained. Further characterizations and experiments with respect to spinnability and degradation were carried out.

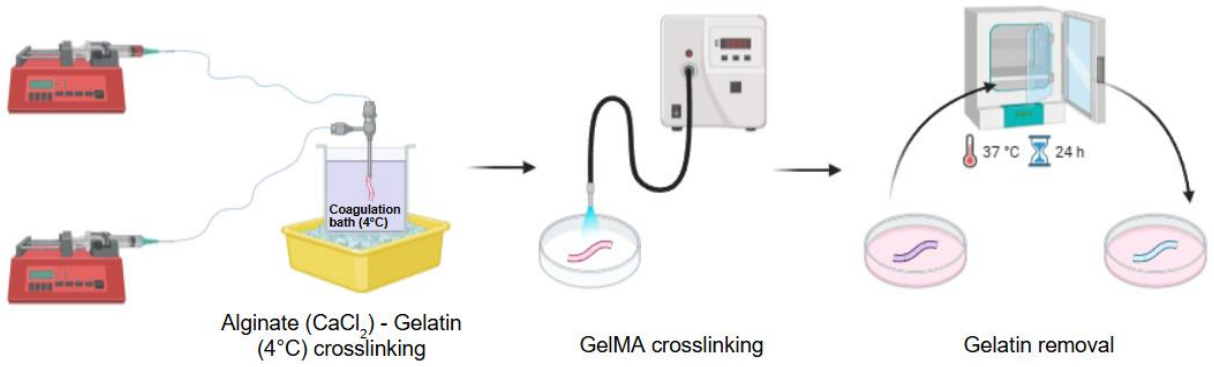

Figure 1. Process scheme of microfluidic-assisted co-axial wet spinning and two-step crosslinking method, ionic, followed by photocrosslinking.

Results and Discussion

Microfluidics-assisted co-axial wet-spinning was optimized according to spinnability and degradability of the bioinks. The shell compartment bioink, consisting of alginate and GelMA, were prepared with various formulations (A/G). Additionally, different viscosity alginates were used for the shell compartment. All bioinks used for the core compartment had the same formulation. Final viscosities of the bioinks prepared for the shell compartment were also compared. The colors in **Table 1**, white, green and yellow, represent low/poor, medium and high/good, respectively, for various properties of the formulations tested.

Both low and medium viscosity alginates were used in the formulations. The spinnability and the quality of the fibers spun with medium viscosity alginate were good. The fastest degradation was observed when the A/G ratio was 0.8, while the fiber lasting for the longest was spun with A/G ratio of 0.3. Although alginate and GelMA were added at similar percentages (w/v%) in 0.8, the overall content was not high enough to maintain the structure for long incubation time. For the ratios, 0.2 and 0.3, the viscosity changed significantly due to the addition of alginate and thus affected the degradability accordingly.

Table 1. For each of the listed features, white, green and yellow symbols indicate low/poor, medium and high/good, respectively.

Viscosity of Sodium Alginate	Formulation (A/G)	Viscosity of the final bioink	Filter (0.22 µm)	Spinnability	Degradability
Medium viscosity (≥2000 cP, 2 %, 25 °C)	0.8	○	○	🟡	🟡
	0.3	🟡	○	🟡	○
	0.2	🟢	○	🟡	🟢
Low viscosity (4-12 cP, 1 % in H_2O, 25 °C)	0.8	○	○	🟡	○
	0.6	○	○	🟡	○

Using low viscosity alginate was better in terms of ease of spinnability. In contrast to the highest A/G ratio shown for medium viscosity, the degradability was low for the low viscosity alginate. This was observed because the overall content of alginate and GelMA kept high since the possibility of obtaining a viscous ink was eliminated. However, filtering the bioink sterile was an issue. Thus, in order to decrease the viscosity, the ratio decreased. HUVECs embedded to low viscosity alginate fibers exhibited proper adhesion and proliferation.

Conclusion

The amount of medium viscosity sodium alginate used affected the degradability and viscosity of the final solution significantly. However, the impact of GelMA on degradability was also incontrovertible. Overall, medium viscosity alginate was not appropriate for wet spinning. On the other hand, low viscosity sodium alginate showed good spinnability and the fibers did not degrade for the time they were incubated. HUVECs embedded in low viscosity alginate forming the shell of the vessel can be utilized as a vasculature and integrated to the organ-on-chip platform.

Acknowledgement

The research fund provided by the Scientific and Technological Research Council of Turkey (TUBITAK) under grant number 120N422 is highly appreciated.

References

[1] Shi, J., Wan, Y., Jia, H., Skeldon, G., Cornelissen, D. J., Wesencraft, K., Wu, J., McConnell, G., Chen, Q., Liu, D., & Shu, W. (2025). *Angewandte Chemie International Edition, 64*, e202417510. https://doi.org/10.1002/anie.202417510

[2] Arslan, Y., Paradiso, A., Celiktas, N., Erdogan, T., Yesil-Celiktas, O., & Swieszkowski, W. (2023). Bioinspired microstructures through decellularization of plants for tissue engineering applications. *European Polymer Journal, 198*, 112415. https://doi.org/10.1016/j.eurpolymj.2023.112415

[3] Volpi, M., Paradiso, A., Walejewska, E., Gargioli, C., Costantini, M., & Swieszkowski, W. (2024). Automated microfluidics-assisted hydrogel-based wet-spinning for the biofabrication of biomimetic engineered myotendinous junction. *Advanced Healthcare Materials, 13*, 2402075. https://doi.org/10.1002/adhm.202402075

[4] Filiz, Y., Arslan, Y., Duran, E., Saglam-Metiner, P., Horozoglu, S., Paradiso, A., Martinez, D. C., Sabour-Takanlou, M., Heljak, M., Jaroszewicz, J., Biray-Avci, C., Swieszkowski, W., & Yesil-Celiktas, O. (2024). Decellularized plant-derived vasculature-on-a-chip interacting with breast cancer spheroids to evaluate a dual-drug therapy. *Applied Materials Today, 36*, 102015. https://doi.org/10.1016/j.apmt.2024.102015

[5] Sharifi, F., Htwe, S. S., Righi, M., Liu, H., Peietralunga, A., Yesil-Celiktas, O., Maharjan, S., Cha, B.-H., Shin, S.-R., Dokmeci, M. R., Vrana, N. E., Ghaemmaghammi, A., Khademhosseini, A., & Zhang, Y. S. (2019). A foreign body response-on-a-chip platform. *Advanced Healthcare Materials, 8*, 1801425. https://doi.org/10.1002/adhm.201801425

[6] Sert, O., Erdogan, T., Arslan, Y., & Yesil-Celiktas, O. (2026). A perfusable decellularized plant-based air-liquid-interface-on-a-chip for investigating inorganic dust aerosol exposure. *Scientific Reports, 16*, 3847. https://doi.org/10.1038/s41598-025-33930-7

[7] Hu, C., Chen, Y., Yin, X., et al. (2025). Pancreatic endocrine and exocrine signaling and crosstalk in physiological and pathological status. *Signal Transduction and Targeted Therapy, 10*, 39. https://doi.org/10.1038/s41392-024-02098-3

[8] Moses, S. R., Adorno, J. J., Palmer, A. F., & Song, J. W. (2021). Vessel-on-a-chip models for studying microvascular physiology, transport, and function in vitro. *American Journal of Physiology-Cell Physiology, 320*(1), C92–C105. https://doi.org/10.1152/ajpcell.00355.2020

[9] Yang, P., Boer, G., Snow, F., Williamson, A., Cheeseman, S., Samarasinghe, R. M., Rifai, A., Priyam, A., Elnathan, R., Guijt, R., Quigley, A., Kaspa, R., Nisbet, D. R., & Williams, R. J. (2025). Test and tune: Evaluating, adjusting and optimising the stiffness of hydrogels to influence cell fate. *Chemical Engineering Journal, 505*, 159295. https://doi.org/10.1016/j.cej.2025.159295

[10] Celiktas, N., Saglam-Metiner, P., Dogan, B., Alarcin, E., Gizli, N., & Yesil-Celiktas, O. (2025). Microcrystalline cellulose and boric acid functionalized hydrogel for differentiation of bone marrow stem cells: Biocompatibility, hemocompatibility and protein adsorption. *International Journal of Biological Macromolecules*, 146435. https://doi.org/10.1016/j.ijbiomac.2025.146435

Wall-Curvature Effects on Capillary-Rise Dynamics: Toward the Design of Biomimetic Artificial Xylem Systems

Zahra Yaqubi[1], Salar Heyat Davoudian[1,2], Ali Koşar[1,2,3]

[1] Faculty of Engineering and Natural Science, Sabanci University, 34956 Tuzla, Istanbul, Türkie

[2] Center of Excellence for Functional Surfaces and Interfaces for Nano-Diagnostics (EFSUN), Sabancı University, Orhanli, 34956 Tuzla, Istanbul, Turkey

[3] Sabanci University Nanotechnology Research and Application Center, 34956 Tuzla, Istanbul, Turkey

1. Introduction

The continuous increase in power density in modern electronic devices, batteries, and energy systems has created a growing demand for efficient passive thermal-management technologies. Among the available solutions, capillary-driven cooling systems such as heat pipes, vapor chambers, and wick-assisted evaporators have attracted significant attention because they can transport liquid without external pumping and remove heat through phase-change processes [1–4]. The performance of these systems strongly depends on their ability to continuously replenish liquid to the evaporation region. Insufficient liquid supply may lead to dry-out, reduced heat-transfer capability, and ultimately system failure [2,4].

Nature provides a remarkable example of passive liquid transport in the form of plant xylem. Through a hierarchical network of conduits, plants transport water from roots to leaves over considerable distances without mechanical pumps [5,6]. This transport process is driven primarily by capillary forces and pressure gradients generated within the xylem network. The high efficiency, self-sustainability, and robustness of this mechanism have inspired the development of artificial xylem systems for fluid transport, water harvesting, and thermal-management applications [7]. Recent advances in biomimetic thermal management have demonstrated that capillary structures inspired by natural transport systems can significantly improve liquid supply in evaporative cooling devices [8–11]. Biomimetic porous wicks, hierarchical capillary networks, and xylem-inspired transport pathways have been proposed to enhance liquid replenishment

and delay dry-out under high heat loads[8,9,11]. These studies suggest that geometry plays a critical role in determining the capillary pumping capability of the system. However, most existing investigations have focused on porous morphology, surface wettability, and multiscale structures, while the influence of channel curvature has received comparatively little attention.

Many biological transport systems do not consist of perfectly straight conduits. Curved and gradually varying geometries are commonly observed in plant vascular structures as well as in other natural liquid-transport systems such as spider silk and cactus spines [12,13]. Previous studies have shown that geometric variations can alter local capillary pressure and influence liquid motion [12,13]. Nevertheless, the isolated effect of wall curvature on capillary-rise dynamics remains insufficiently understood. In particular, it is still unclear how different curvature distributions affect the velocity of capillary rise when all other physical parameters are held constant. Addressing this question is essential for the rational design of curvature-guided artificial xylem systems. Before investigating thermal performance or fabricating biomimetic cooling devices, it is first necessary to establish a fundamental understanding of how wall geometry influences capillary-driven liquid transport. Therefore, the present study represents the first stage of a broader research framework aimed at developing bio-inspired artificial xylem structures for passive thermal management. The overall research roadmap consists of three consecutive phases. The first phase, addressed in this work, focuses on the capillary-rise behavior of a liquid in channels with different wall curvatures and aims to identify geometries that enhance capillary transport. The second phase will investigate heat-transfer and evaporation characteristics using the most favorable geometries identified in the first stage. The final phase will involve the fabrication and experimental evaluation of artificial xylem structures for passive cooling applications (see Fig. 1).

To achieve the objectives of the first phase, capillary rise is investigated in channels with linear, quadratic, and exponential wall profiles. These geometries introduce different curvature distributions while maintaining identical fluid properties, wall–fluid interactions, and boundary conditions. Consequently, wall geometry remains the only independent variable, allowing its influence on liquid transport to be isolated. The physical system is modeled using Dissipative Particle Dynamics (DPD), a mesoscale

simulation technique widely employed for studying multiphase flows, capillary phenomena, and interfacial dynamics [14–18]. DPD provides direct access to the evolution of liquid interfaces while preserving the hydrodynamic behavior necessary for analyzing capillary-driven motion.

The central research question of this study is:

How does wall curvature affect the velocity of capillary rise in a confined liquid system?

It is hypothesized that variations in wall curvature modify the local capillary-pressure distribution and consequently alter the upward velocity of the liquid front. Therefore, different wall geometries are expected to produce distinct capillary-rise dynamics even under identical physical conditions. Accordingly, the objectives of this work are:

1. To investigate capillary rise in channels with different wall curvatures using Dissipative Particle Dynamics.
2. To compare the evolution of liquid-front position and capillary-rise velocity in linear, quadratic, and exponential geometries.
3. To identify wall geometries that enhance capillary-driven liquid transport.
4. To establish a physical foundation for the future development of biomimetic artificial xylem cooling systems.

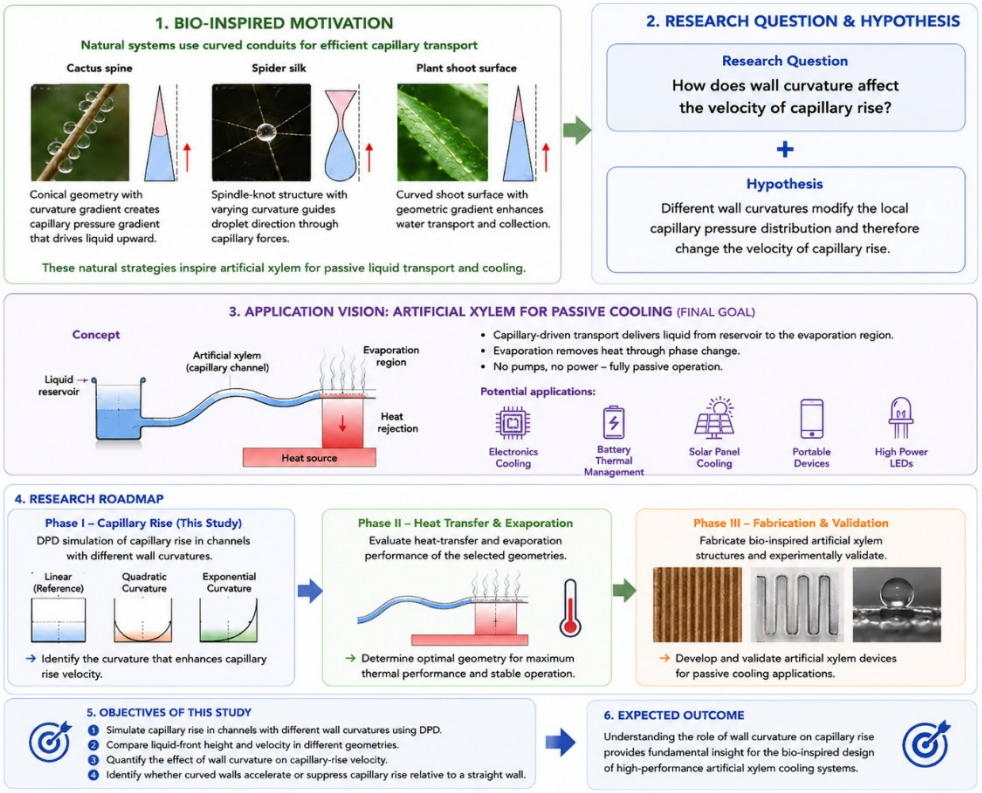

Fig. 1. Bio-inspired motivation and research framework of the present study.

2. Methodology

In this study, capillary rise in channels with different wall curvatures is simulated using the Dissipative Particle Dynamics (DPD) method. DPD is a coarse-grained mesoscale simulation technique derived from Molecular Dynamics (MD), in which a group of molecules is represented by a single computational particle. This approach significantly reduces computational cost while preserving hydrodynamic interactions, thermal fluctuations, and interfacial phenomena. The motion of each particle is governed by Newton's second law:

$$\frac{dr_i}{dt} = V_i \quad , \quad \frac{dV_i}{dt} = f_i,$$

where r_i, V_i, and f_i indicate the position, velocity, and forces vector per unit mass, respectively.

The total interaction force between two particles consists of three contributions:

$$F_{ij} = F_{ij}^{C} + F_{ij}^{D} + F_{ij}^{R}$$

where:

- F_{ij}^{C} is the conservative force governing thermodynamic behavior and phase separation,
- F_{ij}^{D} is the dissipative force representing viscous effects,
- F_{ij}^{R} is the random force accounting for thermal fluctuations.

For multiphase systems, the conservative force coefficient a_{ij} is adjusted to control the immiscibility between fluid phases and to generate a stable liquid–liquid interface.

- **Boundary Conditions**

Two types of boundary conditions are employed:

1. Wall boundary condition for solid walls, implemented using mirror particles outside the computational domain. This approach enforces the no-slip condition at the wall.
2. Periodic boundary condition in the streamwise direction, where particles leaving one side of the domain re-enter from the opposite side with unchanged properties. This eliminates artificial boundary effects and preserves bulk flow behavior.

- **Time Integration**

The governing equations are integrated using the velocity-Verlet scheme, which is widely used in DPD simulations because of its simplicity, numerical stability, and time reversibility. The integration procedure consists of:

1. Position update,
2. Intermediate velocity calculation,
3. Final velocity correction.

Following the recommendation of Groot and Warren, the integration parameter is set to λ=0.65 to ensure stable particle trajectories and accurate momentum conservation.

- **Simulation Strategy**

Three channel geometries are considered: linear ($y = 0.4x$), quadratic ($y = 0.008x^2$), and exponential ($y = 20\frac{\exp(\frac{3x}{50})-1}{\exp(3)-1}$) walls (see Fig. 2). All simulations use identical fluid properties, wettability conditions, and boundary conditions. Gravity is neglected in order to isolate capillary effects. Consequently, wall geometry is the only varying parameter, allowing a direct assessment of its influence on capillary-rise dynamics.

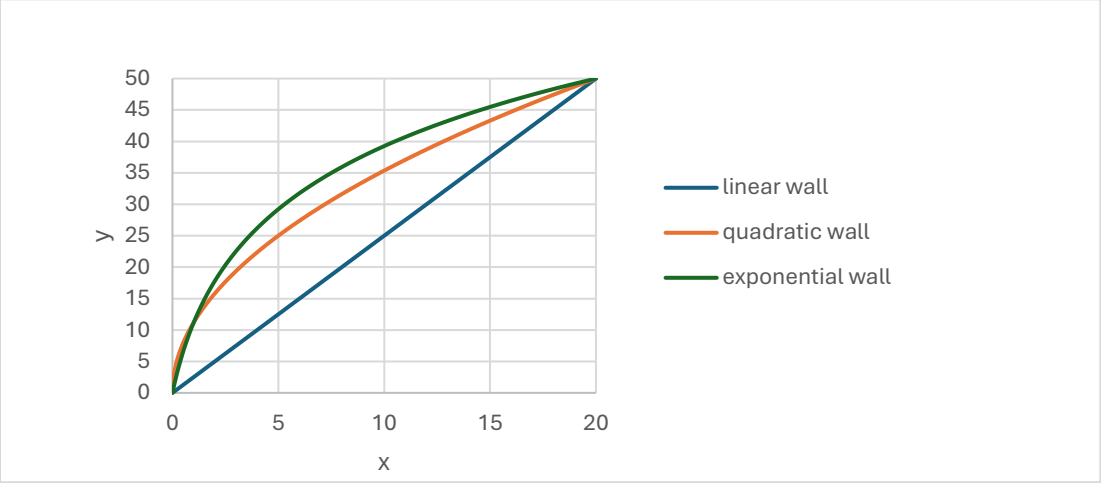

Fig. 2. Different curvature profiles, used in this simulation

Initially, the lower region of the channel is occupied by a wetting liquid, while the remaining domain is filled with a second immiscible liquid. The primary quantity of interest is the time-dependent tip location, which is used to characterize the liquid propagation rate and compare the transport performance of different channel geometries. In addition, the evolution of the liquid–liquid interface, droplet morphology, and internal flow dynamics are monitored throughout the transport process. To reproduce capillary-dominated transport conditions, gravitational effects are neglected. Furthermore, two immiscible liquids with relatively similar densities are employed to minimize buoyancy effects and isolate the influence of interfacial forces, wettability, and channel geometry. This configuration also provides a practical platform for future experimental validation of the numerical results.

3. Results and Discussion

Fig.3 compares the final liquid configurations obtained for the three channel geometries investigated in this study, namely the linear, quadratic, and exponential wall profiles. Since all simulations were performed using identical fluid properties, wall–fluid interaction parameters, and boundary conditions, any differences in the liquid behavior can be attributed solely to the geometric characteristics of the channel walls.

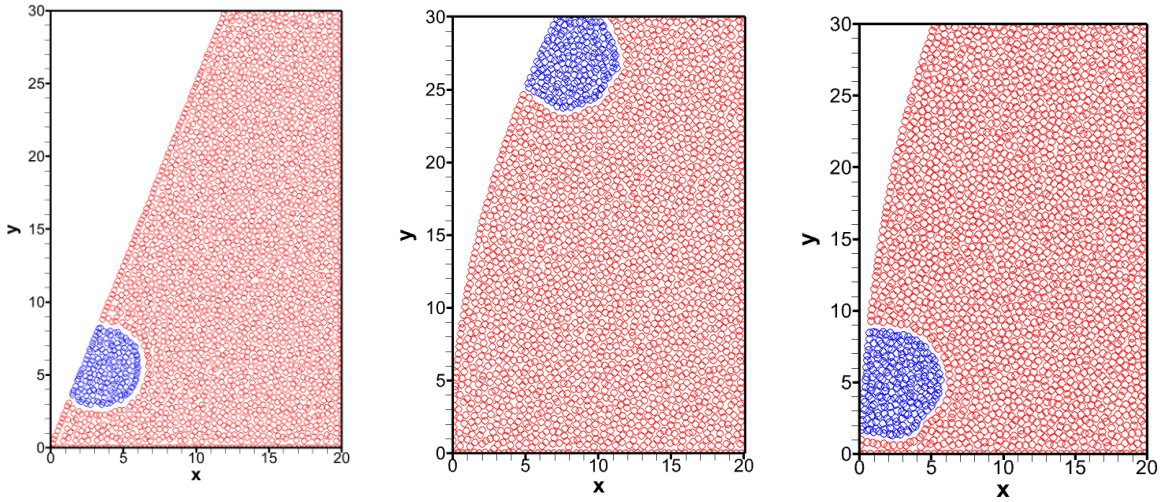

(a) (b) (c)

Fig. 3. Final liquid configurations for channels with (a) linear, (b) quadratic, and (c) exponential bottom-wall geometries.

The results demonstrate that wall geometry influences capillary-rise behavior. Although capillary forces drive the liquid upward in all cases, the final droplet position and interface configuration differ among the three geometries. These observations indicate that geometric confinement affects the evolution of the liquid interface and consequently modifies the capillary-driven motion. The influence of geometry becomes more evident when comparing the quadratic and exponential profiles. Both configurations introduce curvature into the channel. However, the spatial distribution of curvature differs considerably. In the exponential geometry, the wall curvature changes more rapidly near the inlet region, while the quadratic geometry provides a smoother geometric transition along the channel. As a result, the liquid experiences different confinement conditions during its upward motion, leading to distinct capillary-rise responses. These findings suggest that not only the presence of curvature, but also its distribution along the wall, plays a role in determining the rise dynamics.

To better understand the influence of wall curvature on the liquid motion, the temporal evolution of the droplet in the quadratic geometry was examined in greater detail. Fig. 4 shows a sequence of droplet configurations during the capillary-rise process. The droplet gradually migrates upward along the curved wall, confirming that the geometry

alone is sufficient to induce sustained capillary motion under otherwise identical physical conditions.

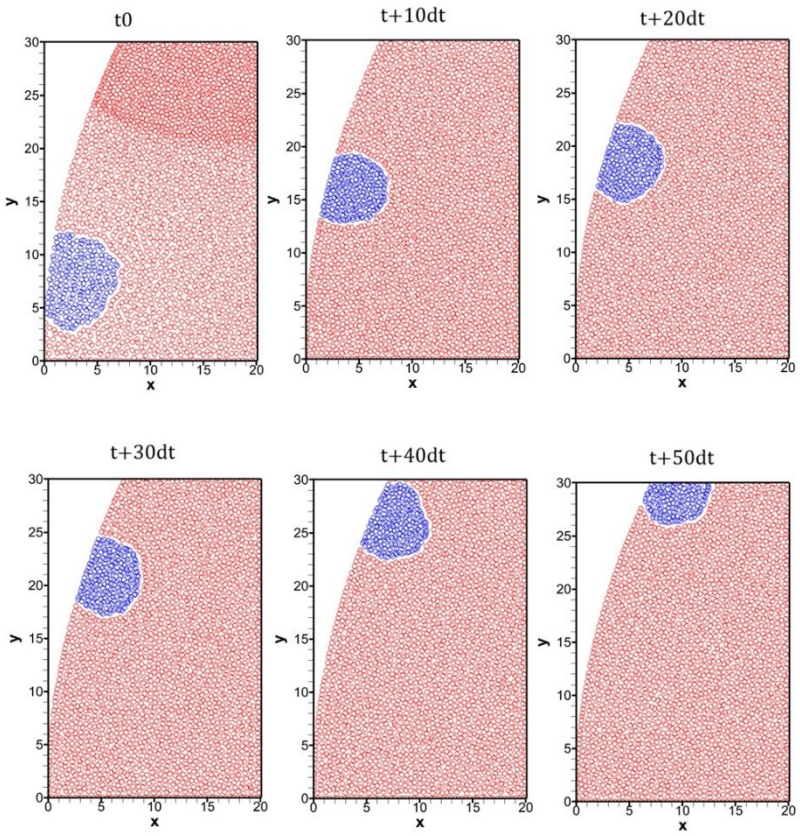

Fig. 4. Temporal evolution of the wetting droplet in the channel with a quadratic bottom-wall profile.

The droplet motion is not uniform throughout the simulation. During the initial stage, the droplet advances slowly from its starting position. As the rise proceeds, the upward motion becomes increasingly pronounced and the droplet covers a larger vertical distance over comparable time intervals. This behavior indicates that the capillary driving force varies during the ascent process rather than remaining constant.

To quantify this evolution, the center-of-mass (COM) velocity of the droplet was estimated and is presented in Fig. 5.

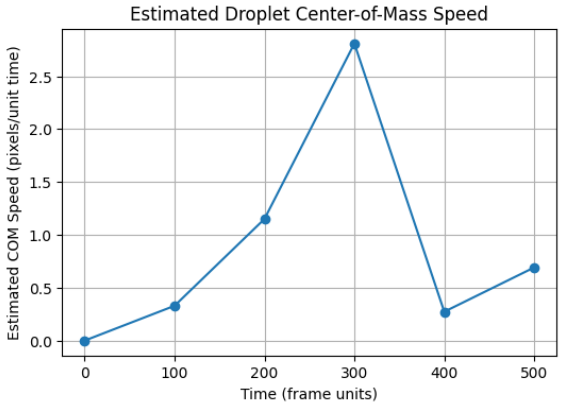

Fig. 5. Estimated center-of-mass velocity of the droplet in the quadratic geometry.

The velocity profile reveals three distinct stages. First, an acceleration stage is observed, during which the droplet velocity increases continuously from its initial value. The velocity reaches a maximum value of approximately 2.8 pixels per unit time at around (t = 300), indicating the most effective capillary transport regime within the channel. This increase suggests that the evolving droplet configuration and the local geometric constraints become increasingly favorable for upward motion as the droplet progresses along the wall. Following the peak velocity, a deceleration stage occurs. The droplet continues to move upward. However, its velocity decreases significantly compared with the maximum value. This reduction implies that the geometric conditions responsible for enhancing the capillary motion during the intermediate stage become less effective near the upper region of the channel. Consequently, the capillary-rise process in the quadratic geometry is characterized by a non-uniform velocity distribution rather than a constant ascent rate. Overall, the results demonstrate that wall curvature affects not only the final droplet position but also the temporal dynamics of capillary rise. Even in the absence of wettability gradients, external forcing, or changes in fluid properties, variations in channel geometry lead to measurable differences in liquid motion. From a biomimetic perspective, these findings support the idea that curved geometries, similar to those observed in natural liquid-transport systems, can regulate fluid motion through purely geometric effects. Therefore, wall curvature may be utilized as a passive design parameter for controlling capillary-driven transport in microfluidic and bio-inspired fluid-management devices.

4. Conclusion

This study investigated the influence of wall curvature on capillary-rise dynamics using Dissipative Particle Dynamics (DPD) simulations. By comparing linear, quadratic, and exponential channel geometries under identical fluid properties, wall–fluid interactions, and boundary conditions, the isolated effect of wall geometry on liquid motion was examined. The results demonstrated that wall curvature alters both the evolution of the liquid interface and the upward motion of the wetting phase. Distinct capillary-rise behaviors were observed among the investigated geometries, indicating that geometric confinement influences the capillary-pressure distribution and consequently affects liquid transport. The detailed analysis of the quadratic geometry further revealed that capillary rise proceeds through successive acceleration and deceleration stages rather than at a constant velocity. Overall, the findings confirm that wall curvature can serve as an effective passive parameter for controlling capillary-driven liquid transport. This work provides a fundamental understanding of curvature-dependent capillary-rise behavior and establishes the first step toward the development of biomimetic artificial xylem structures. Future studies will extend the present framework to investigate evaporation-assisted heat transfer and the design of artificial xylem cooling systems inspired by natural fluid-transport networks.

References:

[1] Gennes P-G, Brochard-Wyart F, Quéré D. Capillarity and wetting phenomena: drops, bubbles, pearls, waves. Springer; 2004.

[2] Stroock AD, Pagay V V, Zwieniecki MA, Michele Holbrook N. The physicochemical hydrodynamics of vascular plants. Annu Rev Fluid Mech 2014;46:615–42.

[3] Quéré D. Wetting and roughness. Annu Rev Mater Res 2008;38:71–99.

[4] Wheeler TD, Stroock AD. The transpiration of water at negative pressures in a synthetic tree. Nature 2008;455:208–12.

[5] Ju J, Bai H, Zheng Y, Zhao T, Fang R, Jiang L. A multi-structural and multi-functional integrated fog collection system in cactus. Nat Commun 2012;3:1247.

[6] Zheng Y, Bai H, Huang Z, Tian X, Nie F-Q, Zhao Y, et al. Directional water collection on wetted spider silk. Nature 2010;463:640–3.

[7] Lorenceau É, Quéré D. Drops on a conical wire. J Fluid Mech 2004;510:29–45.

[8] Luo J-L, Mo D-C, Wang Y-Q, Lyu S-S. Biomimetic copper forest wick enables high thermal conductivity ultrathin heat pipe. ACS Nano 2021;15:6614–21.

[9] Hu X, Hu C, Chen S, He Y, Li L, Tang D. Biomimetic porous wick with efficient fluid transport and excellent heat transfer for loop heat pipes. Appl Therm Eng 2024;249:123377.

[10] Ju J, Zheng Y, Jiang L. Bioinspired one-dimensional materials for directional liquid transport. Acc Chem Res 2014;47:2342–52.

[11] Shen J, Guo C. Biomimetic design for enhanced thermal performance of vapor chambers. Energies (Basel) 2025;18:1250.

[12] Fontenot RJ, Lockwood DJ, Allison JM, Preston DJ. A review and outlook on osmotically driven heat pipes for passive thermal transport. Appl Therm Eng 2024;248:123097.

[13] Caruana R, Guilizzoni M. Modeling of conventional heat pipes with capillary wicks: a review. Energies (Basel) 2025;18:2213.

[14] Tiwari A, Abraham J. Dissipative-particle-dynamics model for two-phase flows. Physical Review E—Statistical, Nonlinear, and Soft Matter Physics 2006;74:056701.

[15] Curk T. Dissipative particle dynamics for coarse-grained models. J Chem Phys 2024;160.

[16] Javan Nikkhah S, Vandichel M. Dissipative particle dynamics modeling in polymer science and engineering. Wiley Interdiscip Rev Comput Mol Sci 2025;15:e70018.

[17] Groot RD, Warren PB. Dissipative particle dynamics: Bridging the gap between atomistic and mesoscopic simulation. J Chem Phys 1997;107:4423–35.

[18] Goel H, Chandran PR, Mitra K, Majumdar S, Ray P. Estimation of interfacial tension for immiscible and partially miscible liquid systems by Dissipative Particle Dynamics. Chem Phys Lett 2014;600:62–7.

Fiber-Based Microfluidic Model for Pressure-Driven Wall Transport Studies

Sercan Altundemir[(1)], Azmat Ullah[(2)], Ilke Kaykanat[(1)], Kerem Pekkan[(2,3)], Kerem Uğuz[(1,*)]

(1) Department of Chemical Engineering, Boğaziçi University, Bebek, Istanbul 34342, Turkey

(2) Department of Biomedical Science and Engineering, Koç University, Sarıyer, Istanbul 34450, Turkey

(3) Department of Biomedical Engineering, The Ohio State University, Columbus, OH 43210, USA

1. Introduction

Cardiovascular diseases, such as atherosclerosis, are strongly associated with abnormal mechanical stimuli acting on the arterial wall. While previous studies have extensively focused on intraluminal blood flow, less attention has been given to the transmural flow. Despite its importance, the relationship between arterial mechanics and transmural flow remains insufficiently understood due to the lack of integrated experimental and computational methodologies. However, earlier studies by Tarbell and co-workers showed that interstitial flow through the arterial wall can generate shear stress on vascular smooth muscle cells and may therefore influence vascular wall remodeling [1,2]. More recently, Altundemir et al. (2024) [3] developed a computational transmural flow model demonstrating that arterial geometry, wall mechanics, and permeability can strongly affect interstitial flow and the resulting mechanical environment within the vessel wall. To address this gap, experimental studies are needed; however, before performing complex ex vivo vessel experiments and simulations, it is necessary to establish a reliable experimental setup. Therefore, this work focuses on fiber-based confocal experiments together with FEBio-based numerical simulations. Similar fiber-level microfluidic approaches have recently been used to quantify mass transport efficiency around hollow fibers, highlighting the value of simplified fiber-based platforms for resolving local transport mechanisms before moving to more complex biological systems [4]. These experiments provide a simpler and more controllable environment for studying pressure-driven transport behavior. Here, fiber serves as a simplified model to investigate passive diffusion and permeation under controlled conditions. Although biological barriers involve additional mechanisms such as active transport, tissue remodeling, and cellular interactions, permeability

measurements in artificial systems provide an important intermediate step for understanding transmural transport behavior and guiding the development of more realistic experimental and computational vascular models.

2. Materials and Methods

2.1 Experiments

For the experiments, first, a microchip was designed in SolidWorks to hold the fiber tubes. After printing, the chip was cleaned, UV-cured, and prepared for the experiment. The fiber is placed inside the chip, and the system is sealed to allow confocal imaging. For the experiments, PBS and Rhodamine B solution are pumped into the chip using an Elveflow pressure controller. The esxperimental set-up is shown in Fig. 1. First, PBS is used to fill the system and wet the fiber. After removing air bubbles, Rhodamine B solution is sent through the system under controlled pressure. Confocal microscopy is used to image the time-dependent transport of tracer through the fiber wall. The obtained fluorescence images are then used to evaluate dye movement through the porous fiber structure.

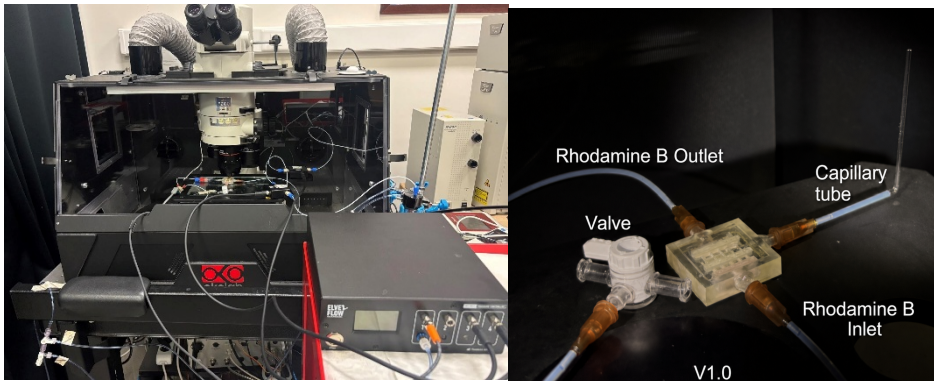

Figure 1. (a) Experimental set-up and (b) microchip and fiber tubes

2.2 Numerical Part

For the numerical analysis, a one-dimensional time-dependent model is developed to describe solute transport through a porous medium. In FEBio, a multiphasic model is used to solve Rhodamine B transport across the fiber wall under the prescribed conditions. The porosity and permeability of the porous medium are assumed to remain constant over time. Within this study, the binding mechanism of Rhodamine B molecules

3. Results and Discussion

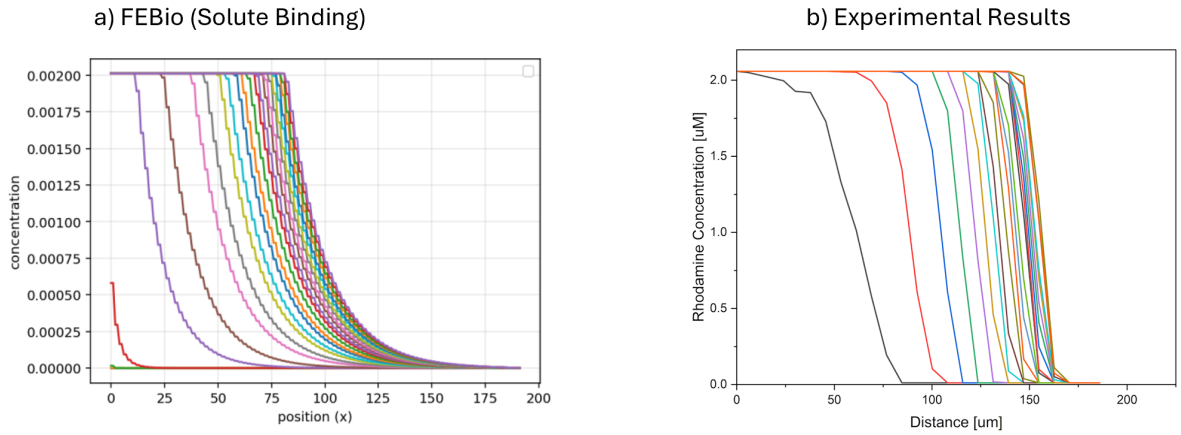

Figure 2. Comparison of numerical and experimental results for Rhodamine transport and adsorption. (a) adsorbed solute concentration obtained using the FEBio model and (b) experimentally measured Rhodamine concentration profiles at different times.

Figure 2(a) shows the concentration profiles obtained from the FEBio simulations. Figure 2(a) presents the adsorbed solute concentration at different time points. The results show that the solute moves through the medium over time, while a portion of it is retained due to the binding mechanism. The rapid decrease in concentration over a short distance indicates that adsorption significantly affects the transport process. Figure 2(b) presents the experimental Rhodamine B concentration profiles along the fiber wall under 100 mbar pressure. The curves correspond to confocal measurements taken at 2-minute intervals. Rhodamine B initially remains near the outer surface and gradually penetrates into the fiber wall. However, the concentration stays low near the inner side, indicating limited permeability and slow transport.

4. Conclusion

The fiber experiments are an important preliminary step for studying pressure-driven transmural transport before moving to ex vivo vessel experiments. Because the fiber has a porous cylindrical structure, it provides a controlled and reproducible model to examine transport across a wall-like geometry. The results show that Rhodamine transport is governed by diffusion, pressure-driven flow, and adsorption within the porous matrix. This indicates that transmural transport cannot be described only by pressure-driven flow and permeability;

solute–matrix interactions must also be considered. Therefore, these experiments help identify the key physical mechanisms that should be included in the computational model.

Acknowledgment: We acknowledge TÜBİTAK Project no: 124M473.

References:

[1] Tada, S., & Tarbell, J. M. (2000). Interstitial flow through the internal elastic lamina affects shear stress on arterial smooth muscle cells. American Journal of Physiology-Heart and Circulatory Physiology, 278(5), H1589–H1597.

[2] Tada, S., & Tarbell, J. M. (2002). Flow through internal elastic lamina affects shear stress on smooth muscle cells (3D simulations). American Journal of Physiology-Heart and Circulatory Physiology, 282(2), H576–H584.

[3] Altundemir, S., Lashkarinia, S. S., Pekkan, K., & Uğuz, A. K. (2024). Interstitial flow, pressure and residual stress in the aging carotid artery model in FEBio. Biomechanics & Modeling in Mechanobiology, 23(1), 179.

[4] Ullah, A., Gölcez, T., Teber, O. O., Koyuncu, İ., Kerem Uğuz, A., & Pekkan, K. (2025). A microfluidic technique for measuring fiber-level mass transport efficiency and hemolysis of blood oxygenators. Biomicrofluidics, 19(6).

Improved edge detection method in deformable microfluidic chips

İsmail Bütün[1,2], Zülal Muganlı[1,2], Ramazan Ceylan[1,2], Ali Koşar[1,2,3,4,*]

[1] Faculty of Engineering and Natural Sciences, Sabancı İstanbul, Türkiye

[2] Sabancı University Nanotechnology Research and Application Centre (SUNUM), İstanbul, Türkiye

[3] Center of Excellence for Functional Surfaces and Interfaces for Nano-Diagnostics (EFSUN), Sabancı University, İstanbul, Türkiye

[4] Turkish Academy of Sciences (TÜBA), Çankaya, 06700, Ankara, Türkiye

[*] Corresponding Authors: Ali Koşar; Email: kosara@sabanciuniv.edu

Abstract: Elastomeric microfluidic chips deform under pressure-driven flow, and the resulting change in channel geometry alters the hydrodynamic resistance and the local flow field. Deformation is normally measured by flowing a fluorescent tracer through the channel, but Rhodamine B (Rh-B) partitions into and diffuses through polydimethylsiloxane (PDMS), so the signal spreads beyond the true wall and blurs the very interface the measurement depends on. Here we invert the labelling scheme. Rh-B is dispersed in the PDMS prepolymer before casting, so the wall itself emits and the lumen stays dark. Confocal imaging of dye-doped chips gave sharp, threshold-insensitive boundaries in top, side and cross-sectional views, whereas tracer-filled and tracer-aged controls showed progressive edge broadening; the extracted channel height rose from ≈ 101 µm at rest to ≈ 126 µm at 2000 µL.min^{-1}. Tensile testing showed a concentration-dependent increase in elongation at break, so the dye loading can be selected without compromising the mechanical integrity of the device. The method requires no additional instrumentation and offers a low-cost route to deformation metrology in compliant microfluidic devices.

Keywords: deformable microchannels; soft lithography; PDMS; fluorescent imaging; confocal microscopy; edge detection

[1] Introduction

PDMS dominates the prototyping of various types of microfluidic chips and microphysiological systems, but its low elastic modulus means that channels deflect measurably under pressure-driven flow [1], [2], [3]. When the cross-section changes, the flow changes with it. The hydrodynamic resistance no longer scales linearly with flow rate, the wall shear stress felt by cultured cells differs from the design value, and particle focusing positions shift [4], [5], [6]. Deformation is therefore something that must be designed for, not a minor artefact.

The standard measurement is confocal microscopy of a channel filled with Rh-B solution, in which the lumen is bright and the wall is inferred from where the signal ends [1], [2], [3], [4]. This assumes the dye stays in the liquid. It does not: Rh-B absorbs into PDMS and diffuses into the bulk, so the emitting region grows during an experiment, and the apparent wall migrates outward, leaving an edge that is soft, threshold-dependent and biased. Digital image correlation, interferometry and model-based inversion of pressure–flow data avoid the tracer but demand specialized hardware or extra assumptions [5], [6]. We therefore incorporated the Rhodamine B dye into the PDMS matrix rather than into the liquid flowing through the channel.

[2] Materials and Methods

Chips were imaged in three ways. In the conventional case, a pristine chip was imaged while a 0.5 mM Rh-B solution flowed through it. In the second, a chip was filled with the same solution, stored for 24 h, then flushed and run with water. In the third, the dye was already embedded in the PDMS, and the chip was run with water only. Water was driven through each device at 0, 500, 1000 and 2000 $\mu L.min^{-1}$. Confocal z-stacks were reconstructed into top, side and cross-sectional views. Wall position was taken from the intensity gradient of line profiles normal to the interface, and channel height from the separation of the two edges.

[3] Results and Discussion

The three imaging schemes differ in the quantity that matters least in a qualitative image and most in a measurement, which is the sharpness of the wall. When the dye flows through the channel, the lumen is bright, but the intensity profile decays over several micrometers into the PDMS, and the decay length grows with imaging time, so the extracted edge depends on both acquisition time and threshold. A chip that had been in contact with the dye solution and then

flushed remained fluorescent at the wall while carrying only water, which confirms that the blur originates from absorbed rather than free dye. Embedding the dye in the polymer reverses the contrast. Emission comes from the solid, the lumen is dark, and the interface becomes a step in material rather than a diffusing concentration field, so the extracted edge positions were threshold-insensitive and stable in time.

Reconstructed views resolved the expected deformation signature over 0–2000 $\mu L.min^{-1}$. The roof deflects outward and the cross-section evolves from rectangular towards a crowned profile. The extracted channel height increased monotonically and non-linearly with flow rate, from ≈ 101 µm at rest to ≈ 126 µm at 2000 $\mu L.min^{-1}$, in agreement with shallow-channel theory [1], [4], [5]. A 25% change of this kind would propagate as a large error in any resistance or shear-stress estimate based on the nominal geometry.

Doping did not compromise the mechanical integrity of the devices. Elongation at break increased logarithmically with dye concentration and the plasma bonding was unaffected, so the dye loading can be chosen freely provided it is held constant within a study and reported with the deformation data.

Conclusion

Moving the fluorophore from the working fluid into the channel wall removes the dominant error source in confocal deformation metrology on PDMS devices. Dye-doped chips yield sharp, time-stable, threshold-insensitive edges in all three views, enabling accurate quantification of pressure-induced deformation with standard imaging equipment while preserving the properties of PDMS.

Acknowledgement:
The authors acknowledge the support of Sabancı University, SUNUM and EFSUN. This research was funded by the TÜBİTAK 1004 NANOSIS Programme, Grant Number 20A6012.

References:

[1] T. Gervais, J. El-Ali, A. Günther, and K. F. Jensen, “Flow-induced deformation of shallow microfluidic channels,” Lab Chip, vol. 6, no. 4, pp. 500–507, 2006, doi: 10.1039/B513524A.

[2] J. M. de Rutte, K. G. Janssen, N. R. Tas, J. C. Eijkel, and S. Pennathur, "Numerical investigation of micro- and nanochannel deformation due to discontinuous electroosmotic flow," Microfluidics and Nanofluidics, vol. 20, no. 11, p. 150, 2016.

[3] B. S. Hardy, K. Uechi, J. Zhen, and H. Pirouz Kavehpour, "The deformation of flexible PDMS microchannels under a pressure driven flow," Lab Chip, vol. 9, no. 7, pp. 935–938, 2009, doi: 10.1039/B813061B.

[4] H. Jeon, T. Kwon, J. Yoon, and J. Han, "Engineering a deformation-free plastic spiral inertial microfluidic system for CHO cell clarification in biomanufacturing," Lab Chip, vol. 22, no. 2, pp. 272–285, 2022, doi: 10.1039/D1LC00995H.

[5] A. Martínez-Calvo, A. Sevilla, G. G. Peng, and H. A. Stone, "Start-up flow in shallow deformable microchannels," Journal of Fluid Mechanics, vol. 885, p. A25, 2020.

[6] M. K. Raj, S. DasGupta, and S. Chakraborty, "Hydrodynamics in deformable microchannels," Microfluidics and Nanofluidics, vol. 21, no. 4, p. 70, 2017, doi: 10.1007/s10404-017-1908-5.

Reversible Thermoplastic Integration Workflow for Packaging MEMS Devices and Commercial Electrodes into Microfluidic Cartridges

Mehmet Oğulcan Güngör[1,2,*], Seçkin Eroğlu[1,3], Ender Yıldırım[1,3]

[1]ODTU MEMS Center, Ankara, Türkiye

[2]Micro and Nanotechnology, Middle East Technical University, Ankara, Türkiye

[3]Department of Mechanical Engineering, Middle East Technical University, Ankara, Türkiye

Integrating MEMS devices and commercial electrodes into cartridges remains a key bottleneck for translatable lab-on-a-chip platforms. Conventional PDMS or adhesive bonding methods are irreversible, non-scalable, and compromise electrochemical sensor accuracy due to small molecule absorption [1]. This work introduces a rapid tooling, fully thermoplastic workflow for adhesive-free, reversible, and scalable heterogeneous integration. The platform utilizes a four-layer architecture comprising a PMMA top cover, a thermoformed Flexdym channel layer, the inserted substrate, and a PMMA support base. Thermoforming molds were SLA 3D printed using High Temp resin, while PMMA layers were produced by CNC milling for prototyping, though they are equally compatible with hot embossing or injection molding for scalable production. This rapid tooling route enabled a design-to-device cycle time under one working day for the prototype, while the all-thermoplastic material set keeps the workflow inherently compatible with scalable replication methods. During assembly, components nest within PMMA cavities to prevent shifting, and reversible sealing is achieved via 3D printed clamps or embedded magnets. Flexdym achieves conformal sealing and exhibits approximately 66% lower small molecule absorption than PDMS [2], protecting sensor accuracy from dose masking effects. The magnet-assembled variant features all-thermoplastic structural components, allowing full recycling under the EU Circular Economy Action Plan. Molds withstood more than 50 thermoforming cycles without measurable geometric degradation. The workflow was validated across two device categories: first, an electrochemical flow cell housing a screen-printed electrode with a clamp assembled variant and a magnet assembled variant, the latter featuring a 30x30 mm footprint and port positions compliant with ISO 22916 [3]. Second, a compact 45x34x6 mm cartridge for pleural effusion screening, integrating a bimodal MEMS sensor on glass substrate beneath a microfluidic channel layer. Burst pressure was characterized using a pressure controller with the cartridge outlet sealed, gradually increasing the applied pressure until failure. Both assemblies remained leak-proof under flow, withstanding burst pressures up to 270 kPa and 380 kPa for the magnet and clamp variants respectively, with no degradation across repeated disassembly and reassembly cycles. The workflow addresses reversibility, scalability, and material sustainability in a single platform, offering a generalizable route from rapid prototyping to scalable biosensor cartridges.

Acknowledgement: This work was supported by TÜBİTAK under grant number 22AG008 (MAESTRO) and by the European Union Horizon Europe Programme under grant agreement No. 101079473 (OrChESTRA).

References:

[1] Rodrigues, R. G., Condelipes, P. G. M., Rosa, R. R., Chu, V., & Conde, J. P. (2023). Scalable processing of cyclic olefin copolymer (COC) microfluidic biochips. Micromachines, 14(10), 1837.

[2] Salmon, H., Rasouli, M. R., Distasio, N., & Tabrizian, M. (2021). Facile engineering and interfacing of styrenic block copolymers devices for low-cost, multipurpose microfluidic applications. Engineering Reports, 3(7), e12361.

[3] International Organization for Standardization. (2022). Microfluidic devices — Interoperability requirements for dimensions, connections and initial device classification (ISO Standard No. 22916:2022).

Microfabricated Pyrolytic Carbon Electrodes: A Proof-of-Concept Study from Fabrication to Electrochemical Performance Evaluation

Amir Fadaie[1*], Murat Artuç[1], Vildan Sanko[1], Aykan Batu[1], Ender Yıldırım[1,2,3]

[1] METU MEMS Center, Ankara, Türkiye

[2] Department of Mechanical Engineering, Middle East Technical University, Ankara, Türkiye

[3] Micro and Nanotechnology Program, Middle East Technical University, Ankara, Türkiye

[1] Introduction

Carbon-based electrodes have been widely used in electrochemical systems owing to their advantageous characteristics, such as an extended electrochemical potential range, strong chemical inertness, low manufacturing cost, and effective catalytic behavior toward numerous redox processes [1], [2]. Therefore, different carbon structures, including highly oriented pyrolytic graphite, graphene, carbon nanotubes, and carbon thin films, have been studied for a variety of electrochemical purposes such as analytical sensing [3], [4] and electrocatalytic applications [5], [6].

This work presents the fabrication and characterization of a MEMS-compatible carbon electrode. After standard microfabrication steps, the structure was thermally converted into a conductive carbon material under an inert argon (Ar) atmosphere at elevated temperature. A significant shrinkage in film thickness was observed, decreasing from roughly 15 µm to about 1.15 µm after pyrolysis, which is attributed to the elimination of volatile species and densification of the carbon network.

[2] Materials and Methods

Microfabrication processes were employed to fabricate polymer structures, followed by pyrolysis under an argon atmosphere to obtain conductive carbon electrodes. Electrical properties were characterized using the Van der Pauw method. Surface morphology and composition were investigated by SEM, EDX, and Raman spectroscopy. Electrochemical performance was evaluated by cyclic voltammetry using the ferri/ferrocyanide redox couple.

[3] Results and Discussion

The results revealed that the produced pyrolytic carbon electrode exhibited a low sheet resistance, with a resistivity of approximately 0.013 Ω·cm. Correspondingly, the electrical conductivity was determined to be approximately 76 S/cm. The obtained low resistivity and high conductivity values indicate that the carbon structure formed after pyrolysis possesses efficient charge transport properties and provides a conductive network suitable for electrochemical applications. In addition, the low standard deviation values obtained from the Van der Pauw measurements demonstrated high measurement repeatability and good electrical homogeneity of the carbon film. Furthermore, 5th BioMEMS and Microfluidic Technologies Workshop 11 - 12 June 2026 compared with commercial screen-printed carbon electrodes, the MEMS-based pyrolytic carbon electrode exhibited improved electrochemical redox performance. This improved electrical performance is attributed to the dense binder-free carbon

network structure, the more compact carbonization mechanism, and the enhanced electron transport properties enabled by the microscale fabrication processes. Morphological and compositional analyses performed by SEM and EDX indicated a carbon dominated structure with a carbon content of about 95%. Raman spectroscopy confirmed the presence of both D and G bands, while an increased ID/IG ratio suggested a higher degree of structural disorder, which is typically associated with an increased density of electrochemically active sites. Electrochemical behavior was assessed using cyclic voltammetry in a ferri/ferrocyanide ($[Fe(CN)6]^{3-/4-}$) redox electrolyte. The MEMS-based electrode exhibited higher peak currents than the commercial counterpart, indicating a larger electroactive surface area and improved charge-transfer kinetics.

Conclusion

This study demonstrates that MEMS-fabricated carbon electrodes produced via pyrolysis can provide a good alternative to conventional screen-printed carbon electrodes for electrochemical sensing applications.

Acknowledgement:

The authors gratefully acknowledge Prof. Dr. Uğur Tamer from Gazi University for providing access to the Raman spectroscopy facility, and Dr. Ayşen Gümüştaş from the METU MEMS Center for performing the Raman spectroscopy measurements. The authors also thank Mr. Servet Şehirli from the Department of Mechanical Engineering at Middle East Technical University for his assistance with furnace usage during the fabrication process.

This work was supported by the Scientific and Technological Research Council of Türkiye (TÜBİTAK) under Grant No. 22AG008.

References:

[1] Kangmennaa, A., Forkuo, R. B., & Agorku, E. S. (2024). Carbon-based electrode materials for sensor application: a review. Sensing Technology, 2,1.

[2] Skinner, W.S.; Ong, K.G. (2020). Modern Electrode Technologies for Ion and Molecule Sensing. Sensors, 20, 4568.

[3] A. Casanova, J. Iniesta, A. Gomis-Berenguer (2022) Recent progress in the development of porous carbon-based electrodes for sensing applications. Analyst, 147, 767-789.

[4] D.A.C. Brownson, C.W. Foster, C.E. Banks. (2012). The electrochemical performance of graphene modified electrodes: an analytical perspective. Analyst, 137, 1815-1823.

[5] Y. Zheng, Y. Jiao, Y. Zhu, L.H. Li, Y. Han, Y. Chen, A. Du, M. Jaroniec, S.Z. Qiao (2014) Hydrogen evolution by a metal-free electrocatalyst. Nature Communications, 5, 1-8.

[6] J. Liang, Y. Zheng, J. Chen, J. Liu, D. Hulicova-Jurcakova, M. Jaroniec, S.Z. Qiao (2012) Facile oxygen reduction on a three-dimensionally ordered macroporous graphitic C 3N 4/carbon composite electrocatalyst. Angewandte Chemie International Edition, 51, 3892-3896.

Optimization of Functional Maturation of hiPSC-Derived Hepatic Organoids in a Dynamic Microfluidic Liver-on-a-Chip Platform Using Box-Behnken Experimental Design

Pelin Saglam-Metiner[1,2,3*], Cemile Nur Agaca[1,4], Omur Sert[2], Ozlem Yesil-Celiktas[2,3,5], Esra Erdal[1,4,6]

[1]Izmir Biomedicine and Genome Center, Izmir, Türkiye,

[2]Department of Bioengineering, Faculty of Engineering, Ege University, Izmir, Türkiye

[3]Ege University Translational Pulmonary Research Center (EgeSAM), Izmir, Türkiye

[4]Dokuz Eylul University, Izmir International Biomedicine and Genome Institute, Izmir, Türkiye

[5]ODTU-MEMS, Ankara, Türkiye

[6]Dokuz Eylul University, Faculty of Medicine, Department of Medical Biology, Izmir, Türkiye

Introduction. Human induced pluripotent stem cell (hiPSC)-derived hepatic organoids are promising human-relevant in vitro models for disease modeling, drug screening, and toxicological studies [1]. However, current hepatic organoid systems still exhibit fetal-like immaturity, limited functional stability, and inter-culture variability [2].

Materials and Methods. In this study, we developed a dynamic microfluidic liver organoid-on-a-chip platform designed to mimic physiologically relevant laminar flow and low shear stress conditions to enhance hepatic organoid maturation. hiPSC-derived hepatic organoids were cultured in a custom-designed perfusable microfluidic chip system and optimized using a Box-Behnken response surface methodology. Albumin secretion was selected as the primary functional response, while organoid passage number, perfusion flow rate, and maturation duration were evaluated as independent variables. Experimental optimization was performed using Design-Expert software, generating a 15-run experimental design to identify conditions maximizing hepatic functionality.

Results and Discussion. Following optimization, organoids cultured under dynamic on-chip conditions were characterized using functional, molecular, and histological analyses, including albumin secretion, ATP-based viability assays, CYP3A4 activity, glycogen accumulation, immunofluorescence staining, and qRT-PCR profiling of hepatic and biliary markers. Dynamic microfluidic culture conditions enhanced hepatic and biliary phenotypic signatures while supporting a more heterogeneous and physiologically relevant cellular composition compared to static culture systems.

Conclusion. Overall, this study demonstrates that integration of statistical experimental design with organ-on-chip technology enables robust optimization of hepatic organoid maturation and functionality, providing a scalable and translationally relevant liver-on-chip platform for biomedical applications.

Acknowledgement: This study was financially supported by the Scientific and Technological Research Council of Turkey (TUBITAK) - Science Fellowships and Grant Programmes (BIDEB) 2218 through number of 123C325 and, TUBITAK 1001 project through number of 124R024.

References:

[1] Akbari, S., Sevinç, G. G., Ersoy, N., Basak, O., Kaplan, K., Sevinç, K., ... & Erdal, E. (2019). Robust, long-term culture of endoderm-derived hepatic organoids for disease modeling. Stem cell reports, 13(4), 627-641.

[2] Reza, H. A., Santangelo, C., Iwasawa, K., Reza, A. A., Sekiya, S., Glaser, K., ... & Takebe, T. (2025). Multi-zonal liver organoids from human pluripotent stem cells. Nature, 641(8065), 1258-1267.

MEMS-Based Electrochemical Biosensor Platforms for ctDNA Detection: From Static to Microfluidic Architectures

Zeynep Çağlayan Arslan[1,2,*], Meltem Okan[1,3], Haluk Külah[1,2,3]

[1] METU MEMS Center, Ankara, Turkey

[2] Department of Electrical and Electronics Engineering, METU, Ankara, Turkey

[3] Department of Micro and Nanotechnology, METU, Ankara, Turkey

Circulating tumor DNA (ctDNA) has emerged as a promising liquid biopsy biomarker for non-invasive cancer diagnostics and molecular monitoring [1]. However, conventional nucleic acid detection workflows often require labor-intensive processing, amplification, or labeling steps that limit rapid and decentralized implementation. In this context, electrochemical biosensors offer significant advantages due to their low-cost instrumentation, label-free detection capability, miniaturization potential, and compatibility with microfluidic integration [2].

This work presents the development of MEMS-based electrochemical biosensor platforms for ctDNA detection, following a progressive platform engineering approach from static planar sensing architectures to integrated microfluidic implementations. The presented platform was demonstrated for hepatocellular carcinoma (HCC)-associated ctDNA detection, a clinically relevant use case for minimally invasive molecular monitoring [3].

The initial development stage focused on a planar MEMS-based electrochemical biosensor operating under static conditions. The platform employed a three-electrode configuration consisting of gold (Au) working, platinum (Pt) counter, and silver (Ag) reference electrodes fabricated on glass substrates using standard MEMS microfabrication techniques. This static platform served as a controlled testbed for baseline electrochemical characterization, optimization of assay parameters, and proof-of-concept validation of hybridization-based DNA sensing using electrochemical impedance spectroscopy (EIS).

Based on the optimized sensing workflow established under static conditions, a dedicated microfluidic MEMS biosensor platform was subsequently developed for controlled fluidic

operation [4]. The final platform preserved the same three-electrode electrochemical sensing configuration while employing a specifically designed MEMS sensing chip integrated with a PDMS microchannel, enabling controlled fluid handling in a more application-relevant format. Thiolated single-stranded DNA probes immobilized on the Au working electrode enabled label-free hybridization-based target recognition without amplification or fluorescent labeling.

The integrated microfluidic biosensor demonstrated sensitive ctDNA detection with a limit of detection of 1.43 fM over a 2–200 fM dynamic range. Specificity was validated using one-base mismatched and fully non-complementary control sequences, confirming reliable target discrimination. The progression from static assay development to microfluidic integration highlights a practical MEMS-based biosensor translation strategy for liquid biopsy applications.

Overall, this work demonstrates a MEMS-based electrochemical biosensor development pathway for ctDNA detection, progressing from foundational static assay development to integrated microfluidic implementation. Beyond the presented HCC use case, the proposed platform architecture offers broader potential for nucleic acid biomarker detection in future point-of-care diagnostic applications.

Acknowledgements:

This work was financially supported by the Scientific and Technological Research Council of Turkey (TÜBİTAK) under Grant No. 119E628.

References:

[1] Wan, J. C. M., Massie, C., Garcia-Corbacho, J., Mouliere, F., Brenton, J. D., Caldas, C., Pacey, S., Baird, R., & Rosenfeld, N. (2017). Liquid biopsies come of age: towards implementation of circulating tumour DNA. *Nature Reviews Cancer*, 17(4), 223–238.

[2] Campuzano, S., Serafín, V., Gamella, M., Pedrero, M., Yáñez-Sedeño, P., & Pingarrón, J. M. (2019). Opportunities, challenges, and prospects in electrochemical biosensing of circulating tumor DNA and its specific features. *Sensors*, 19(17), 3762.

[3] Yang, J.-C., Hu, J.-J., Li, Y.-X., Luo, W., Liu, J.-Z., & Ye, D.-W. (2022). Clinical applications of liquid biopsy in hepatocellular carcinoma. *Frontiers in Oncology*, 12, 781820.

[4] Çağlayan Arslan, Z., Okan, M., & Külah, H. (2024). Pre-enrichment-free detection of hepatocellular carcinoma-specific ctDNA via PDMS and MEMS-based microfluidic sensor. *Microchimica Acta*, 191, 229.

Acousto-Holographic Lab-on-Chip Platform for Single-Cell Mechanophenotyping Across the Oral Dysplasia–Carcinoma Continuum

Ayşenur Akgün[1], Merve Sevgi[2], Yağmur Işık[3], Hasan Berkay Abdioğlu[3], Esmahan Çağlar[2], Merva Soluk Tekkeşin[4], Yasemin Başbınar[5], Daniela Elena Costea[6], Hüseyin Üvet[3,*]

[1] Yildiz Technical University, Department of Molecular Biology and Genetics, Istanbul, Türkiye
[2] Yildiz Technical University, Department of Bioengineering, Istanbul, Türkiye
[3] Yildiz Technical University, Department of Mechanical Engineering, Istanbul, Türkiye
[4] Ankara University, Faculty of Dentistry, Department of Clinical Sciences, Ankara, Türkiye
[5] Dokuz Eylül University, Oncology Institute, Izmir, Türkiye
[6] University of Bergen, Department of Clinical Medicine, Bergen, Norway

* Corresponding author: Hüseyin Üvet – huvet@yildiz.edu.tr

Introduction. Histopathological grading of oral squamous cell carcinoma (OSCC) carries interobserver variability and incompletely resolves the biological heterogeneity of the dysplasia-to-carcinoma transition, particularly at the borderline between high-grade dysplasia and early invasive carcinoma [1]. Single-cell mechanical phenotype is an integrative, observer-independent readout of cytoskeletal state, prestress and adhesion, each of which is remodelled during epithelial–mesenchymal transition (EMT) and malignant progression [2,3]. Conventional atomic force microscopy (AFM) is, however, slow (typically <8 measurement points·s^{-1}), is biased by tip–sample contact mechanics, and damages cells on repeated probing [4]. We previously developed and AFM-validated an acousto-holographic lab-on-chip platform that reconstructs whole-cell stiffness label-free and contact-free in ~10 s per cell, and demonstrated its biological sensitivity to TGF-β-induced EMT in colorectal carcinoma [5]. Here we extend this BioMEMS platform to the oral dysplasia–OSCC continuum and test whether the resulting single-cell mechanical fingerprint tracks malignant grade or epithelial differentiation / EMT status.

Materials and Methods. A PDMS–PZT microfluidic chip (a 12 × 12 mm PDMS chamber bonded to a bulk-acoustic-wave transducer following O_2-plasma activation, mounted on a 0.13–0.17 mm cover-glass substrate) was integrated with an in-line Mach–Zehnder interferometer (527 nm, 10 mW) [5]. The PZT was driven at its 1 kHz resonant frequency (24 V_{pp}; 0.05 W; sub-micron nominal membrane displacement) and 1000 phase-shifted interferograms (50 frames × 20 π/10-rad phase steps) per cell were acquired in ~1 s on a CMOS detector synchronised to a piezo phase-stepper. Phase maps were reconstructed via wavelet-based carrier demodulation with BM3D denoising and preconditioned-conjugate-gradient unwrapping; pixel-wise strain $\varepsilon(x,y) = [h_0(x,y) - h(x,y)] / h_0(x,y)$ was Hertzian-fitted to whole-cell stiffness (Pa), calibrated against AFM via polyacrylamide and agarose microbeads (R^2 = 0.90-0.93) and HCT116 cells (1.08 ± 0.14 kPa acousto-holography vs 1.16 ± 0.22 kPa AFM) [5]. Five oral cell lines — POE9n-TERT (mild/moderate dysplasia), DOK (severe dysplasia), CaLH3 (well-differentiated OSCC), Ca1 (OSCC) and Luc4 (poorly-differentiated, EMT-enriched OSCC) were profiled (3–4 biological replicates each; ≥15 cells per replicate; n = 417 single cells). Cell-level Kruskal-Wallis followed by pairwise Mann-Whitney U with Benjamini–Hochberg FDR correction was complemented by a linear mixed-effects model with biological replicate as a random intercept.

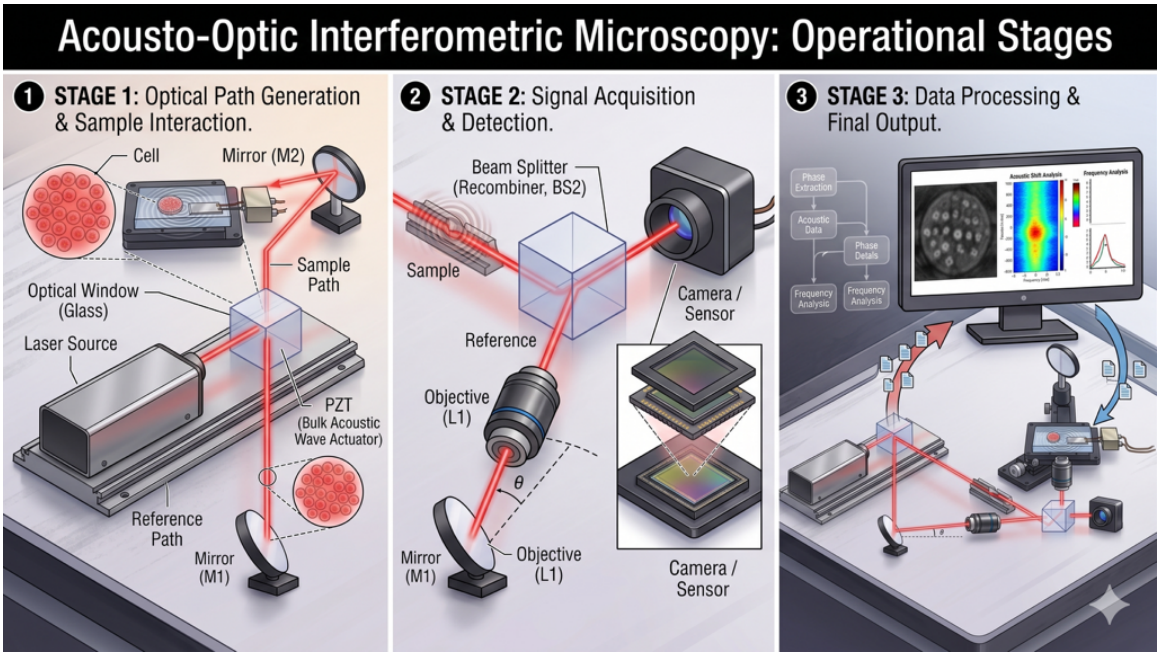

Figure 1: Acousto-Optic Interferometric Microscopy: Operational Stages

Results and Discussion. Median whole-cell stiffness ranged from 425 Pa (Luc4) to 711 Pa (CaLH3) - a 1.67-fold range across the panel (Kruskal–Wallis H = 15.63, p = 3.6 × 10^{-3}). The well-differentiated OSCC line CaLH3 was significantly stiffer than the EMT-enriched poorly-differentiated OSCC line Luc4 (Mann-Whitney U, FDR-adjusted p = 5.3 × 10^{-3}; Cliff's δ = +0.31 [95% CI +0.17, +0.45]; 92% achieved power); the severe-dysplasia line DOK was likewise stiffer than Luc4 (FDR-adjusted p = 2.3 × 10^{-2}; Cliff's δ = +0.26). Empirical cumulative distributions showed an enriched <300 Pa lower tail in Luc4, consistent with its known $CD44^{hi}EpCAM^{lo}$ post-EMT subpopulation [6]. Critically, stiffness rankings did not track malignant grade monotonically: dysplastic and well-differentiated OSCC lines occupied overlapping mechanical regimes, whereas the EMT-enriched line was consistently the softest. These findings parallel the Twist1/Snail/Rac1-driven cytoskeletal softening previously reported in head-and-neck squamous cell carcinoma [3] and reinforce EMT, rather than malignant grade per se, as the dominant determinant of single-cell mechanics across the oral neoplastic continuum.

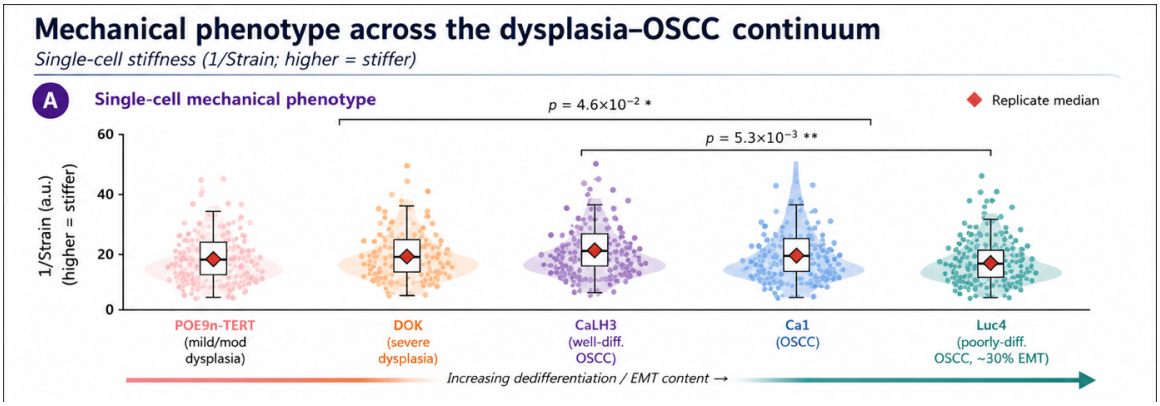

Figure 2: Single-cell mechanical phenotype across the oral dysplasia–OSCC continuum.

Conclusion. Acousto-holographic mechanophenotyping on a PDMS-PZT lab-on-chip platform discriminates EMT-enriched poorly-differentiated OSCC from well-differentiated and dysplastic counterparts, supporting BioMEMS-enabled single-cell mechanobiology as a candidate label-free, non-contact adjunct to conventional histopathological grading of OSCC.

Acknowledgement: This work builds on a platform originally developed under TÜBİTAK project 116E743 (acknowledged in [5]). Funding for the present extension to the oral dysplasia–OSCC continuum is to be confirmed at submission. The authors thank the Mackenzie and Biddle laboratories for sharing the CaLH3, Ca1 and Luc4 cell lines.

References:

[1] Warnakulasuriya, S., Reibel, J., Bouquot, J., & Dabelsteen, E. (2008). Oral epithelial dysplasia classification systems: predictive value, utility, weaknesses and scope for improvement. *Journal of Oral Pathology & Medicine*, 37(3), 127–133.

[2] Suresh, S. (2007). Biomechanics and biophysics of cancer cells. *Acta Biomaterialia*, 3(4), 413–438.

[3] Chen, Y.-Q., Lan, H.-Y., Wu, Y.-C., Yang, W.-H., Chiou, A., & Yang, M.-H. (2018). Epithelial–mesenchymal transition softens head and neck cancer cells to facilitate migration in 3D environments. *Journal of Cellular and Molecular Medicine*, 22(8), 3837–3846.

[4] Kontomaris, S. V., Malamou, A., & Stylianou, A. (2025). The Young's modulus as a mechanical biomarker in AFM experiments: a tool for cancer diagnosis and treatment monitoring. *Sensors*, 25(11), 3510.

[5] Varol, R., Karavelioglu, Z., Omeroglu, S., Aydemir, G., Karadag, A., Meco, H. E., Demircali, A. A., Yilmaz, A., Kocal, G. C., Gencoglan, G., Oruc, M. E., Esmer, G. B., Basbinar, Y., Ozdemir, S. K., & Uvet, H. (2022). Acousto-holographic reconstruction of whole-cell stiffness maps. *Nature Communications*, 13, 7351.

[6] Biddle, A., Liang, X., Gammon, L., Fazil, B., Harper, L. J., Emich, H., Costea, D. E., & Mackenzie, I. C. (2011). Cancer stem cells in squamous cell carcinoma switch between two distinct phenotypes that are preferentially migratory or proliferative. *Cancer Research*, 71(15), 5317–5326.

MXene-Based Nanoparticle-Modified Flexible Dual-Working-Electrode Electrochemical Sensor for Multiplexed Detection of Dopamine and Uric Acid

Dilara Yeniterzi[1,2], Esra Nur Elmas[1,2], Serdar Akbayrak[3], Saniye Soylemez[1,2,*]

[1]Faculty of Engineering, Department of Biomedical Engineering, Necmettin Erbakan University, 42100, Konya, Türkiye

[2]Science Technology Research and Application Center (BITAM), Necmettin Erbakan University, 42100, Konya, Türkiye

[3]Necmettin Erbakan University, Faculty of Engineering, Department of Basic Sciences, 42140, Konya, Türkiye

Dopamine (DA) and uric acid (UA) are important biomarkers associated with neurological function and oxidative stress. The simultaneous determination of these analytes has attracted considerable attention due to its potential applications in the diagnosis and monitoring of neurodegenerative diseases, particularly Parkinson's disease [1]. Owing to their electroactive nature, DA and UA can be effectively detected using electrochemical techniques [2]. However, the simultaneous electrochemical detection of dopamine (DA) and uric acid (UA) remains challenging due to their similar electrochemical behavior and the complexity of biological matrices [3]. To address these limitations, nanomaterial-modified electrodes have been extensively investigated for their ability to enhance electron-transfer kinetics and improve peak separation between target analytes [4]. Although DA and UA exhibit closely overlapping oxidation potentials, their simultaneous (multiplexed) detection can be achieved with high sensitivity using nanomaterial-modified electrodes that enhance signal resolution and electrocatalytic efficiency [5].

In this study, a flexible electrochemical sensing platform based on a dual-working-electrode (dual-WE) configuration is being developed for the simultaneous (multiplexed) detection of DA and UA using differential pulse voltammetry (DPV). The sensor is fabricated by modifying a flexible electrode substrate with nanomaterials via a simple drop-casting method. The proposed platform offers a promising wearable and non-invasive approach for real-time

biomarker monitoring. Preliminary electrochemical results demonstrate that the modified electrode provides well-resolved, distinct oxidation peaks for DA and UA, confirming the feasibility of simultaneous detection. Ongoing work focuses on optimizing analytical performance parameters, evaluating selectivity, and validating the sensor in artificial sweat matrices.

The flexible architecture, facile fabrication strategy, and compatibility with wearable sensing technologies position this platform as a strong candidate for future multiplexed monitoring of neurological and oxidative stress biomarkers in non-invasive health diagnostics.

Acknowledgement:

S. Soylemez acknowledges the NEU-BAP (ULAP-24UA19001) for financial support.

References:

[1] Seifar, F., Dinasarapu, A. R., & Jinnah, H. A. (2022). Uric acid in Parkinson′ s disease: what is the connection?. *Movement Disorders*, *37*(11), 2173-2183.

[2] Yang, L., Liu, D., Huang, J., & You, T. (2014). Simultaneous determination of dopamine, ascorbic acid and uric acid at electrochemically reduced graphene oxide modified electrode. *Sensors and Actuators B: Chemical*, *193*, 166-172.

[3] Zhou, F., Lim, H. N., Ibrahim, I., Endot, N. A., Malek, E. A., & Gowthaman, N. S. K. (2024). Simultaneous Electrochemical Detection of Dopamine and Uric Acid via Au@ Cu-Metal Organic Framework. *ChemPlusChem*, *89*(5), e202300686.

[4] Tonelli, D., Scavetta, E., & Gualandi, I. (2019). Electrochemical deposition of nanomaterials for electrochemical sensing. Sensors, 19(5), 1186.

[5] Tukimin, N., Abdullah, J., & Sulaiman, Y. (2018). Electrochemical detection of uric acid, dopamine and ascorbic acid. *Journal of the Electrochemical Society*, *165*(7), B258-B267.

Programmable FIP-Engineered LAMP Bypasses Independent CRISPR Target Design for Rapid Mpox Detection

Nazente Atceken[1,2,3*] & Savas Tasoglu[1,2,4,5,6,7]

[1]School of Biomedical Sciences and Engineering, Koç University, Istanbul, Turkey, 34450
[2]Koç University Translational Medicine Research Center (KUTTAM), Koç University, Istanbul, Turkey, 34450
[3]School of Medicine, Koç University, Istanbul, Turkey, 34450
[4]Department of Mechanical Engineering, Koç University, Istanbul 34450, Turkey
[5]Koç University Is Bank Artificial Intelligence Lab (KUIS AI Lab), Koç University, Istanbul, Turkey, 34450
[6]Koç University Arçelik Research Center for Creative Industries (KUAR), Koç University, Istanbul, Turkey, 34450
[7]Boğaziçi Institute of Biomedical Engineering, Boğaziçi University, Istanbul, Turkey, 34684
Presenter

1. Introduction

Rapid and sensitive detection of Mpox virus is essential for effective outbreak surveillance and disease control [1]. CRISPR/Cas12a-based diagnostics offer high specificity; however, they typically require independent target design and the availability of a protospacer adjacent motif (PAM) within the target sequence, which can complicate assay development [1-3]. In this study, we developed a programmable FIP-engineered LAMP strategy that incorporates a Cas12a-compatible PAM sequence directly into the amplification product, thereby eliminating the need for independent CRISPR target design and enabling rapid Mpox detection.

2. Material and Methods

Six LAMP primers targeting the *F3L* gene of Mpox virus were designed to generate specific amplification products [4, 5]. The forward inner primer (FIP), consisting of the F2 and F1c regions, was modified by inserting a TTTN sequence between F2 and F1c to introduce a Cas12a-compatible PAM motif into the resulting LAMP amplicon. Subsequently, crRNAs were designed directly against the engineered FIP-derived sequence. LAMP reactions were performed using the LavaLAMP™ kit. CRISPR detection assays employed LbCas12a nuclease (GenScript) and a FAM-ssDNA-BHQ1 fluorescent reporter. Fluorescence signals were measured using a qPCR instrument, and endpoint fluorescence values were recorded. Colorimetric fluorescence visualization was also performed under appropriate illumination conditions.

3. Results and Discussion

The engineered FIP design successfully enabled Cas12a activation and specific detection of Mpox-derived LAMP products. Using LAMP products generated from 25 ng/µL plasmid Mpox DNA, different volumes of amplification product (4, 3, and 2 µL) were introduced into 20 µL CRISPR/Cas12a reactions. Endpoint fluorescence signals increased proportionally with template concentration, yielding 599 RFU, 498 RFU, and 390 RFU for 4, 3, and 2 µL LAMP products, respectively, while no fluorescence signal was detected in the negative control. Visual fluorescence imaging confirmed stronger fluorescence intensity at higher LAMP product concentrations. To evaluate reporter concentration effects, reactions containing 4 µL of LAMP product were tested with 3, 2, and 1 µL of 100 nM FAM-ssDNA- BHQ1 reporter. Increasing

reporter concentration resulted in enhanced fluorescence output, producing 1196 RFU, 898 RFU, and 599 RFU, respectively. In contrast, reactions lacking LAMP amplicons produced no detectable fluorescence regardless of reporter concentration, demonstrating that Cas12a activation was strictly dependent on the presence of specific target DNA and did not generate non-specific background signals. Colorimetric fluorescence imaging further validated these findings. These results demonstrate that incorporating a programmable PAM sequence into the FIP primer enables direct crRNA design against the engineered amplification product, simplifying CRISPR assay development while maintaining high specificity and signal responsiveness.

Conclusion

The programmable FIP-engineered LAMP approach provides a simple and effective strategy for integrating CRISPR/Cas12a detection without requiring independent CRISPR target selection. By embedding a PAM motif directly into the LAMP amplicon, the assay enables flexible crRNA design, robust Cas12a activation, and specific detection of Mpox DNA. This platform represents a promising framework for rapid, adaptable, and field- deployable molecular diagnostics for Mpox and other emerging pathogens.

Acknowledgement:

S.T. acknowledges TÜBİTAK 2232 International Fellowship for Outstanding Researchers Award (118C391), TÜBİTAK-1001 Scientific and Technological Research Projects (123S582 and 123Z050), Alexander von Humboldt Research Fellowship for Experienced Researchers, Marie Skłodowska-Curie Individual Fellowship (101003361), and Royal Academy Newton Katip Çelebi Transforming Systems Through Partnership Award (120N019) for the financial support of this research. N.A. acknowledges support by EMBO Scientific Exchange Grant (11627) and TÜBİTAK-2218 Domestic Postdoctoral Research Scholarship Project (122C195). This study was conducted using the service and infrastructure of Koç University Translational Medicine Research Center (KUTTAM).

References:

[1] N. Atceken, I. Bayaki, B. Can, D. Yigci, and S. Tasoglu, "Mpox disease, diagnosis, and point of care platforms," Bioengineering & Translational Medicine, vol. 10, no. 3, p. e10733, 2025.
[2] N. Atceken, A. Kahya, D. Yigci, and S. Tasoglu, "CRISPR-on-Chip for Point-of-Care Diagnostics," ACS nano, 2026.
[3] N. Atçeken, D. Yigci, B. Ozdalgic, and S. Tasoglu, "CRISPR-Cas-Integrated LAMP," Biosensors, vol. 12, no. 11, p. 1035, 2022. [Online]. Available: https://www.mdpi.com/2079-6374/12/11/1035.
[4] N. Atceken, A. C. Abdullah, O. Ozarslan, Z. Yıldız, and S. Tasoglu, "Machine Learning-Augmented Loop-Mediated Isothermal Amplification-Enabled Point-of-Care for Mpox-Specific Detection," Advanced Intelligent Systems, p. e202500825, 2026.
[5] M. T. Birtek, N. Atçeken, and S. Tasoglu, "Programmable 3DP Microfluidic Bio-Reaction System: Automated LAMP-on-a-Chip," Lab on a Chip, 2025, doi: 10.1039/d5lc00003c.

Sub-100 nm Ti-MIL-125 and V-MIL-47 Nanoparticles via Synergistic Seeding-Assisted Droplet Microfluidics: Overcoming Residence Time Limitations

E.Gökçen DİLCİ, Selis ÖNEL*

Hacettepe University, Department of Chemical Engineering, Ankara, Turkiye

1. Introduction

Materials featuring a metal organic framework (MOF) crystalline architecture have garnered significant attention due to their advantageous mesoporosity, high surface area-to-volume ratio, and tunable catalytic properties. These attributes render MOF structures highly suitable for a diverse range of applications across the defense, pharmaceutical, paint and coating, and energy sectors, including adsorption and separation processes [1, 2], targeted drug delivery [3-5], and heterogenous catalysis [6, 7]. Conventionally, the synthesis of MOF particles relies on solvothermal methods conducted in laboratory-scale autoclaves. This approach presents limitations because macroscale nucleation kinetics are temporally and spatially heterogeneous throughout the reactor volume leading to uncontrolled variations in crystal growth and morphology.

To address these limitations, droplet-based microfluidic systems offer a compelling alternative, where the contact of immiscible phases within microchannels drives the interfacial tension-mediated breakup of the dispersed phase. Via adjustment of nozzle widths and fluid flow rates, the dimensions of the resulting droplets can be precisely manipulated. Consequently, these systems are characterized by their ability to generate monodisperse droplets at constant flow conditions, providing a highly reproducible reaction environment.

Building upon their hydrodynamic advantages, the implementation of picoliter droplets as isolated reactors facilitates accelerated heat and mass transfer compared to macroscale systems. Solvothermal synthesis in such miniaturized dynamic systems yields monodisperse particles in the nanometer range, as successfully demonstrated in the synthesis of stable transition-metal-based frameworks, such as those incorporating zirconium (Zr) and copper (Cu) [8, 9].

MOF architectures incorporating less stable transition metals, such as titanium (Ti) [10] and vanadium (V) [11], often exhibit slower crystallization rates and typically yield larger particles on the micrometer scale. Because these frameworks necessitate longer synthesis times, they pose a specific operational challenge for microfluidic systems as the physical channel dimensions inherently limit the available residence times.

To overcome these constraints and extend the capabilities of continuous-flow droplet-based microfluidics, this study employs a two-phase microfluidic system designed to precisely regulate nucleation kinetics and achieve high product uniformity. To compensate for the time limitations inherent to microfluidic residence times, heterogeneous nucleation was induced via seeding [12]. This strategy lowers the thermodynamic energy barrier within the droplet reactors, ultimately facilitating the synthesis of highly monodisperse V-MIL-47 and Ti-MIL-125 nanoparticles in the sub-100 nm range.

2. Materials and Methods

All chemicals used in the experiments were of analytical grade and procured commercially from Sigma-Aldrich, St. Louis, Missouri, USA, unless otherwise specified. The precursor solution comprised one or more of the solvents n,n-dimethylformamide (DMF) ($(CH_3)_2NC(O)H$, 99.8%), 1-methyl-2-pyrrolidone (NMP) (C_5H_9NO, 99%), and methanol (M) (CH_3OH, 99%). The organic ligand employed was terephthalic acid (H_2BDC) ($C_8H_6O_4$, >98%) and the metal salt was vanadium vanadium(IV) sulfate oxide hydrate ($VOSO_4(H_2O)x$, >99%) and titanium isopropoxide (TTIP) ($Ti[OCH(CH_3)_2]$, >99%).

The microfluidic device with a flow-focusing geometry was fabricated using polydimethylsiloxane (PDMS) (Slygard 184, Dow Corning, Corning, NY) using a 10/1 base to curing agent ratio by weight via standard soft photolithography. Silicone oil ($CH_3[Si(CH_3)_2O]_nSi(CH_3)_3$), with a kinematic viscosity of 1000 cSt, was used as the continuous phase, which was supplemented with the surfactants sorbitan monooleate (Span 80, $C_{24}H_{44}O_6$) and dioctyl sulfosuccinate (AOT, $C_{20}H_{37}NaO_7S$) to inhibit droplet coalescence.

Precursor solution was prepared using a systematic protocol. Initially, the metal salt and organic ligand were dissolved in the solvent and sonicated for 10 minutes to ensure thorough mixing.

2.1 Microfluidic Synthesis

Microfluidic synthesis consists of a multi-syringe pump system for transfer of two different fluids, a microfluidic device for droplet generation, and thermal activation for crystallization as represented in Figure 1. Precursor solution and silicone oil were transferred via 1 mL syringes and Masterflex® polytetrafluoroethylene (PTFE) (Masterflex Transfer Tubing, Avantor, Inc, USA) tubing with 0.012" ID x 0.030" OD. Microdroplets were transported through a 2 m long heated channel using a larger diameter tubing with 0.024" ID x 0.030" OD. Fluid flow was controlled by Nemesys BASE120 syringe pumps (CETONI GmbH, Germany). To achieve monodisperse reactors with diameters of 50-60 mm and the desired residence time, the flow rates were set at 0.6 µL/min for dispersed phase and 3.6 µL/min for the continuous phase. After the completion of the synthesis, particles were washed with xylene (C_8H_{10}, ≥99%, ISOLAB) at least three times to dissolve and remove the silicone oil surrounding the particles. Washing procedure after the removal of silicone oil is the same as that in the solvothermal synthesis.

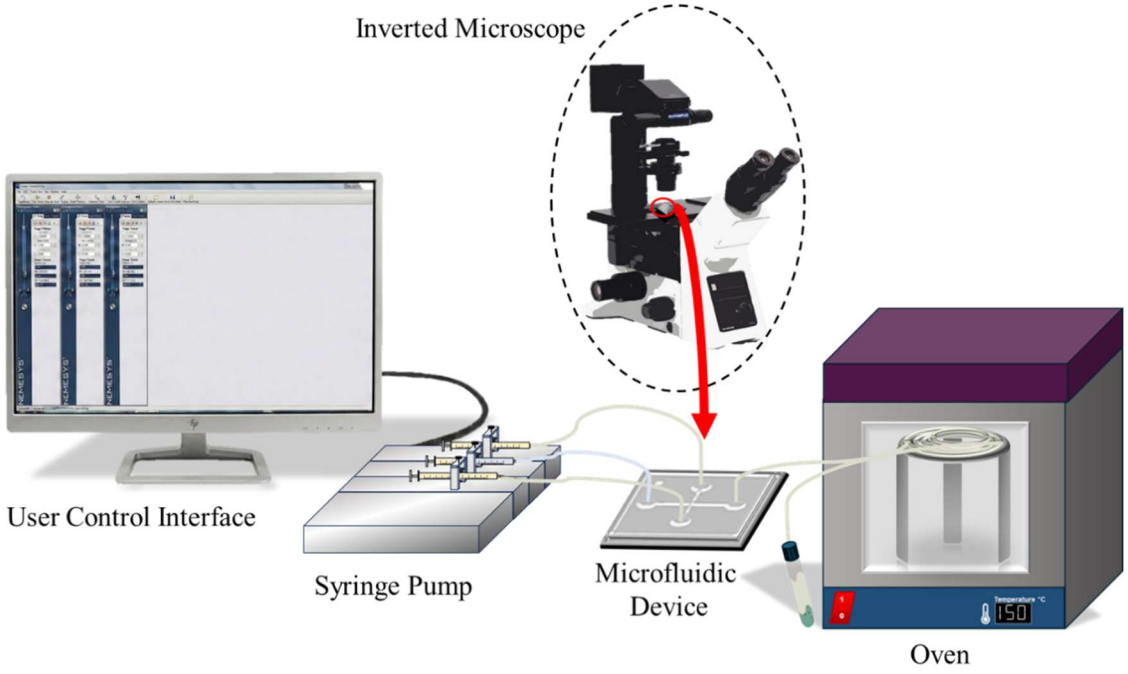

Figure 1. Schematic representation of microfluidic synthesis, including the syringe pump system, microfluidic device for droplet generation, and thermal activation for crystallization.

2.2 Synthesis via Seeding

To facilitate heterogeneous nucleation, a comparative study was performed to evaluate the effect of seeding. This was achieved by incorporating pre-synthesized V-MIL-47 and Ti-MIL-125 seeds in the precursor solution. Specific seed dimensions and concentrations are presented in Table 1.

Table 1. Composition of precursor solution and synthesis conditions using seeding.

Metal Salt g		Ligand g	Solvent mL		Seed mg		Seed Size nm	Temp. °C	Time h
$VOSO_4$	*TTIP*	*H_2BDC*	*DMF*	*NMP/M*	*V-MIL-47*	*Ti-MIL-125*			
0.241		0.179	5		5		0	150	2
							136		
							1097		
	0.0952	0.195		4.5/0.5		5	0	190	2
							873	190	2

3. Results and Discussion

Macroscale synthesis with seeds initially resulted in non-crystalline particles (Figure 2.a-b.). Introduction of 1097 nm seeds accelerated the nucleation process. This transformation facilitated the formation of desired crystalline structure and limited particle growth, resulting in a final average particle size (D_{avg}) of 87.7±17 nm, as shown in Figure 2.c.

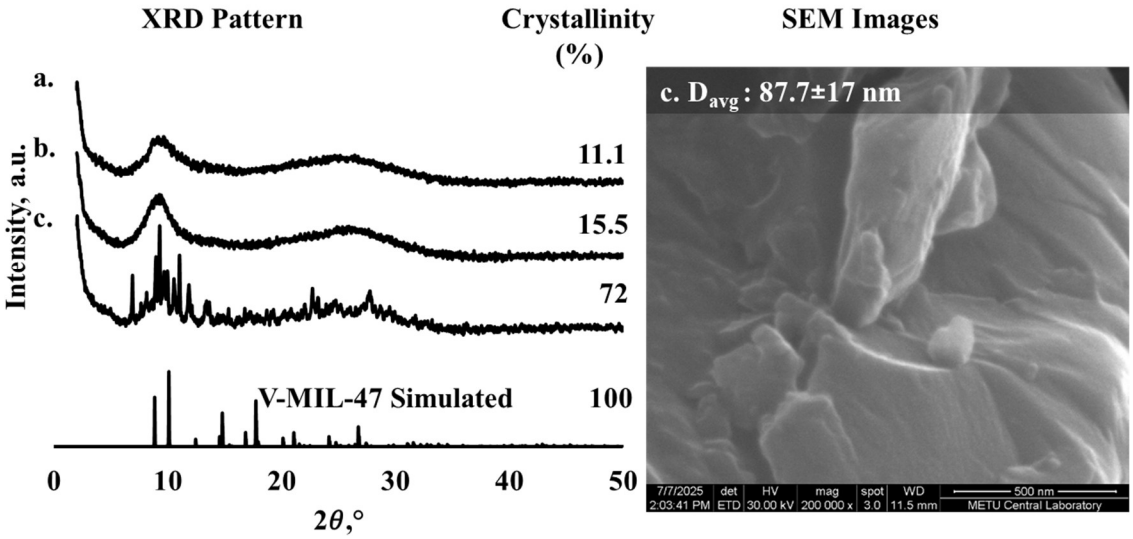

Figure 2. XRD profile, crystallinity, and SEM micrograph (200,000x magnification) of V-MIL-47 nanoparticles produced at 150°C and 2 hours in macroscale autoclaves using **a. no seeds**, **b. 136 nm seeds**, and **c. 1097 nm seeds**.

Microfluidic synthesis, utilizing the same precursor composition, temperature and residence time as the macroscale synthesis, facilitated crystallization and yielded smaller particles (Figure 3). Crystallinity of the particles increased by 5%. This enhancement allowed better control over crystal growth, leading to significantly refined particle sizes. Microfluidic synthesis resulted in a 23.6 % reduction in particle size compared to macroscale synthesis. Enhanced mass and heat transfer in microfluidic synthesis, in corroboration with heterogeneous nucleation kinetics, led to enhanced nucleation kinetics.

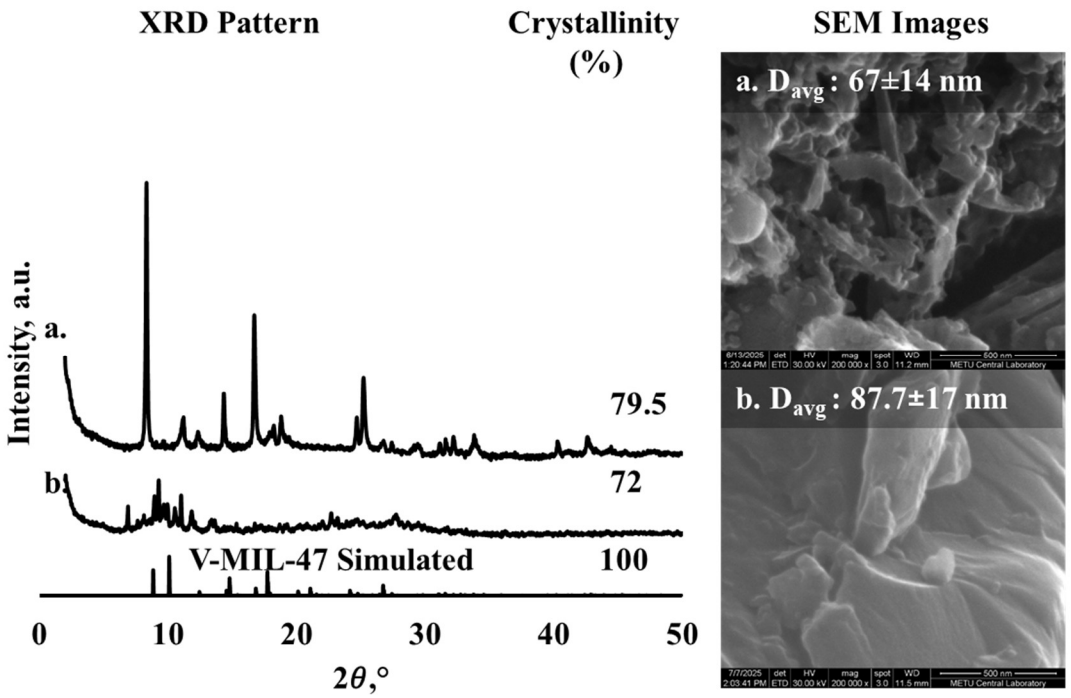

Figure 3. XRD profile, crystallinity, and SEM micrograph (200,000x magnification) of V-MIL-47 nanoparticles produced at 150°C and 2 hours using 1097 nm seeds via **a. microfluidic** and **b. macroscale autoclave** systems.

Microfluidic synthesis was conducted using 873 nm Ti-MIL-125 nanoparticles as heterogeneous nucleation sites. Seeded synthesis facilitated size control, resulting in particles of 51.4 nm using the microfluidic system compared to 189 nm using the macroscale system (Figure 4). Conversely, the crystallinity of the particles reduced to 33% from 52.6%. These results indicate that nucleation kinetics in macroscale systems are less controllable compared to microfluidic systems. The increased rate of nucleation in the microfluidic system leads to smaller particles, whereas the increased rate of crystal growth in the macroscale system leads leading to larger particle sizes as observed in.

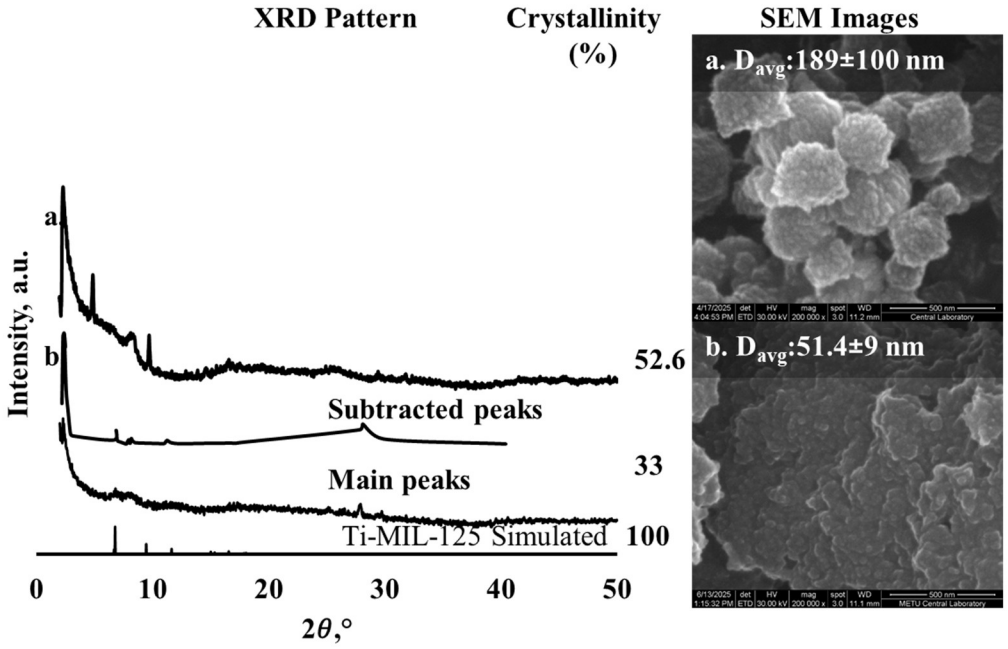

Figure 4. XRD profile and crystallinity of Ti-MIL-125 nanoparticles synthesized at 190 °C and 2 hours via the **a. macroscale route** and **b. microfluidic route using 873 nm seeds.**

Consequently, the integration of heterogeneous nucleation sites within the microfluidic system offers better control over crystal growth. Comparatively, in the macroscale system, these extra nucleation sites may result in poor crystallinity (Figure 2). This is further supported by Figure 4, where the non-seeded synthesis of Ti-MIL-125 structures yielded higher crystallinity than seeded counterparts.

Conclusion

Our work demonstrated that integrating a seeding strategy within a microfluidic system enables accelerated nucleation with refined morphological control. Microfluidic systems ensure homogeneous size distribution, while the seeding approach overcomes the residence time limitation of microfluidic systems. This comparative study effectively addressed the limitations of solvothermal synthesis via the conventional macroscale route based on autoclave reactors, where identical conditions resulted in amorphous or profoundly agglomerated particles. Collectively, the synergistic effects of employing a microfluidic solvothermal route with seeding facilitate the production of monodisperse MOF structures with higher yield.

Acknowledgements

This study was supported by The Scientific and Technological Research Institution of Turkiye (TUBITAK) through the 1001 Research Projects Funding Program project no: 220M002 and by Hacettepe University BAP projects, no: FHD-202420812 and FYL-2026-22074.

References

[1] W. Wang, Y. C. Chen, P. Y. Feng, and X. H. Bu, "Tailorable Multi-Modular Pore-Space-Partitioned Vanadium Metal-Organic Frameworks for Gas Separation," (in English), *Adv Mater,* vol. 36, no. 30, Jul 2024, doi: 10.1002/adma.202403834.

[2] Y. Z. Li *et al.*, "A moisture stable metal-organic framework for highly efficient CO2/N2, CO2/CH4 and CO2/CO separation," (in English), *Chem Eng J,* vol. 484, Mar 15 2024, doi: 10.1016/j.cej.2024.149494.

[3] Y. S. Lin, K. S. Lin, N. V. Mdlovu, M. T. Weng, W. C. Tsai, and U. S. Jeng, "Synthesis of a MIL-125(Ti) carrier for thermal-and pH-responsive drug release," (in English), *Biomater Adv,* vol. 140, Sep 2022, doi: 10.1016/j.bioadv.2022.213070.

[4] A. Rengaraj *et al.*, "Porous NH_2-MIL-125 as an efficient nano-platform for drug delivery, imaging, and ROS therapy utilized Low-Intensity Visible light exposure system," (in English), *Colloid Surface B,* vol. 160, pp. 1-10, Dec 1 2017, doi: 10.1016/j.colsurfb.2017.09.011.

[5] K. Suresh and A. J. Matzger, "Enhanced Drug Delivery by Dissolution of Amorphous Drug Encapsulated in a Water Unstable Metal-Organic Framework (MOF)," (in English), *Angew Chem Int Edit,* vol. 58, no. 47, pp. 16790-16794, Nov 18 2019, doi: 10.1002/anie.201907652.

[6] X. Han, X. B. Yang, G. B. Liu, Z. H. Li, and L. Shao, "Boosting visible light photocatalytic activity via impregnation-induced RhB-sensitized MIL-125(Ti)," (in English), *Chem Eng Res Des,* vol. 143, pp. 90-99, Mar 2019, doi: 10.1016/j.cherd.2019.01.010.

[7] S. S. Hu *et al.*, "Location-Specific Microenvironment Modulation Around Single-Atom Metal Sites in Metal-Organic Frameworks for Boosting Catalysis," (in English), *Angew Chem Int Edit,* vol. 64, no. 3, Jan 15 2025, doi: 10.1002/anie.202415155.

[8] M. Faustini *et al.*, "Microfluidic Approach toward Continuous and Ultrafast Synthesis of Metal-Organic Framework Crystals and Hetero Structures in Confined Microdroplets," (in English), *J Am Chem Soc,* vol. 135, no. 39, pp. 14619-14626, Oct 2 2013, doi: 10.1021/ja4039642.

[9] S. Onel, B. Parlak, G. Korkmaz, and E. G. Dilci, "Effect of Miniaturization Using Droplet Based Micro Fluidic Systems on the Synthesis of Uio-66 Mof Nanoparticles," (in English), *Proceedings of Asme 2023 International Mechanical Engineering Congress and Exposition, Imece2023, Vol 4,* 2023. [Online]. Available: <Go to ISI>://WOS:001216797200037.

[10] J. E. Knapp *et al.*, "Dynamic breathing behaviour of the titanium-based metal-organic framework NTU-9 upon adsorption of water and organic solvents," (in English), *Chem Sci,* vol. 16, no. 30, Jul 30 2025, doi: 10.1039/d5sc02585k.

[11] P. Van der Voort *et al.*, "Vanadium metal-organic frameworks: structures and applications," (in English), *New J Chem,* vol. 38, no. 5, pp. 1853-1867, 2014, doi: 10.1039/c3nj01130e.

[12] D. R. D. Bois and A. J. Matzger, "Metal-Organic Framework Seeding to Drive Phase Selection and Overcome Synthesis Limitations," (in English), *Cryst Growth Des,* Oct 19 2022, doi: 10.1021/acs.cgd.2c00762.

Optimized Nature-Inspired Geometries for Sweat Analysis: Minimizing Effective Saturation Time in Paper-Based Microfluidic Devices

A. C. Abdullah[1], J. Jalilov[1], E. Ahmadinejad[1], A. Ahmadpour[1], and S. Tasoglu[1,2,3,4,5,6,*]

[1]*Department of Mechanical Engineering, Koç University, Turkey*

[2]*Department of Biomedical Sciences and Engineering, Koç University, Turkey*

[3]*School of Medicine, Koç University, Istanbul 34450, Turkey.*

[4]*Koç University Translational Medicine Research Center (KUTTAM), Koç University, Turkey*

[5]*Koç University Is Bank Artificial Intelligence Lab (KUIS AILab), Koç University, Turkey*

[6]*Koç University Arçelik Research Center for Creative Industries (KUAR), Koç University, Turkey*

Wearable sweat sensors offer continuous, non-invasive access to physiological biomarkers, but their response depends on how rapidly and completely sweat is delivered from the skin to the sensing electrode. In pump-free, paper-based microfluidic chips this transport is governed almost entirely by the porous collecting geometry, which is still designed largely by trial and error [1]. We present a physics-grounded, surrogate-assisted optimization framework that treats the chip geometry as a design variable and simultaneously minimizes the effective saturation time (T_{95}) and maximizes analyte delivery to the sensor.

Three nature-inspired radial-arm architectures were modeled by coupling Richards' equation for unsaturated capillary flow with the Transport of Diluted Species for sodium-ion (Na^+) transport in COMSOL Multiphysics. The workflow was automated through the MATLAB-COMSOL LiveLink interface to build a simulation dataset spanning the geometric design space. Gaussian Process Regression (GPR) surrogates with a Matérn kernel were trained on this dataset and coupled to a single-objective genetic algorithm and the multi-objective NSGA-II algorithm, reducing each design evaluation from minutes to microseconds. Selected candidate geometries were then validated against full COMSOL simulations [2].

The three architectures occupy complementary regions of the trade-off between saturation time and surface coverage (SC_{T95}). Design 1 (simple radial arms) shows a genuine speed-delivery trade-off and provides the fastest-saturating geometry ($T_{95} \approx 45.4$ s), whereas Design 3 (single separating ring) delivers the highest analyte coverage ($SC_{T95} \approx 0.16$); the double-ring Design 2 is entirely dominated. Across fifteen COMSOL-validated candidates, the global Pareto front is formed exclusively by Designs 1 and 3. Surrogate reliability was design-dependent (mean absolute percentage errors of 4.3%, 13.8% and 8.3% for Designs 1-3), and the calibrated GPR uncertainty correctly flagged extrapolation beyond the sampled space.

The framework offers a transferable, computationally efficient route to the rational design of paper-based sweat chips and reframes the problem as an architecture choice: simple radial arms when saturation speed is paramount, and a single separating ring when maximal analyte delivery is required.

Acknowledgements. The authors acknowledge TÜBİTAK-1001 Scientific and Technological Research Projects (Grant Nos. 123S582 and 123Z050) for financial support of this research.

References

[1] C. Huang, et al., Quantitative analysis for sweat-absorbing times of paper-based microfluidic chips, Microfluidics and Nanofluidics 28(1) (2024) 1.

[2] M.T. Birtek, V. Aktas, B. Aktas, A.C. Abdullah, A. Ozcan, S. Tasoglu, ML-automated microfluidic circuit design (μFluidicGenius), Science Advances (2026).

Numerical and Experimental Investigation of Microscale Wall-Profile Effects on Single-Phase Flow and Heat Transfer in Mini-Channels

Ariya Rahmani[1], Omid Najafikia[1], Omid Moradi[1,2], Ali Koşar[1,2]*

[1]Department of Mechatronics Engineering, Faculty of Engineering and Natural Sciences, Sabancı University, Istanbul, Türkiye

[2]Sabancı University Center of Excellence for Functional Surfaces and Interfaces for Nanodiagnostics (EFSUN), Istanbul, Türkiye

*Corresponding author: ali.kosar@sabanciuniv.edu

[1] Introduction

Mini- and micro-channels are widely used in compact heat exchangers, electronics cooling, biomedical devices, and lab-on-a-chip systems because their high surface-area-to-volume ratio enables efficient heat removal within a small volume [1]. Their main limitation is that any attempt to intensify convection generally increases flow resistance and pumping-power demand. One passive approach is to modify the internal wall of the channel. Periodic corrugations repeatedly contract and expand the flow passage, disturb the hydrodynamic and thermal boundary layers, and can therefore increase the heat-transfer rate without moving components or external actuation [2,3]. However, the same disturbances also produce additional viscous and form losses. The useful design question is therefore not simply which wall produces the highest heat transfer, but which geometry provides the most favorable balance between thermal enhancement and pressure-drop penalty.

This study was designed to answer that question for a circular mini-channel with manufacturable microscale wall features. Three internal profiles: trapezoidal, triangular, and sinusoidal, were compared at two wave amplitudes. The numerical investigation was used to explain how each profile changes the local velocity and temperature fields and to quantify its heat-transfer and pressure-drop performance relative to a smooth channel. Matching test sections were then produced and tested in a single-phase water loop to determine whether the experimentally measured hydraulic trends followed the numerical predictions.

[2] Materials and Methods

The investigated channel had an inner diameter of 3 mm and was divided into three consecutive regions. A 70 mm smooth inlet section allowed the flow to develop before reaching the modified wall. This was followed by a 10 mm test section containing the corrugations and a 12 mm smooth outlet section that reduced the influence of the outlet boundary condition on the test region. The modified section contained five waves with a wavelength of 2 mm. Trapezoidal, triangular, and sinusoidal profiles were studied at amplitudes of 300 µm and 600 µm. A smooth channel with the same diameter and total length was used as the reference geometry. This arrangement made it possible to isolate the influence of wall shape and amplitude while keeping the remaining channel dimensions unchanged.

The numerical model was developed in COMSOL Multiphysics. Water was modeled as a steady, laminar, incompressible, Newtonian fluid with constant thermophysical properties. The conservation equations of mass, momentum, and energy were solved through a non-isothermal finite-element formulation. A uniform velocity and prescribed temperature were applied at the inlet, the outlet was assigned a gauge-pressure condition, and no-slip conditions were imposed on all channel walls. The inlet and outlet sections were thermally insulated, whereas a constant wall temperature was applied to the modified test section. For the smooth-channel validation

case, the thermal boundary condition was applied in a manner consistent with the reference internal-flow configuration.

A strongly refined finite-element mesh was generated around the wave peaks, inclined surfaces, and cavities, where the largest velocity, wall-shear, and temperature gradients were expected. The local heat-transfer coefficient was calculated from the wall heat flux and the difference between the wall temperature and a velocity-weighted bulk-fluid temperature. Local and average Nusselt numbers were then used to compare the thermal response of the profiles. The pressure difference between the channel inlet and outlet was used to evaluate hydraulic performance.

For the experimental part, test sections with the same internal profile shapes were prepared by additive manufacturing. Each sample included an external hexagonal body, integrated threaded ends, and sealing surfaces for connection to the flow loop. Water was supplied from a reservoir by a pump. A bypass line equipped with a metering valve was used to reduce pump-induced pulsations, and a flow straightener was installed upstream of the test section. The volumetric flow rate was monitored with an inline flowmeter, while pressure sensors located immediately upstream and downstream of the sample measured the pressure difference. The experiments were used primarily to compare the hydraulic behavior of the manufactured profiles with the numerical pressure-drop trends.

When the flow entered a modified section, the cross-sectional area changed repeatedly. The fluid accelerated through the narrow portions of each wave and decelerated inside the wider cavities. As a result, the near-wall boundary layer was repeatedly thinned, displaced, and redeveloped. The strongest local heat-transfer regions appeared near the contractions and on surfaces where the flow was redirected, whereas low-velocity zones formed inside the cavities. Increasing the amplitude from 300 μm to 600 μm made the contractions more severe, enlarged the cavity regions, and intensified both the local thermal gradients and the hydraulic losses.

All three profiles improved the average heat transfer relative to the smooth channel, but the magnitude depended strongly on shape and amplitude. At an amplitude of 300 μm, the trapezoidal, sinusoidal, and triangular profiles increased the average heat-transfer performance by approximately 26%, 22%, and 17%, respectively. At 600 μm, the corresponding enhancements increased to approximately 62%, 55%, and 46%. Thus, the larger amplitude moved the enhancement range from 17-26% to 46-62%. The trapezoidal wall produced the highest thermal improvement because its abrupt changes in flow area caused the strongest acceleration and boundary-layer interruption. The triangular wall produced the lowest enhancement, while the smoother sinusoidal wall remained between the other two profiles.

The pressure-drop results showed the opposite side of the same mechanism. The trapezoidal profile produced the largest hydraulic resistance, the triangular profile produced the smallest, and the sinusoidal profile was intermediate. At 300 μm, the pressure drop of the trapezoidal profile was approximately 60-70% higher than that of the triangular and sinusoidal profiles. At 600 μm, the difference between the trapezoidal profile and the other two narrowed to approximately 10-16%, although the trapezoidal geometry still remained the most resistive. Increasing the amplitude from 300 μm to 600 μm increased the pressure drop by roughly 130-240%, depending on the profile. This increase was much larger than the corresponding thermal gain, demonstrating that amplitude cannot be selected solely on the basis of heat-transfer enhancement.

The experimental measurements reproduced the same hydraulic ranking as the simulations. The trapezoidal samples required the largest pressure difference, the triangular samples the smallest, and the sinusoidal samples showed an intermediate response. The higher-amplitude samples

also produced substantially larger pressure drops than their lower-amplitude counterparts. Differences between numerical and experimental values are expected because the manufactured channels include surface roughness, dimensional tolerances, fitting losses, and residual flow pulsations that are not represented explicitly in the idealized numerical model. Nevertheless, agreement in the profile ordering and in the effect of amplitude supports the use of the numerical model for comparative design.

Conclusion

The study clearly demonstrates how the internal wall profile controls the thermo-hydraulic behavior of a circular mini-channel. Trapezoidal corrugations generated the strongest boundary-layer disturbance and therefore the highest heat-transfer enhancement, but they also imposed the largest pressure-drop penalty. Triangular corrugations minimized flow resistance but provided the smallest thermal improvement. Sinusoidal corrugations produced intermediate heat-transfer and pressure-drop behavior and therefore offered the most balanced response among the investigated profiles. Increasing the wave amplitude substantially improved heat transfer, but the accompanying increase in pressure drop was proportionally greater. The combined numerical and experimental approach provides a practical basis for selecting manufacturable wall geometries according to the thermal requirement and the available pumping capacity of compact cooling and microfluidic systems.

Acknowledgement:

The authors gratefully acknowledge the support of Sabancı University and the facilities provided by EFSUN.

References:

[1] D. B. Tuckerman and R. F. W. Pease, “High-performance heat sinking for VLSI,” *IEEE Electron Device Letters*, vol. 2, no. 5, pp. 126-129, 1981.

[2] Y. Sui, C. J. Teo, P. S. Lee, Y. T. Chew, and C. Shu, “Fluid flow and heat transfer in wavy microchannels,” *International Journal of Heat and Mass Transfer*, vol. 53, pp. 2760-2772, 2010.

[3] A. Rahmani, M. Najafigamasaei, M. R. Ansari, and S. Khodadadi, “Slug flow heat transfer rate in wavy walls microtubes by applying the modified volume of fluid method,” *Journal of Micromechanics and Microengineering*, vol. 35, no. 9, p. 095014, 2025.

[4] M. Akbarzadeh, S. Rashidi, and J. A. Esfahani, “Influences of corrugation profiles on entropy generation, heat transfer, pressure drop, and performance in a wavy channel,” *Applied Thermal Engineering*, vol. 116, pp. 278-291, 2017.

Development and Optimization of CRISPR/LAMP-Based Lateral Flow Assay Platform for Human Mpox Detection

Cagla Parmaksizoglu[1,2*], Isil Cakiroglu[1,2], Begum Kubra Tokyay[1,2], Nazente Atceken[1,2,3], and Savas Tasoglu[1,2,3,4,5,6,7]

[1]School of Biomedical Sciences and Engineering, Koç University, Istanbul, Turkey, 34450
[2]Koç University Translational Medicine Research Center (KUTTAM), Koç University, Istanbul, Turkey, 34450
[3]School of Medicine, Koç University, Istanbul, Turkey, 34450
[4]Department of Mechanical Engineering, Koç University, Istanbul 34450, Turkey
[5]Koç University Is Bank Artificial Intelligence Lab (KUIS AI Lab), Koç University, Istanbul, Turkey, 34450
[6]Koç University Arçelik Research Center for Creative Industries (KUAR), Koç University, Istanbul, Turkey, 34450
[7]Boğaziçi Institute of Biomedical Engineering, Boğaziçi University, Istanbul, Turkey, 34684
[*]*Presenter*

1. Introduction

Lateral flow assay (LFA) is a biosensor platform generally based on antigen-antibody or nucleic acid-based interactions, enabling rapid and cost-effective diagnosis [1, 2]. Its portable structure makes it widely used in the detection of various diseases [1, 3-5]. LFA systems generally consist of a sample pad, conjugate pad, nitrocellulose membrane (NC membrane), and absorbent pad; however, they can be diversified with different structural designs, such as single-line (sandwich-type), competitive, multiple-line, or microfluidic-based designs, depending on the intended use [1, 2]. The lack of point of care devices (PoC) for Monkeypox virus (MPXV) led to the development of this detection platform using LFA.- In this study, we developed and optimized a gold nanoparticle-based LFA platform suitable for CRISPR/LAMP molecular testing for the detection of human Mpox using anti-FAM functionalized gold nanoparticles (AuNPs) and a FAM-ssDNA-Biotin probe.

2. Materials and Methods

Between 5-20 nm gold nanoparticles (AuNPs) were synthesized and conjugated with anti-FAM antibodies to generate the reporter particles. Different antibody concentrations were tested, and then the conjugates were prepared under optimized buffer and various pH (8, 8.5, 9) conditions and stabilized using protein-based blocking strategies. The optimum conditions were then selected and the strip was assembled. The pads were overlapped to support efficient capillary flow. Different capture antibodies including anti-Biotin and anti-IgG were immobilized on the NC membrane for the detection. The FAM-ssDNA-Biotin probe was tested at different concentrations, and buffer conditions were optimized to improve probe-conjugate interaction, flow behaviour, and signal intensity. Nanoparticle synthesis, conjugation, and molecular interactions were further characterized using methods including UV-Vis spectroscopy, dynamic light scattering, zeta potential analysis, and isothermal titration calorimetry. Further, negative and positive test trials were run on the strips for 15 minutes using Mpox plasmid sample (FAM-ssDNA-Biotin probe).

3. Results and Discussion

The synthesized AuNPs exhibited characteristic optical properties, and surface modification with anti-FAM antibodies produced measurable changes in the nanoparticle behaviour which supported successful conjugation. In the lateral flow format, the AuNP-anti-FAM conjugates

migrated efficiently through the strip and produced a visible control line, confirming successful strip assembly, capillary flow, and conjugation. Further, a visible anti-Biotin test line was obtained in the presence of the uncut version of the FAM-ssDNA-Biotin probe. This demonstrated that the probe could interact with the AuNP-anti-FAM conjugates and subsequently be captured at the test region. Also, optimization of the probe concentration, membrane capture chemistry, and buffer composition improved test line visibility. The successful formation of both test and control lines confirmed the functional integration of the nanoparticle reporter, and the negative test trials.

Conclusion

This study demonstrated the successful development and optimization of a AuNPs-based LFA platform for the detection of MPXV. The formation of a visible anti-Biotin test line confirmed the functionality of the AuNP-anti-FAM/FAM-ssDNA-Biotin probe system (negative test control), while the control line (anti-IgG line on the NC membrane) verified proper conjugate migration and strip performance. Our future work will focus on evaluating the analytical sensitivity and specificity.

Acknowledgement:

This research was funded from TÜBİTAK-1001 Scientific and Technological Research Project (123S582) and TÜBİTAK-218 Domestic Postdoctoral Research Scholarship Project (122C195)

References:

[1] S. H. Kim, J. Lee, B. H. Lee, C.-S. Song, and M. B. Gu, "Specific detection of avian influenza H5N2 whole virus particles on lateral flow strips using a pair of sandwich-type aptamers," *Biosensors and Bioelectronics,* vol. 134, pp. 123–129, 2019/06/01/ 2019, doi: https://doi.org/10.1016/j.bios.2019.03.061.

[2] J. W. Guo, H. Y. Ho, C. Y. Dai, Y. H. Chen, M. L. Yu, and L. S. Yu, "Single-tube, single-strip lateral flow assays utilizing loop-mediated isothermal amplification for simultaneous hepatitis B and C viral detection," (in eng), *J Med Virol,* vol. 96, no. 6, p. e29721, Jun 2024, doi: 10.1002/jmv.29721.

[3] J. Wang *et al.*, "Development of aptamer-based lateral flow devices for rapid detection of SARS-CoV-2 S protein and uncertainty assessment," *Talanta,* vol. 281, p. 126825, 2025/01/01/ 2025, doi: https://doi.org/10.1016/j.talanta.2024.126825.

[4] S.-C. Lai *et al.*, "Development of Novel Dengue NS1 Multiplex Lateral Flow Immunoassay to Differentiate Serotypes in Serum of Acute Phase Patients and Infected Mosquitoes," (in English), *Frontiers in Immunology,* Original Research vol. 13, 2022–March–04 2022, doi: 10.3389/fimmu.2022.852452.

[5] B. Zhang, Z. Zhu, F. Li, X. Xie, and A. Ding, "Rapid and sensitive detection of hepatitis B virus by lateral flow recombinase polymerase amplification assay," *Journal of Virological Methods,* vol. 291, p. 114094, 2021/05/01/ 2021, doi: https://doi.org/10.1016/j.jviromet.2021.114094.

Design and Optimization of CRISPR/LAMP-Based Microfluidic Chip at the Point of Care (PoC) Level for Human Mpox Diagnosis

Hazal Çelik[1,*], Nazente Atceken[1,2,3], Ahmed Choukri Abdullah[4], Savas Tasoglu[1,2,3,4,5,6,7]

[1]School of Biomedical Sciences and Engineering, Koç University, Istanbul, Turkey, 34450
[2]Koç University Translational Medicine Research Center (KUTTAM), Koç University, Istanbul, Turkey, 34450
[3]School of Medicine, Koç University, Istanbul, Turkey, 34450
[4]Department of Mechanical Engineering, Koç University, Istanbul 34450, Turkey
[5]Koç University Is Bank Artificial Intelligence Lab (KUIS AI Lab), Koç University, Istanbul, Turkey, 34450
[6]Koç University Arçelik Research Center for Creative Industries (KUAR), Koç University, Istanbul, Turkey, 34450
[7]Boğaziçi Institute of Biomedical Engineering, Boğaziçi University, Istanbul, Turkey, 34684
[*]*Presenter*

1. Introduction

Mpox is a serious infectious disease which is classified as a global public health issue by World Health Organization (WHO) [1]. Due to the fact that there is a need for rapid, accurate, and accessible point-of-care molecular diagnostics. The combination of CRISPR and LAMP technologies allows enhanced viral detection through amplifying the fluorescent signal while ensuring sequence-specific confirmation [2]. In this study, a CRISPR/LAMP-based microfluidic chip for rapid Mpox diagnosis was designed, fabricated and characterized.

2. Materials and Methods

The microfluidic chip has LAMP, CRISPR, and fluorescence readout reservoirs. Sinusoidal channels were designed to interconnect reservoirs for micro-mixing and reducing pressure-burst effects by limiting direct flow into subsequent reservoirs [3]. Capillary stop valves were positioned at the outlet of each reservoir to ensure precise control over the staged flow. These localized constrictions act as passive pressure barriers that hold liquid during incubation until applied pressure surpasses the valve's burst threshold [4]. The geometries of the stop valves and their upstream reservoirs were designed to maintain a minimum pressure margin of 5 mbar to eliminate the risk of premature flow between stages. The Young–Laplace equation was used for preliminary design optimization, followed by experimental characterization to validate the performance of the chip. Contact angle measurements were also conducted to evaluate PDMS wettability and its effect on burst pressures. Molds were designed in SolidWorks (France) and fabricated using a Creative CADWorks (Canada) Profluidics 110 3D printer with Master mold Resin. PDMS chips were prepared using Sylgard 184 at a 10:1 ratio, cured, oxygen-plasma bonded, and annealed to restore hydrophobicity. Flow tests were conducted with DI water using an Elveflow OB1 pressure controller to measure the burst pressures. For on-chip assays, LAMP and CRISPR reagents targeting Mpox Plasmid DNA were pipetted into their corresponding reservoirs via punch reservoir access ports, frozen using liquid nitrogen and lyophilized. After lyophilization, the punched access ports were sealed with uncured PDMS and covered with a transparent film. Diluted Mpox DNA was then introduced into the chip via the pressure controller, transported the LAMP reservoir, incubated at 72 °C for 30 minutes using a portable

heater. The mixture is then moved to the CRISPR reservoir for incubation at 37 °C for 10 minutes, and fluorescent signals were imaged from the readout reservoir.

3. Results and Discussion

Flow tests conducted with DI water demonstrated reliable pressure-gated fluid control across the three capillary valve stages. The measured pressure margins between each capillary valve and reservoirs were $\Delta P_1 = 6.7 \pm 0.9$ mbar, $\Delta P_2 = 7.9 \pm 1.6$ mbar, and $\Delta P_3 = 14.2 \pm 1.8$ mbar, all exceeding the 5 mbar design threshold. Theoretical burst pressures were strongly correlated with experimental burst pressures (slope = 1.15, $R^2 = 0.837$). Measured burst pressures were generally higher, likely due to contact-line pinning, contact angle hysteresis, or mold-induced surface roughness [5, 6]. For on-chip assays, LAMP and CRISPR reagents were loaded via access ports and then lyophilized directly inside the chip with no observable structural damage or reagent loss. Flow tests with diluted Mpox DNA confirmed a sealed, and leak-free system while the chip maintained different isothermal regions (72 °C and 37°C) without thermal crosstalk. A clear fluorescence signal was detected when Mpox DNA was introduced to the system, whereas the negative control showed no signal.

Conclusion

The microfluidic chip demonstrated reliable fluid control, safe operating pressure margins, and successful on chip Mpox detection. Therefore, the platform holds a great potential as a portable, fluorescence-based tool for PoC testing while offering a baseline for future sensitivity and limit of detection (LoD) analyses.

Acknowledgement: The authors thank Koç University TUPRAŞ Energy Center (KUTEM) for oxygen plasma bonding.

References:

[1]World Health Organization. (n.d.). Mpox. World Health Organization. https://www.who.int/news-room/fact-sheets/detail/mpox

[2] Atceken N, Bayaki I, Can B, Yigci D, Tasoglu S. Mpox disease, diagnosis, and point of care platforms. Bioeng Transl Med. 2025;10(3):e10733. doi:10.1002/btm2.10733

[3] Birtek, M. T., Atçeken, N., & Tasoglu, S. (2025). Programmable 3DP microfluidic bio-reaction system: automated LAMP-on-a-chip. Lab on a Chip, 25(21), 5506–5523. https://doi.org/10.1039/d5lc00003c

[4] Wang, S., Zhang, X., Ma, C., Yan, S., Inglis, D., & Feng, S. (2021). A Review of Capillary Pressure Control Valves in Microfluidics. Biosensors, 11(10), 405. https://doi.org/10.3390/bios11100405

[5] Han, D. H., Oh, U., & Park, J.-K. (2023). Characterization of PDMS microchannels using horizontally or vertically formed 3D-printed molds by digital light projection. ACS Omega, 8(21), 19128–19136. https://doi.org/10.1021/acsomega.3c02933

[6] Cho, H., Kim, H.-Y., Kang, J. Y., & Kim, T. S. (2007). How the capillary burst microvalve works. Journal of Colloid and Interface Science, 306(2), 379–385. https://doi.org/10.1016/j.jcis.2006.10.077

Ultrasensitive and Rapid Detection of the Mpox Virus by Integrating CRISPR/Cas12a Enzyme Technology with an Electrochemical Sensor

Isil Cakiroglu[1,2*], Nazente Atceken[1,2,3], Begum Kubra Tokyay[1,2], and Savas Tasoglu[1,2,3,4,5,6,7]

[1]School of Biomedical Sciences and Engineering, Koç University, Istanbul, Turkey, 34450
[2]Koç University Translational Medicine Research Center (KUTTAM), Koç University, Istanbul, Turkey, 34450
[3]School of Medicine, Koç University, Istanbul, Turkey, 34450
[4]Department of Mechanical Engineering, Koç University, Istanbul 34450, Turkey
[5]Koç University Is Bank Artificial Intelligence Lab (KUIS AI Lab), Koç University, Istanbul, Turkey, 34450
[6]Koç University Arçelik Research Center for Creative Industries (KUAR), Koç University, Istanbul, Turkey, 34450
[7]Boğaziçi Institute of Biomedical Engineering, Boğaziçi University, Istanbul, Turkey, 34684
[*]*Presenter*

1. Introduction

The rapid and high-sensitivity identification of emergent viral diseases such as Mpox virus is important for localized diagnosis and effective outbreak control. Traditional molecular identification tools are very sensitive, but they usually need sophisticated equipment and take several hours to process, limiting their use in decentralized settings. Here, we present a device that integrates the enzymatic activity of CRISPR/Cas12a with an electrochemical detection system using a potentiostat, enabling rapid and practical measurements for the fast and sensitive detection of Mpox virus DNA. In the proposed sensor, CRISPR/Cas12a has a sensitive recognition ability and is activated upon binding to the target Mpox DNA sequence [1,2].

2. Materials and Methods

Once active, Cas12a starts showing non-specific trans-cutting on single stranded DNA reporters. The thiolated ssDNA and gold self-assembled monolayer (SAM) were used to link methylene blue-labeled single-stranded DNA probe to the surface of the gold electrode. The enzymatic activity is converted into an electrochemical signal by anchoring methylene blue (MB) labeled single-stranded DNA probes on the surface of the gold electrode through thiol gold self-assembling monolayer (SAM) synthesis [1-4]. Then the electrode surface is passivated with 6-mercapto-1-hexanol (MCH) to reduce non-specific adsorption and enhance the probe alignment. When Cas12α is activated, it will degrade the MB-labeled probes, and the electrochemical signal will change considerably owing to the detachment or flexibility of the redox reporter [1,3].

3. Results and Discussion

When comparing the electrochemical behavior of the electrodes using cyclic voltammetry (CV), differential pulse voltammetry (DPV), square wave voltagram (SWV), and electrochemical impedance spectroscopy (EIS), significant signal changes dependent on surface modification were observed. Modification of single-stranded DNA probes attached to the gold surface was successfully performed depending on the parameters, and the methylene blue signal was successfully obtained by differential pulse voltammetry. Surface modification was confirmed by performing cyclic voltammetry for 4 cycles. Furthermore, DPV measurements are more sensitive and can better distinguish signals, making it possible to determine lower target levels more reliably than CV measurements. In summary, the system demonstrated the ability to perform very sensitive detection with high signal-to-noise ratios and fast response times. In CV, while a significant cathodic current reaching approximately −45 µA

at around −0.35 V and an anodic signal of ~14–15 µA at around −0.10 V were obtained with the electrode measured only with PBS, the current response was largely suppressed after immobilization of ssDNA on the surface, dropping to approximately ±3–5 µA. This demonstrates that the ssDNA layer forms a negatively charged barrier limiting electron transfer on the electrode surface. Additionally, after 6-MCH blocking, the CV current remained similarly low and exhibited a flatter profile. This supports the idea that a more compact SAM structure is formed by filling the surface voids with 6-MCH. In DPV, measurements taken with PBS also showed distinct peaks in the ~0.20–0.25 V range on the electrode and ssDNA modified surfaces, with peak currents of approximately 60–70 µA. This result, showing a more controlled and lower signal shift after ssDNA immobilization and 6-MCH blocking on the surface, indicates increased surface blockade. In SWV, a distinct peak of approximately 28–30 µA was observed around −0.20 V on the clean surface, while the peak current decreased to approximately 20 µA after ssDNA and to approximately 5–10 µA after ssDNA/6-MCH [4,5]. In EIS results, the capacitive semicircle diameter increased from the clean surface to the ssDNA and ssDNA/6-MCH surfaces; this confirms that the charge transfer resistance increased and the electrode/electrolyte interface became more insulating [6]. Overall, when CV, DPV, SWV, and EIS data are evaluated together, it is observed that ssDNA immobilization followed by surface treatment with 6-MCH results in a decrease in faradaic current, an increase in Rct, and the formation of a more regular, electron-transfer-limiting DNA/MCH-SAM layer on the electrode surface [4].

Electrochemical impedance spectroscopy characterization was in line with the cyclic voltammetry data. After optimization and characterization of the surface modification, the results predict a significant decrease in the MB redox signal upon Cas12a activation in the presence of target DNA. So that means that the target recognition and signal transmission will be successful [7].

Conclusion

When everything is taken into account, this work presents a novel strategy for Mpox virus detection by integrating CRISPR/Cas12a technology with an electrochemical sensing platform. The proposed method is a good alternative to the traditional diagnostic technologies as it combines high specificity, rapid response and compatibility with small, portable devices. This method has a lot of potential for point-of-care applications and can be modified to detect other viral diseases.

Acknowledgement:

This research was funded from European Molecular Biology Organisation (EMBO) Scientific Exchange Grant (11627) and TÜBİTAK.

References:

[1] Dai, Y., Somoza, R. A., Wang, L., Welter, J. F., Li, Y., Caplan, A. I., & Liu, C. C. (2019). Exploring the trans-cleavage activity of CRISPR-Cas12a (cpf1) for the development of a universal electrochemical biosensor. Angewandte Chemie, 131(48), 17560-17566.

[2] Suea-Ngam, A., Howes, P. D., & DeMello, A. J. (2021). An amplification-free ultra-sensitive electrochemical CRISPR/Cas biosensor for drug-resistant bacteria detection. Chemical science, 12(38), 12733-12743.

[3] Kerman, K., Ozkan, D., Kara, P., Meric, B., Gooding, J. J., & Ozsoz, M. (2002). Voltammetric determination of DNA hybridization using methylene blue and self-assembled alkanethiol monolayer on gold electrodes. Analytica Chimica Acta, 462(1), 39-47.

[4] Hayat, M., Shah, A., Nisar, J., Shah, I., Haleem, A., & Ashiq, M. N. (2022). A novel electrochemical sensing platform for the sensitive detection and degradation monitoring of methylene blue. Catalysts, 12(3), 306.

[5] Duan, H., Wang, Y., Tang, S. Y., Xiao, T. H., Goda, K., & Li, M. (2023). A CRISPR-Cas12a powered electrochemical sensor based on gold nanoparticles and MXene composite for enhanced nucleic acid detection. Sensors and Actuators B: Chemical, 380, 133342.

[6] Raju, V. M., Bhavana, V., Gayathri, G. K., Suryan, S., Reddy, R., Reddy, N., ... & Santosh, M. S. (2020). A novel disposable electrochemical DNA biosensor for the rapid detection of Bacillus thuringiensis. Microchemical Journal, 159, 105434.

[7] Taufiq, S., Nagata, M., Abbas, S. R., & Sode, K. (2024). An electrochemical biosensor for the detection of tuberculosis specific DNA with CRISPR-Cas12a and redox-probe modified oligonucleotide. Heliyon, 10(23).

Multimetric Assessment of KOH-Assisted Reconfigurable Acoustofluidic Chip Bonding

Nurseli Seda Genç[1], Ayşe Erol[1], Furkan Kuruoğlu[1]*

[1]Department of Physics, Faculty of Science, Istanbul University, Vezneciler, 34134, Istanbul, Turkey

*Corresponding author: furkan.kuruoglu@istanbul.edu.tr

[1] Introduction

Acoustofluidic devices permanently bonded between lithium niobate surface acoustic wave (SAW) substrates and polydimethylsiloxane (PDMS) microchannels often suffer from limited reconfigurability and poor reusability after clogging, design modification, or surface degradation.

[2] Materials and Methods

In this study, a potassium hydroxide (KOH)-assisted bond-detach/rebond strategy was systematically reassessed using a multimetric analysis framework designed to distinguish surface evolution from device-level bonding functionality [1]. Device stability was evaluated through radio frequency (RF) resonance behavior derived from scattering parameter (S_{11}) spectra together with Young–Dupré work of adhesion, atomic force microscopy (AFM)-based surface roughness, Fourier transform infrared spectroscopy (FTIR)-based surface chemistry analysis.

[3] Results and Discussion

RF measurements confirmed stable RF response of the acoustofluidic device after repeated KOH cycles. Although AFM and FTIR analyses revealed progressive surface morphological and chemical modifications, the device retained its bonding functionality throughout repeated reuse cycles.

Conclusion

Overall, the results demonstrate that KOH-assisted reconfiguration preserves a functional bonding window that enables reliable, repeatable, and cost-efficient reuse of acoustofluidic platforms without significant performance degradation. This approach provides a practical route toward more sustainable and reconfigurable lab-on-a-chip systems for future acoustofluidic and cell-manipulation applications.

Acknowledgement:

This work is funded by The Scientific and Technological Research Council of Turkey (Project Number: 120F337) and The Scientific Research Projects Coordination Unit of İstanbul University (Project Number: FYL-2024-41154).

References:

[1] Kuruoğlu, F. (2022). A practical and cost-effective method to make permanently bonded acoustofluidic chips reconfigurable. Microfluidics and Nanofluidics, 26, 72.

Geometry-Dependent Flow-Induced Deformation Analysis in Micropillar-Based Microfluidic Systems for Viscosity Measurement

Özlem Koçoğlu[12]*, Ali Haydar Yıldız[1], Rezzan Yardımcı[13], Ahmet Can Erten[1]*

[1] Istanbul Technical University, Department of Electronics and Communication Engineering, Istanbul, Türkiye; [2] Istanbul Beykent University, Istanbul, Türkiye; [3] Istanbul Yeni Yüzyıl University, Istanbul, Türkiye

*: Özlem Koçoğlu (kocoglu21@itu.edu.tr) , Ahmet Can Erten (aerten@itu.edu.tr)

Introduction: Viscosity is a fundamental rheological property that describes the internal resistance of fluids to flow and is widely used for characterizing fluid behavior in industrial and biological systems [1]. Conventional viscometers are typically bulky and require large sample volumes, whereas microfluidic viscometers enable precise flow control, rapid analysis, small sample consumption, and easy integration with imaging systems [2]. In particular, micropillar-based microfluidic systems stand out as a method capable of converting fluid-structure interactions into measurable mechanical outcomes. In this study, the deformation behavior of micropillars with different geometries under various flow rates and viscosities was experimentally investigated using optical imaging and analyzed through ANSYS Fluent simulations. Although previous studies generally focused on viscosity and flow velocity for a specific micropillar geometry, the flow-induced response of different geometries has not been comparatively addressed through experimental and simulation-based approaches [3],[4]. Therefore, this study aims to evaluate the deformation responses of different micropillar geometries under varying flow rates and fluid viscosity conditions.

Materials and Methods: An SLA-printed mold containing square and circular micropillars was prepared and used to fabricate a PDMS master mold. PDMS microfluidic chips were then produced, bonded to microscope slides via UV-ozone treatment, and tested under various flow rate and viscosity conditions.

Results and Discussion: The experimental and simulation results confirm that increasing flow velocity and fluid viscosity increased micropillar deformation of the micropillar structures. Geometry-dependent structural analysis demonstrated that micropillar geometry plays a critical role in fluid-structure interaction and directly influences deformation behavior.

Conclusion: The results highlight the importance of micropillar geometry on flow-induced structural deformation and displacement sensitivity in microfluidic platforms.

References:

[1] Leblanc, G. E., Secco, R. A., & Kostic, M. (2023). Viscosity measurement. In *Mechanical Variables Measurement-Solid, Fluid, and Thermal* (pp. 11-1). CRC Press.

[2]Del Giudice, F. (2022). A review of microfluidic devices for rheological characterisation. *Micromachines*, *13*(2), 167.

[3] Mustafa, A., Eser, A., Aksu, A. C., Kiraz, A., Tanyeri, M., Erten, A., & Yalcin, O. (2020). A micropillar-based microfluidic viscometer for Newtonian and non-Newtonian fluids. *Analytica chimica acta*, *1135*, 107-115.

[4] Chang, Y. N., & Yao, D. J. (2026). A Microfluidic Platform for Viscosity Testing of Non-Newtonian Fluids in Engineering and Biomedical Applications. *Micromachines*, *17*(2), 201.

Best Poster Awards

This year, three outstanding poster presentations were recognized with the Best Poster Awards in acknowledgement of their scientific quality, originality, and presentation.

Sadık Koç from **the** Department of Bioengineering at Izmir Institute of Technology received the Best Poster Award for the poster titled **"Dynamic Tracking of Single Particles in a Pneumatic Valve-Integrated Microfluidic Magnetic Levitation System."**

Seymen İlke Kaykanat from the Department of Chemical Engineering at Boğaziçi University received the Second Place Poster Award for the poster titled **"Fiber-Based Microfluidic Model for Pressure-Driven Wall Transport Studies."**

Mehmet Oğulcan Güngör from Micro and Nanotechnology at METU received the Third Place Poster Award for the poster entitled **"Reversible Thermoplastic Integration Workflow for Packaging MEMS Devices and Commercial Electrodes into Microfluidic Cartridges."**